Granular Media

Flow & Agitations

PROEFSCHRIFT

Ter verkrijging van
de graad van Doctor aan de Universiteit Leiden,
op gezag van de Rector Magnificus
Prof. mr. P.F. van der Heijden,
volgens besluit van het College voor Promoties
te verdedigen op 1 december 2009
klokke 10.00 uur
door

Joshua Albert Dijksman
geboren te Den Haag
in 1981

Promotiecommissie:

Promotor: Prof. dr. M.L. van Hecke
Overige leden: Prof. dr. R.P. Behringer (*Duke University*)
                 dr. W. Losert (*University of Maryland*)
                 Prof. dr. J.W.M. Frenken
                 Prof. dr. J.M. van Ruitenbeek

*"And see how, just as drifting sands constantly overlay
the previous sand, so in our lives what we once did
is very quickly covered over by subsequent layers."*

Marcus Aurelius, *Meditations*.

Contents

CONTENTS

CONTENTS

Chapter 1

Introduction

1.1 Entree

What do sand, rice, coffee powder and Lego® bricks have in common? They are all *granular materials*: collections of non-Brownian, macroscopic particles with dissipative interactions. Despite their obvious relevance and their overabundance in nature, industry and households, the macroscopic mechanical properties of these materials are not well understood. The main theme of this thesis will be an experimental study of the properties of precisely these granular materials under weak driving. Due to their dissipative nature, energy has to be supplied, for example by shaking or shearing, in order to observe dynamics.

Chapters 2-5 deal with the flow of granular media in so-called *split-bottom* geometries, which in essence consist of a disk rotating at the bottom of a container. We study dry granular flows, both in the frictional, slow, rate-independent regime, and the liquid-like, rate dependent regime which is reached for faster flows. We shall also study suspension flows. We develop the so-called index matched scanning technique, that allows 3D imaging of the suspensions. Also for the suspension we study both the slow, rate independent and the faster, rate dependent regime. In all cases we combine 2D and 3D imaging of the flow with rheological measurements. Previously, the rheology of the split-bottom experiments had not been studied experimentally. We discuss here how to deal with the steep gradients arising near the split, and focus on the functional dependence of the driving torque as a function of flow rate and filling height. Both for the filling height and for the flow rate dependence, we

discuss and test recent theoretical predictions.

In chapter 6 and 7, the granular medium is also agitated by vibrations. Chapter 6 deals with slow granular flows in the split-bottom geometry, when this system is subjected to weak vibrations. Fluctuations play a crucial role for granular flows, and the additional vibrations allow us to tune the amount of fluctuations independently from the flow rate. These strongly affect the phenomenology -- even very weak vibrations completely destroy the rate-independent nature of slow granular flows, which are a hallmark of non-vibrated grain flows. In chapter 7 we revisit the classical tapping induced compaction experiments. By carefully controlling both the strength and duration of the taps, we find that not the peak acceleration, but rather the time of flight of the grains controls their behavior.

This chapter -- In section 1.2 we will consider what makes granular media interesting and sets them apart from other many-body systems in Nature. In section 1.3, we will give an overview of what is known of the basic phenomenology of slow granular flows. In this thesis we will study slow granular flows in a particular flow geometry called the *split-bottom* geometry; in section 1.4 we will therefore give a detailed overview of the current knowledge of granular flows in these systems. In section 1.5 we briefly review various theoretical approaches to granular flows, in particular the so-called *inertial number* theory. Although mostly applied to fast granular flows, it has also yielded insight in the nature of slow flows.

1.2   Granular Media

Macroscopically, granular media exhibit a complex mixture of solid and fluid-like behavior. This is commonly illustrated by the fact that it is possible to walk on completely dry beach sand, which supports one's weight as if it were a solid. By scooping up a handful of this sand, and letting it run through one's fingers, the fluid-like nature of the material is also immediately obvious.

Microscopically, this complex behavior has various sources. First of all, the mere size of the granular constituents makes them insensitive to thermodynamic temperature: the gravitational energy mgd of a 1 mm sand grain exceeds k_BT by 14 orders of magnitude. This implies that a thermal equilibrium as understood in the statistical mechanics framework is never reached. Interactions between the grains are dissipative -- kinetic energy of a macroscopic particle can always be transformed into thermal energy of the atoms and molecules that make up the particle. For example: a glass marble dropped on a glass plate rebounces to ever

smaller heights. The athermal and dissipative nature of the microscopics leads to systems very far from equilibrium. In particular, when not externally driven, granulates condense into a (meta)stable, quiescent state: a bag of glass particles dropped on a glass plate comes to rest virtually instantaneously. Interactions between particles are usually only weakly attractive, if at all. This makes granular materials easily deformable on macroscopic length scales, if no external pressure is applied. The interaction potentials between individual particles are at the same time also highly nonlinear, and involve many length and timescales [1].
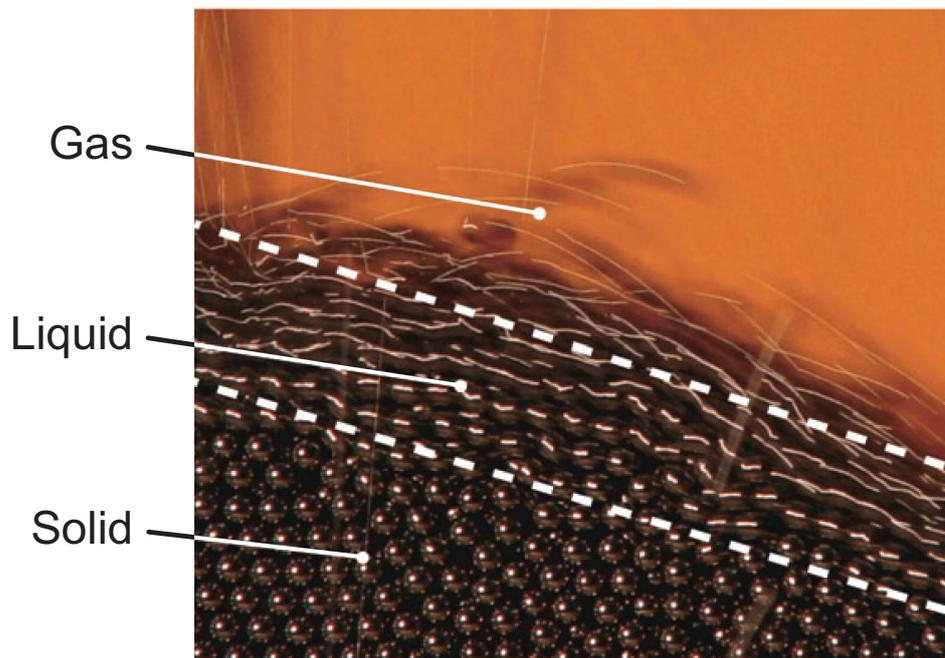
Figure 1.1: A motion-blurred image of steel beads poured on a pile illustrates the three distinct phases of granular material. Figure adapted from Ref. [2]. Reproduced with permission. Copyright (2008) Annual Review Inc.

Granular solids, liquids and gases -- A common trisection of granular materials is to view them as being either solid, liquid or gas-like, depending on the way the material is driven [2, 3]. An illustration of this viewpoint is shown in Fig. 1.1. Steel beads are poured on a heap from which they flow down, and exhibit the three phases: on top of the flow down the heap, there is a dilute phase where collisions are the dominant interaction between the beads. This

thesis will not touch upon this regime; we refer the reader interested in this *gaseous* regime to review articles like Ref. [4]. In the semi-dilute phase just below this granular gas regime, beads also have enduring frictional contacts, but still flow easily past each other. With increasing distance to the surface of the heap, this *liquid* phase then crosses over into a phase in which the particles do not have much free volume anymore to move past each other, and do not experience collisions anymore, but only have enduring contacts. This phase is referred to as the *solid* phase; in this phase the particles are essentially static.

This complex behavior of granular materials is often hard to predict or capture in models. At present, there is for example no *general* approach which, for given flow geometry, driving strength and grain properties, predicts the ensuing granular flow fields. Given the ubiquity of granular materials, it is evident that such modeling is highly desirable. Apart from being studied for the utilitarian value of a better understanding of them, granular materials also serve as a model system to study the *jamming* transition. This phase transition, separating a disordered solid- and liquid-like phase is speculated to be exhibited not just by granular materials, but by many different kinds of disordered systems, such as colloidal suspensions, emulsions and foams. The jamming concept therefore has the potential of underpinning a universal framework for the description of such disordered systems. The study of granular materials has contributed greatly to the development of this theory, although many questions remain unanswered.

In this thesis we will focus on the boundary between the liquid and solid phase by studying slow granular flows. What do we mean by slow? As will be detailed in Section 1.5.1, we can compare the shear rate $\dot{\gamma}$ in the granular flow to the rearrangement timescale of a particle inside this flow. The simplest timescale one can construct with the relevant variables ρ (the density of the grains), P (the local pressure acting on the particle), and d (its diameter) is the time it takes for a particle to move over a distance d given that it is exposed to a pressure difference P: $d/\sqrt{P/\rho}$. For $\dot{\gamma}$ small compared to $d/\sqrt{P/\rho}$, so for $\dot{\gamma}d/\sqrt{P/\rho}$, we call the flow *slow*. In this regime, particles interact via enduring contacts, and inertial effects are negligible.

Two features of slow flows are very robust. Whatever the driving geometry, the average forcing required to sustain a certain flow rate becomes independent of the driving rate. Likewise, the obtained flow profiles become independent of the driving rate. Therefore, we refer to the regime of slow flows as the *rate-independent* regime. In the literature the term *quasi-static* is also very often used to refer to this regime. This rate independence is due to the fact that

the dominant type of interaction between the particles is frictional, and sliding friction is at most only weakly dependent on the sliding velocity [5].

1.3   Slow Flow Geometries: Planar, Couette and Chute

To study granular flows, one has to induce motion in the grains. This can be done by imposing a force or, equivalently, a *stress* -- a force per unit area -- on the material, or a deformation or *strain* -- a deformation per unit length.
In a typical flow geometry called the *inclined plane*, a constant stress is applied. A table is placed at some angle with respect to gravity, and grains are poured onto this table from a large reservoir -- see Fig. 1.2a. The constant stress, acting on the grains, depends on the tilt angle of the table. The special character of the behavior of granular material is however such that in decreasing this stress smoothly to zero, by reducing the tilt angle of the inclined plane, its resulting flow speed will not go smoothly to zero -- below a certain threshold inclination, the flow will come to a halt; the packing *jams*.
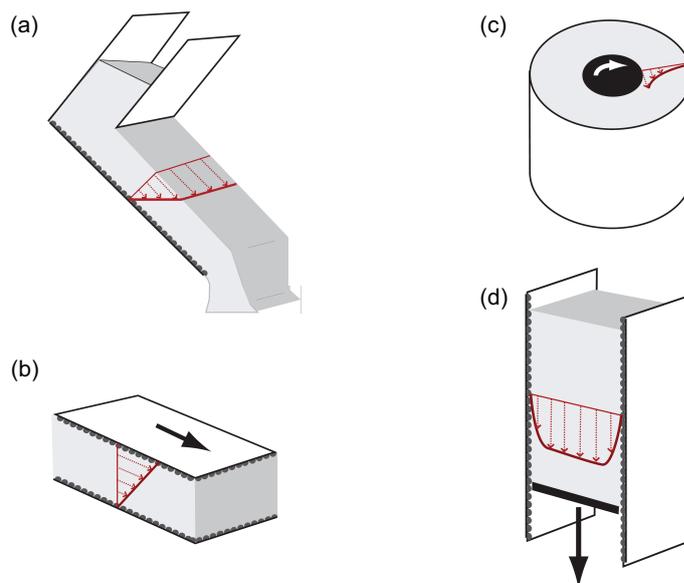
Figure 1.2: Four different flow geometries. (a) inclined plane; (b) plane shear; (c) Couette ; (d) chute. Figure adapted from Ref. [2]. Reproduced with permission. Copyright (2008) Annual Review Inc.

To study arbitrarily slow flows, one therefore has to *impose* deformation,

since this can then be done at arbitrary rate. The canonical way to do this is to use some container with a constantly moving, rough boundary. This is usually accomplished in one of the three following different geometries: planar, in which granular material is sheared between two parallel plates (Fig. 1.2b); Couette, where shear takes place between an inner and an outer cylinder (Fig. 1.2c), and the chute flow geometry (Fig. 1.2d), which is essentially a rectangular, vertical pipe. Chute flow does not involve a physically moving boundary; shear is driven by gravity as in the inclined plane geometry. In contrast to the inclined plane flow, the flow rate in the silo, and with that the shear rate, can be made extremely small by adjusting the flux of particles at the bottom.

Note that if one drives the system externally, for example by means of vibrations, a constant force is usually also sufficient to set up an arbitrarily small but constant flow speed [6, 7], irrespective of the geometry. We will also apply this principle in the split-bottom geometry to induce constant flow under constant applied stress -- see chapter 6.

Another common rheometric geometry is notably absent in the literature on the flow properties of granular materials: the cone-plate geometry [8]. In this geometry, material is sheared between a rotating cone and a static plate. The advantage of cone-plate geometries is the fact that the shear stress in the gap is constant [8]. The only setup that setup that comes close to the cone-plate geometry is the wide plate-plate setup used by Lu [9, 10]. The reason why cone-plate geometries are not used is simple: confining material in the cone-plate gap is normally achieved by the surface tension of the fluid. Granular materials do not have surface tension, since they do not have attractive interaction potentials. Therefore, one would have to confine the granular materials inside the gap with side walls positioned very close to the edge of the disk (as in the plate-plate geometry from Refs. [9, 10]), which creates nonuniform shear conditions at the outer edge of the cone.

In this section, we shall describe the basic phenomenology of slow granular flows observed in the plane shear, Couette and chute geometries. For all geometries, we will describe the main experimental parameters and discuss experimental and numerical observations of the velocity profiles, stresses and dilatancy effects, if available.

Apart from the setups described above, there is another geometry that allows one to impose deformations at a constant rate: the split-bottom geometry. In the split-bottom geometry, the source of the driving is a buried, rotating disk. Since the split-bottom geometry is the geometry we shall use in almost all experiments covered by this thesis, the flow behavior observed in this flow cell warrants a more detailed description, which will be given in section 1.4.

1.3.1   Plane Shear Flow

The simplest way to impose shear deformation is in a plane shear geometry, depicted in Fig. 1.2b. In this geometry, there are two control parameters: the shear velocity V and the gap size W. Numerical work has shown that for slowly driven systems, these velocity profiles at short times are highly intermittent [11], and that, averaged over enough strain, a linear profile is always recovered, also in the rate independent limit [12]. Note that in experiments linear profiles are seldom observed [13].

   Dilatancy has been observed already very early in plane shear experiments [14]. Kabla [15] confirmed quantitatively that dilatancy in slow granular flows is a function of the total strain in the sample. These X-ray experiments revealed the following relationship between the strain s and volume fraction Φ:

$$\Phi(s) = \Phi_{min} + (\Phi_{max} - \Phi_{min}) \exp(-s/s_c), \tag{1.1}$$

where s_c is a characteristic amount of strain after which equilibrium is reached.

   Of all the geometries mentioned, plane shear is easiest to realize in numerics, but very hard to study experimentally. To obtain a constant stress, gravity has to be eliminated, and for steady state flow analysis, large strains are necessary, which are difficult to obtain in experiments. To circumvent these problems, Couette and chute experiments are usually carried out.

1.3.2   Couette Flow

Apart from grain properties, the system parameters for the Couette geometry are the radius of the inner wheel R_i and the outer wheel R_o, the dimensionality (two or three), and driving rate Ω. The flow localizes near the moving boundary in a *shear band*. This shear banding is generally very strong, with bands having a typical thickness of five to ten grain diameters. Shear banding appears to be robust: studies in Couette cells always show the formation of a narrow shear band near the inner cylinder, irrespective of dimensionality and driving rate [16]. Close to the driving wall, the velocity profile in Couette flows can be expressed as the product of an exponential and a Gaussian [16, 17]:

$$v_\theta(r) = v_o \exp[-b(r/d)] \exp\{-[c(r - r_o)/d]\}^2, \tag{1.2}$$

Here $v_\theta(r)$ is the velocity profile, v_o, b and c and r_o are fitting constants that depend on the particle shape and roughness. d is the particle diameter. This velocity profile was also found in rate independent flows in an annular shear cell [18]. Further away from the wall, purely exponential tails were observed [19].

Note that for small gaps, where $R_i - R_o$ is of the order of a few particle diameters, a linear profile is observed [20].

The average driving stresses necessary to sustain a constant rotation rate in these Couette flows are generally independent of Ω. Hartley [5] found a weak logarithmic dependence on Ω for slightly compressed systems. The stresses can show large fluctuations though, since the flow can be intermittent [5]. In the intermittent flows, Eq. 1.2 is only obtained after time averaging. In two dimensions, below a certain critical volume fraction of about 0.78, the stress necessary to drive the flow disappears completely; above this volume fraction, the logarithmic rate dependence increases with the distance to this critical filling fraction [5]. These large filling fractions were obtained with relatively soft particles, with a Young's modulus of 4.8 MPa [17]. Rigid grains like glass beads, which have a Young's modulus of the order of GPa, are only slightly deformed in a typical experiment, so they are typically close to this critical fraction [21], which means that their logarithmic dependence is probably weak.

Shearing frictional granular materials induces *dilatancy*, an increase in volume of a fixed amount of grains. This was already observed by Reynolds [22]. He filled a bag with shot and water to its maximum capacity, and noticed he could add extra water after deforming the bag, showing an increase in the interstitial volume due to the deformation. Dilatancy is also observed in Couette geometries. Closer to the driving wall, the dilatancy is more pronounced [16, 23, 24].

1.3.3 Chute Flow

In chute flow, also sometimes called *silo* flow, the main control parameters are the width of the channel W and the flow rate imposed at the outlet Q [25]. The flow profile is that of plug flow, with narrow shearbands at the edges [26]. A typical plug flow profile is indicated in Fig. 1.2b. This flow profile is found for essentially all flow rates [27], including the rate independent regime. Dimensionality and W do not affect the width of the shearband. Most notably at small Q, the flow can become very intermittent. This is due to the sudden appearance of load bearing force network configurations [28]. Averaging of the flow field is therefore necessary to obtain the plug flow profile shown in Fig. 1.2b. The flow can also experience complete arrest, due to jamming of the orifice where the particles exit the pipe [29], although this orifice jamming disappears for large enough orifice sizes. Strong dependence of the flow kinematics on particle material stiffness and interparticle friction coefficient was also found [30], although the

average flow profiles obtained in that numerical work are also that of the type indicated in Fig. 1.2b. As for Couette flow, for chute flow, phenomenological equations for the shape of the shearband have been put forward ([25, 28]). The models however all involve exponential shear localization at the edges; usage of such models is based on the assumption that transition state theory ideas can be applied to these flows -- see section 1.5.2.

1.4 Slow Flows in the Split-Bottom Geometry

This thesis will concern itself mostly with granular flows in so-called split-bottom geometries. In this section we will review the results of recent experiments and numerical work on the flows which have been generated in these special flow geometries.
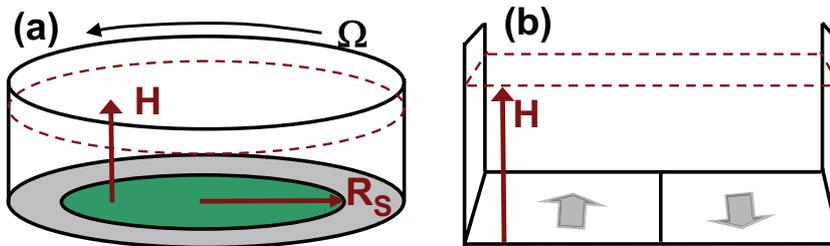
Figure 1.3: (a) Cylindrical split-bottom geometry, showing a disc of radius R_s at the bottom of a granular layer of depth H. Here, the outer cylinder rotates with rate Ω and the bottom disc is kept fixed -- the alternative geometry, with fixed outer cylinder and rotating disc is also frequently encountered. (b) Linear split-bottom geometry, where a container is split along a straight line in its bottom. This geometry can be seen as the $R_s \rightarrow \infty$ limit of the cylindrical cell.

1.4.1 General Description

The essential feature of the split-bottom is that it drives the granular medium not directly from the sidewalls, but only from the bottom. The bottom of the container that supports the grains is split in two parts that slide past each other. This way, one takes advantage of gravity to drive the granulate from the sliding discontinuity in the bottom support of the grain layer. This effectively creates and pins a wide shear zone away from the sidewalls. The resulting grain flows

are smooth and robust, with both velocity profiles and the location of the shear zones exhibiting simple, grain independent properties.

In this section, we focus on the rate independent regime. Two variants of the split-bottom geometry will be encountered: in experiments one typically employs a cylindrical split-bottom shear cell, consisting of a bucket, at the bottom of which a disc rotates with respect to the bucket (Fig. 1.3a) [31--34], while for theoretical studies the linear split-bottom cell with periodic boundary conditions is more convenient (Fig. 1.3b) [35--38].

1.4.2 Parameters and Regimes

The cylindrical split-bottom geometry is characterized by three parameters. The radius of the bottom disc R_s and its rotation rate Ω are generally fixed in a set of experiments, and the relative motion of disc with respect to the cylindrical container drives the flow. The thickness of the granular layer, H, is the control parameter that typically is scanned in a series of experiments. Note that the radius of the container appears immaterial, as long as it is sufficiently large (25% larger than R_s appears to be sufficient [32]).

We denote the ratio of the averaged azimuthal velocity of the grains $v_\theta(r)/r$ and the disk rotation speed Ω by ω; $\omega = 0$ thus corresponding to stationary grains, while $\omega = 1$ corresponds to grains comoving with the driving. For the small Ω of interest here (typically less than $0.1\,\mathrm{s}^{-1}$), the flow profiles $\omega(r, z)$ appear independent of Ω -- the flow is rate independent, and transients are short lived. Since centrifugal forces are negligible for typical sizes of R_s (typically a few cm), one may also fix the disc and rotate the bucket, and essentially obtain the same sort of flows with $\tilde{\omega}(r, z) = 1 - \omega(r, z)$ -- see [31--33]. The two remaining parameters, H and R_s, set the large scale structure of the flow.

When the disk rotates, a shear zone propagates from the slip position R_s upwards and inwards. The qualitative flow behavior is governed by the ratio H/R_s, and three regimes can be distinguished. A regime of shallow layers is found for $H/R_s < 0.45$, and here the shear zone reaches the free surface. The three-dimensional shape of the shear zones is roughly that of the cone of a trumpet, with the front of the trumpet buried upside down in the sand. Another regime of deep layers plays a role for $H/R_s > 0.65$, and here the shear zone essentially forms a dome-like structure in the bulk of the material; little or no shear is observed at the free surface. In between there is an intermediate regime, where the shear in the bulk of the material is a mix between the trumpet and dome-like shape.

1.4.3 Surface Flow

Shallow flows -- We first focus on the flow observed at the free surface. For shallow layers, a narrow shear zone develops above the split at R_s, and when H is increased, the shear zone observed at the surface broadens continuously and without any apparent bound. Additionally, with increasing H, the shear zone shifts away from R_s towards the center of the shear cell.
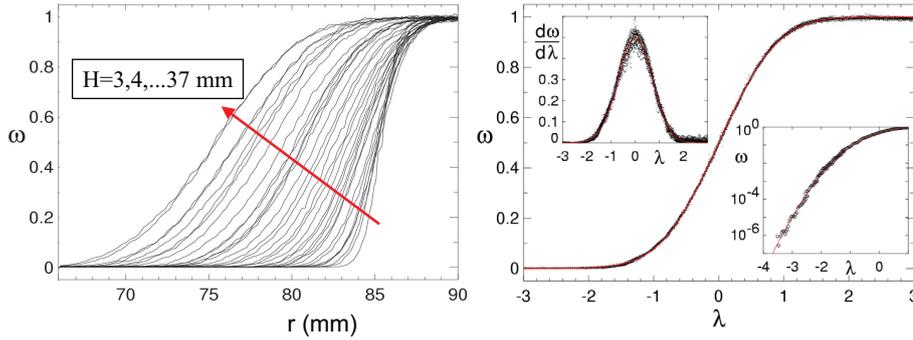
Figure 1.4: (a) Surface flows for glass beads of diameter 300 μm and a range of filling heights H as indicated are well described by an error function (fit not shown) - $R_s = 85$ mm here, and the outer cylinder is rotating. (b) Collapse of the surface flow profiles shown in (a) and comparison to error function. The rescaled radial coordinate λ is defined as $(r - R_c)/W$. Top inset: strain rates are Gaussian. Bottom inset: the tail of flow profile corresponds well to the Gaussian tail of the error function. Figure reprinted with permission from Ref. [31]. Copyright (2003) by Nature Publishing Group.

After proper rescaling, all bulk profiles collapse on a universal curve which is extremely well fitted by an error function:

$$\omega(r) = \frac{1}{2} + \frac{1}{2} erf\left\{\frac{r - R_c}{W}\right\}, \tag{1.3}$$

where *erf* denotes the error function, *r* is the radial coordinate, R_c the center of the shearband (where $\omega(r) = 0.5$) and W the width of the shearband (Fig. 1.4). Accurate measurement of the tail of the velocity profile further validate Eq. (1.3), and rule out an exponential tail of the velocity profile (Fig. 1.4b). The strain rate is therefore Gaussian, and the shear zones are completely determined by their centers R_c and widths W.

Particle shape does not influence the functional form of the velocity profiles, in contrast to the particle dependence found for wall-localized shear bands in a

Couette cell [16]. For these, the vicinity of the wall induces the formation of semi-crystalline particle layers, in particular for monodisperse mixtures. Apparently such layering effects play no role for these bulk shear zones.
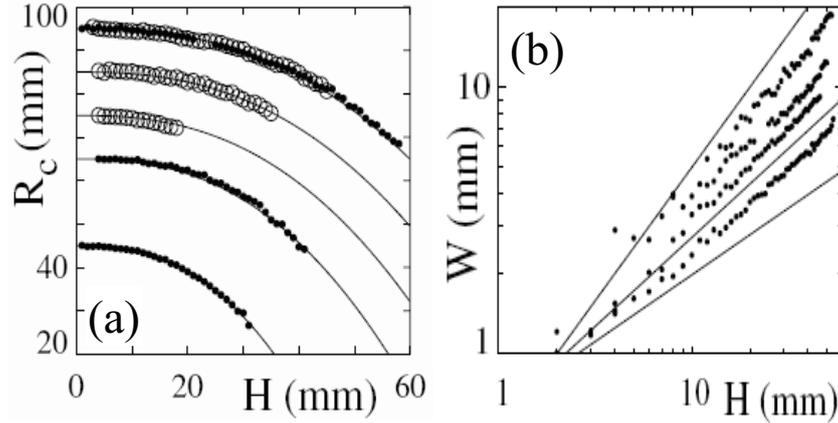
Figure 1.5: (a) Shear zone positions R_c versus H, where R_s = 95, 85, 75, 65, and 45 mm. Lines correspond to Eq. 1.4. (b) Log-log plots of W for spherical glass beads of increasing sizes (ranging from average diameter 300 μm to 2 mm) for R_s = 95 mm. The lines shown in (b) correspond to exponents of 1/2, 2/3, 1. Figure reprinted with permission from [32]. Copyright (2004) by the American Physical Society.

Remarkably, the shear zone center, R_c, turns out to be independent of the material used (Fig. 1.5a). Therefore, the only relevant length-scales for R_c appear to be H and R_s. We find that the dimensionless "displacement" of the shear zone, $(R_s - R_c)/R_s$, is a function of the dimensionless height (H/R_s) only. The simple relation

$$(R_s - R_c)/R_s = (H/R_s)^{5/2} \tag{1.4}$$

fits the data well (Fig. 1.5a).

The relevant length scale for the shear zone width W defined above is given by the grain properties, and is independent of R_s (Fig. 1.5b). Grains shape, size, and type also influence $W(H)$: irregular particles display smaller shear zones than spherical ones of similar diameter. The best available experimental data shows that

$$W/d \sim (H/d)^{2/3} , \tag{1.5}$$

where d denotes the particle diameter, although this scaling has not been checked over more than a decade.

The available numerical data coming from molecular dynamics simulations essentially confirm this picture [34, 36, 37, 39]: the surface flows in split-bottom geometries for $H/R_s < 0.45$ are given by Eqs. 1.3-1.5. Only the absolute width of the shear zone remains as a fit parameter, but once this width has been measured for a single value of H/R_s, Eq. 1.5 can be used to estimate the width for the whole range of $H/R_s < 0.45$.

Deep flows: symmetry breaking and precession -- When H/R_s is small, the core material rests on and co-moves with the center disc. With increasing H/R_s, the width of the shear zone grows continuously, and its location moves inward towards the central region (Eq. 1.4). This implies that for deep layers qualitatively different flow patterns can be expected to occur.
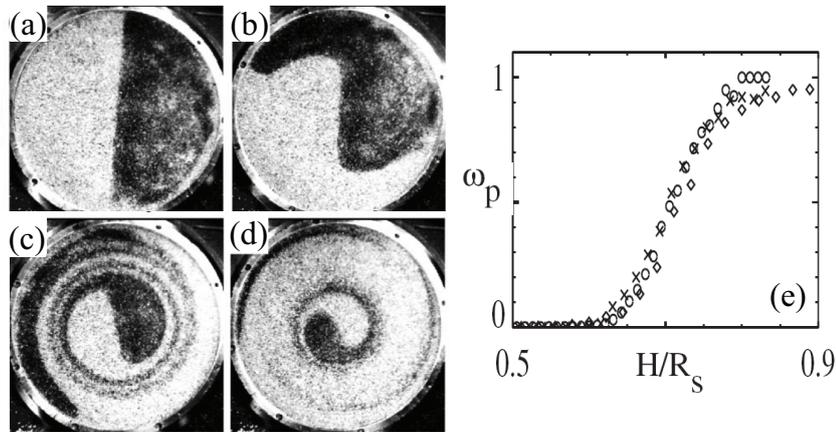
Figure 1.6: Core precession in a split-bottomed geometry. (a-d) Series of snapshots of top views of a setup with stationary disc and rotating outer cylinder (for $R_s = 95$ mm, $H = 60$ mm, and rotation rate $\Omega = 0.024$ rps), where colored particles sprinkled on the surface illustrate the core precession for t = 0 s (a), t = 10 s (b), t = 100 s (c) and t = 1000 s (d). (e) Data collapse of the precession rate ω_p for $R_s = 45$ mm (diamonds), $R_s = 65$ mm (x) and $R_s = 95$ mm (circles) when plotted as a function of H/R_s. Figure reprinted with permission from Ref. [33]. Copyright (2006) by the American Physical Society.

The most striking feature of these flows is that the core, as observed at the free surface, now precesses with respect to the bottom disc - hence material in the central part of the system no longer rests on the disc, and there is *torsional failure* of the core. Precession is not simply a consequence of the overlap of

two opposing shear zones, since before being eroded by shear, the inner core rotates as a solid blob for an appreciable time (Fig. 1.6a-d).

The precession rate ω_p is defined as the limit of $\omega(r)$ for r going to zero, where we assume, for simplicity, that the outer bucket rotates with rate Ω and the bottom disc is kept fixed, as in [33] -- consistent results are found in a setup where the disc was rotated and the outer cylinder kept fixed [34]. For various slip radii, the onset height for precession grows with R_s, and the data for ω_p collapses when plotted as a function of H/Rs (Fig. 1.6e). When H/R_s becomes of order one, the whole surface rotates rigidly with the rotating drum and all shear takes place in the bulk of the material. On the other hand, for $H/R_s < 0.65$, hardly any precession can be observed.
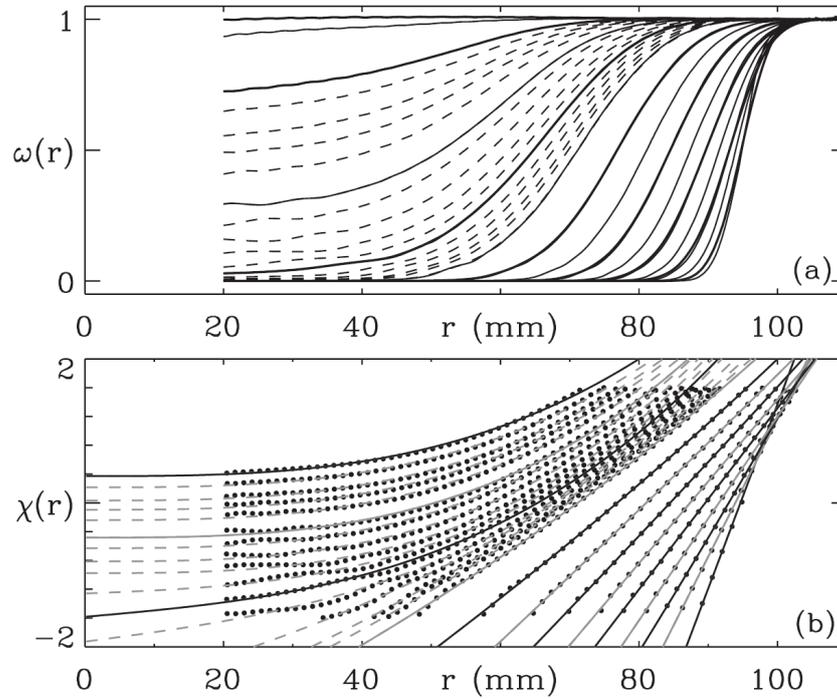
Figure 1.7: Surface velocity profiles $\omega(r)$ for $R_s = 95$ mm and increasing layer depth H. Thick curves: $H = 10, 20 \ldots 80$ mm; Thin curves $H = 15, 25, \ldots 75$ mm; Dashed curves $H = 56, 57, \ldots 69$ mm. (a) Precession gradually sets in for $H > 60$ mm. (b) Corresponding profiles of $\chi(r)$ (dots, see Eq. 1.6), compared to cubic fits given by Eq. 1.7 (curves). Figure adapted from [33].

Intermediate regime and symmetry breaking -- In the intermediate regime, $0.45 < H/R_s < 0.65$, a precursor to the transition to precession can be observed, since a careful analysis reveals that the surface velocity profiles $\omega(r)$ increasingly become asymmetric for $H/r_s > 0.45$. In fact, one can generalize Eq. 1.3 by writing

$$\omega(r) = \frac{1}{2} + \frac{1}{2}erf(\chi(r)),\tag{1.6}$$

and by fitting the data for $\omega(r)$ over the whole range of H/R_s to this equation (Fig. 5), one finds that $\chi(r)$ can be fitted well by a cubic polynomial of the form

$$\chi(r) = a_0 + a_1\,r + a_3\,r^3\,.\tag{1.7}$$

For shallow layers, $a_3 = 0$, and a_0 and a_1 follow from the scaling laws Eqs. 1.4 and 1.5. For $0.45 < H/R_s < 0.65$, a_3 starts to grow and governs the symmetry breaking of the flow profiles, while for deep layers ($H/R_s > 0.65$), a_1 tends to zero, and a two parameter fit describes the flow profiles well again.
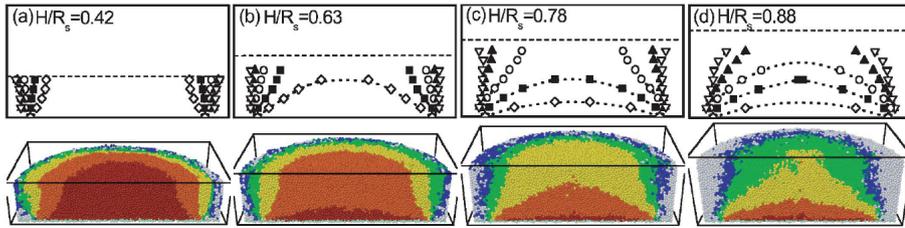
Figure 1.8: Contours of constant angular velocity ω, for different filling height H. Upper panels: MRI experiments: $\omega = 0.84$ (diamonds), 0.24 (squares), 2.4×10^{-2} (circles), 2.4×10^{-3} (triangles), and 2.4×10^{-4} (inversed triangles). Dashed lines indicate H and dotted lines are guides to the eye. Lower panels: simulations. Color is used to identify velocity ranges: dark red, $\omega \in [0.84, 1]$; orange, $\omega \in [0.24, 0.84]$; yellow, $\omega \in [2.4 \times 10^{-2}, 0.24]$; green, $\omega \in [2.4 \times 10^{-3}, 2.4 \times 10^{-2}]$; blue, $\omega \in [2.4 \times 10^{-4}, 2.4 \times 10^{-3}]$; grey, $\omega \in [0, 2.4 \times 10^{-4}]$. Figure reprinted with permission from [34]. Copyright (2006) by the American Physical Society.

1.4.4   Bulk Flow

Shallow flows -- The bulk structure of granular flows is harder to access, but by now, we have information on split-bottom flows from experiments that bury and excavate colored beads [32], MRI [34,40] and numerical simulations [34,36,37,39]. First, for shallow layers, the flow profiles at fixed depth z below the surface H still

takes an error function form, which allows us to characterize $\omega(r)$ at fixed z with the same two parameters R_c and W as before. The location of the shear zones in the bulk where found to be consistent with a scaling argument put forward by Unger *et al.*. The idea is follows: Eq. 1.4 gives the location R_c at the free surface. Then to obtain R_c at depth z, one imagines a systems with a depth of $H - z$, and by inverting Eq. 1.4, obtains where the split would have to be in a system of depth of $H - z$ for the surface location to be as given [41]. This yields:

$$z = H - R_c \left[1 - R_c/R_s(1 - H/R_s)^{2.5} \right]^{1/2.5} . \tag{1.8}$$

The width $W(z)$ of the shear zones is harder to obtain reliably, but the best available experimental data suggest a power law growth of the form $W \sim z^\alpha$, where α is less than 1/2 and more than 1/4 [32, 35]. More recent numerical studies [37] found that $W(z)$ can be well described by a "quarter circle" curve of the form

$$W(z) = W(z = H)\sqrt{1 - (1 - z/H)^2} . \tag{1.9}$$

Deep Flows -- The symmetry breaking and the eventual disappearance of grain motion at the surface indicates that qualitatively different bulk flow is developing: the trumpet shape of the shear zones present in shallow layers must have changed. When H/R_s is sufficiently large, the shear zone is entirely confined to the bulk of the material, and forms a dome-like structure above the rotating disk [33, 34, 40, 41] -- see Fig. 1.8. The torsional failure of the material is thus concentrated in the dome. Cheng *et. al.* measured the functional form of the axial velocity profile $\omega(z)|_{r=0}$, and found it to be described by a Gaussian:

$$\omega(z, r = 0) = \omega_p + (1 - \omega_p) \exp{-z^2/(2\sigma^2)} , \tag{1.10}$$

where ω_p is the rotation rate observed at the surface at $r = 0$, which decreases roughly exponentially with H, and σ, the width of the bulk Gaussian velocity profile, is approximately $R_s/5$ [34].

Couette versus split-bottom geometries -- The first studies [31] of split-bottom geometries where done in a modified Couette cell, as shown in Fig. 1.9. The resulting flows are similar to the disc geometry, as long as the shear flow is away from the side walls, but since for increasing filling heights the shear zones move inward, they will inevitably "collide" with the inner cylinder for sufficiently large filling height. The resulting flow profiles are shown in Fig. 1.9 [42].

First, one observes that for sufficiently large H, the flow profiles become independent of H. The main result is that the tail of these flow profiles becomes purely exponential for large H, while it is Gaussian for shallow H. We have found
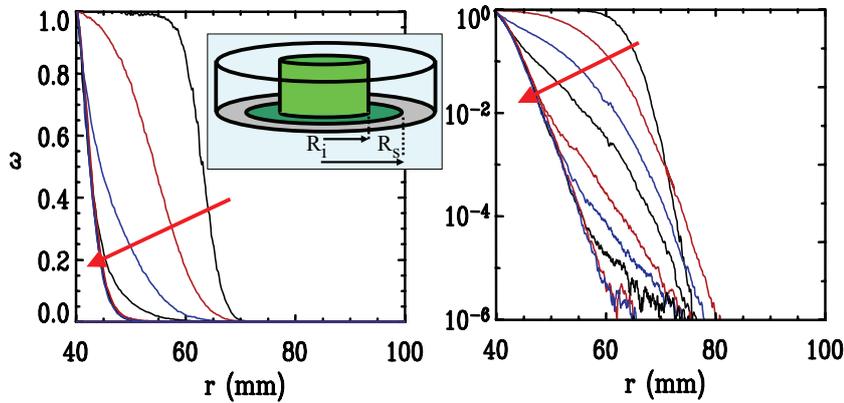
Figure 1.9: Surface flow profiles observed for 1 mm glass beads in a split-bottom Couette geometry, with inner cylinder radius $R_i = 40$ mm, a split at $R_s = 65$ mm, and $H = 10, 30, 40, 50, 60, 70, 80, 100, 110$ mm. The outer cylinder is 120 mm. Figure from Ref. [42].

this exponential talk to be robust, i.e., independent of grain shape. Note that this does not contradict the findings of Mueth *et al.* -- these concern the shape of the flow profile near the shearing wall, corresponding to the range $10^{-3} < \omega < 1$ -- flow profiles are indeed grain dependent here. But further out in the tail they become purely exponential. For other examples of exponential tails see [43].

1.4.5 Dilatancy

By means of Magnetic Resonance Imaging, direct measurements of the evolution of the local packing density of the shear flow generated in a cylindrical split-bottomed geometry were performed in [40]. To be able to image the particles by means of MRI, food grade poppy seeds were used; these contain MRI-detectable mineral oils.

It was observed that the relative change in density in the flowing zone is rather strong and saturates around 10-15 % -- likely the rough and peanut shape of the poppy seeds plays a role. After long times, a large zone with more or less constant, low packing fraction forms, encompassing most of the shearband. The fact that the density remains constant here, even though local strain rates vary over many decades, suggests that the density of the flowing material is a function of the *total strain*, and not of the strain rate, similarly to what was

17
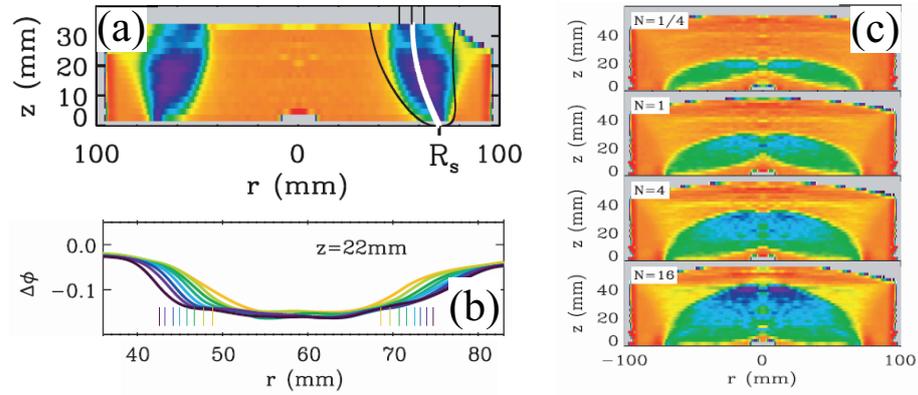
Figure 1.10: Evolution of dilatancy. (a) Color map of relative density change (light blue corresponds to -10%) for $H/R_s = 0.51$ after 4 rotations of the bottom disk (b) Spread of dilated zone for vertical shear observed in the bulk at $H/R_s = 0.51$ at $z = 22$ mm ($H = 36$ mm), for $N = 1/2, 1, 2, \ldots, 64$, compared to estimates where, after N turns, the local strain equals one. (c) Spread of dilatancy for dome-like flow observed at $H/R_s = 0.77$, for number of disc rotations N as indicated. Figure reprinted with permission from Ref. [40]. Copyright (2008) by EDP Sciences.

observed by Kabla [15].

Consistent with this, the dilated zone was found to slowly spread throughout the system as time progresses (Fig. 1.10). This spread is consistent with the idea that, after initial preparation, the accumulated local strain governs the amount of dilatancy -- to show this, the flow field in the bulk was reconstructed by combining the above mentioned scaling relations for the location and width of the shear zones in the bulk, and this reconstructed flow field can then be compared to the density field obtained by MRI. Such comparison shows that the locations of the dilated zone and the shear zone coincide, for small filling heights ($H/R_s < 0.6$). Finally, for deep filling heights where torsional failure and precession play a role, a relatively long-lived transient was found to cause the dilated zone to deviate substantially from the late-time shear zone.

1.5 Theory for Granular Flows

Our focus is on slow flows, for which over the years a variety of theories have been put forward. These theories have been successful by varying degree, but as yet, no theory can capture all the physics of slow granular flows. It

remains for example remarkable that no theoretical framework is available from which Eqs. 1.3-1.5 can be deduced. Creating such a theory would constitute an important milestone in the development of our understanding of slow granular flows.

Much progress has however been made in the study of the 'liquid'-like granular flows, with the development of the so-called Inertial number theory. So although applied only to faster flows, that theory serves as a good starting point of the discussion of slow granular flow theories, the subject of this section. After the treatment of the fast flow theory, we will give an overview of essential characteristics that slow granular flow theories should at least capture. Then we will discuss the theoretical framework used in the analysis of the split-bottom flows. We choose to treat this geometry here, since it is the geometry we will be using in our experimental exploration of slow granular flows in the rest of this thesis.

1.5.1   Fast Flows

In describing fast dry granular flows, such as steady granular flows down an incline, much progress has been made in recent years. For a comprehensive review, see Ref. [2]; in this section we will give a brief overview of the main results. In fast granular flows, large flowing zones are observed, and simple, steady state fluid properties emerge. Microscopically, momentum exchange in these fluid-like flows takes place by a mixture of collisions, as in the granular gas, and enduring frictional contacts.

The inertial number -- It turns out that the only simple dimensionless parameter one can construct with the variables playing a role in these flows, is the inertial number[1]: the local pressure P, the strain rate $\dot{\gamma}$, the particle diameter d and the particle density ρ can be combined to give:

$$I = \frac{\dot{\gamma}d}{\sqrt{P/\rho}}.$$ (1.11)

This number characterizes the local 'rapidity' of the flow. One particularly elegant interpretation views it as the ratio of two timescales in granular flows: $\dot{\gamma}$ is a timescale set by the flow rate, and $d/\sqrt{P/\rho}$ is the timescale a particle needs to travel over its own diameter in free space, given that it is subjected to a force Pd^2 -- it is the timescale at which granular rearrangements take place in a semi-dilute granular flow, where the weight that exerts a pressure P on a

---

[1]Assuming the particle are hard, otherwise particle elasticity becomes relevant [44].

19
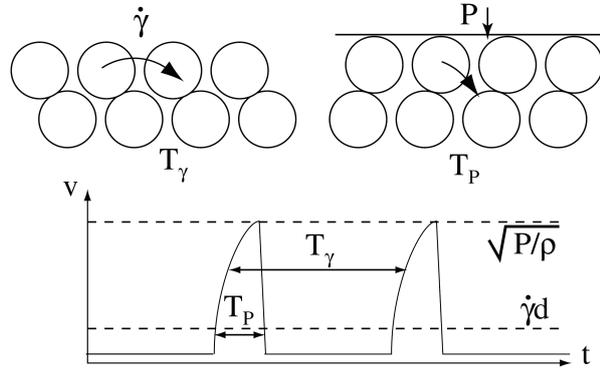
Figure 1.11: The rearrangement process of a particle inside a granular flow. $T_{\dot\gamma}$ is the rearrangement timescale, T_P is the confinement timescale. Figure reprinted with permission from Ref. [12]. Copyright (2004) by EDP Sciences.

particle is sometimes not balanced by the presence of another particle, which also implies or requires that there is space for particles to move around. See Fig. 1.11.

Shear stress -- The local stress in these flows is proportional to the local pressure. Assuming that the local dissipation is still predominantly frictional, one writes for the local stress τ:

$$\tau = \mu(I)P, \tag{1.12}$$

with $\mu(I)$ an effective friction coefficient that depends on the inertial number. $\mu(I)$ is an empirical function of I, and involves material parameters:

$$\mu(I) = \mu_s + \frac{\mu_2 - \mu_s}{I_0/I + 1}. \tag{1.13}$$

The friction coefficient μ starts at μ_2 in the limit of very small strain rates, where only frictional interactions play a role. Note that μ_2 is an effective friction coefficient, not necessarily equal to the interparticle friction coefficient μ_p. $\mu(I)$ increases around I_0 to its maximum value μ_s. Typical values of I_0 are around 1.

This local relation between stresses, strain-rates and I then successfully captures many aspects of these rapid granular flows [12], and can even be generalized to three-dimensional flows [2, 45].

The three-dimensional generalization gives a good intuition for the type of flow behavior that the inertial number theory predicts at small strain rates. The

stress tensor in three dimensions is given in the following form:

$$\sigma_{ij} = P\delta_{ij} + \tau_{ij}, \tau_{ij} = \eta(|\dot{\gamma}|, P)\dot{\gamma}_{ij}, \tag{1.14}$$

with δ_{ij} the Kronecker delta and $\dot{\gamma}_{ij} = \partial u_i/\partial x_j + \partial u_j/\partial x_i$ the full strain rate tensor; u_j is the velocity component in direction j. The viscosity η in this framework varies throughout the material in the following way:

$$\eta(|\dot{\gamma}|, P) = \mu(I)P/|\dot{\gamma}|. \tag{1.15}$$

The notable feature in this equation is the dependence of the viscosity on the modulus of the strain rate $|\dot{\gamma}|$ -- in the limit of slow flows, the viscosity diverges. This feature lets the inertial number theory capture the property that granular materials have a yield stress $\tau_Y = \mu_s P$; only if $\tau > \mu_s P$, flow is possible.

Dilatancy -- The local volume fraction Φ of a flowing zone depends on the inertial number , and typically decreases from Random Close Packing [46] at small I to values around 0.7 [23] in two dimensions and as low as 0.55 [2] in three dimensions at large I.

Taking dilatancy into account in modeling of granular flows is not always necessary: in the three dimensional generalization of the inertial number-based model, good quantitative agreement between numerics and experimental results were obtained [45] even though the small density variations throughout the shearing layer were neglected. However, dilatancy effects can be used to capture transients in granular flows, for example for submersed flows [47], and they are also used to describe an instability in inclined plane flows [48].

1.5.2 Slow Flows -- General Considerations

Soil mechanics is a natural starting point to describe rate independent flows, since in this limit, the microscopics are dominated by enduring frictional contacts. Both rate independence and the emergence of (narrow) shear bands are consistent with a Mohr-Coulomb picture where the friction laws acting at the grain scale are translated to the stresses acting at coarse-grained level. The idea is that when ratio of shear to normal stresses is below the yielding threshold, grains remain quiescent, while in slowly flowing regions the shear stresses will be given by a (lower) dynamical shear stress.

This way of thinking readily captures the maximal slope of dry sand piles. However, the steep gradients associated with narrow shear bands are difficult to capture by a continuum theory, and shear bands often are described as having

zero width [41]. Another difficulty for continuum models is that the width of the shearbands usually depends simply on the grain scale, and is therefore thought to disappear in the continuum limit [49], where one takes $d \rightarrow 0$.
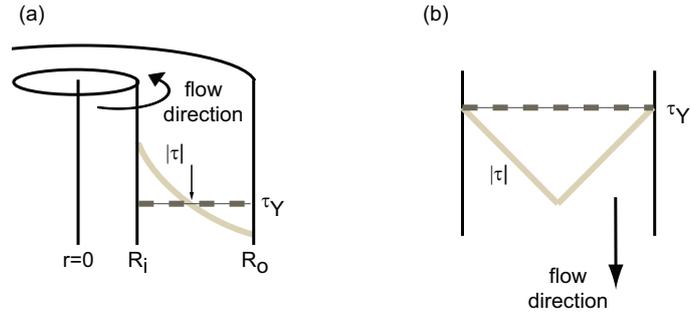
Figure 1.12: The stress field in two flow geometries. (a) Couette; (b) chute flow. Light grey indicate the locally applied stress, the dark grey dashed line indicates where the macroscopic yield stress is. At the arrow, the local stress drops below the yield stress.

Constitutive equations -- For the rate independent regime, obviously constitutive relations based on relating stresses and strain rates are unlikely to capture the physics, as they do so successfully in the inertial regime.

This was for example shown in Ref. [23]. There they obtained numerically the local strain rates in a Couette geometry. For steady Couette flow, continuum mechanics gives the form of the stress component $\sigma_{r\theta}$ distribution in the gap:

$$\sigma_{r\theta}(r) = \sigma_{r\theta}(R_i)(\frac{R_i}{r})^2, \qquad (1.16)$$

from conservation of torque. $\sigma_{r\theta}(R_i)$ is the stress exerted by the inner wheel. This stress profile is shown in Fig. 1.12a. In the Couette geometry, the local strain rates can then be compared to the local stress, to see if any constitutive equation $\tau(\dot{\gamma})$ can be found. For slow driving, it was found that this is not possible [23]. Interestingly, for moderate to fast driving, a Bingham relation between the local stress and strain rates

$$\mu(I) = \mu_{min} + bI, \qquad (1.17)$$

with b a constant was obtained. This is expected based on the behavior of $\mu(I)$ for low to intermediate I -- see Eq. 1.13 and Fig. 10 in Ref. [23].

(a)   1 second   (b)   1 minute   (c)   1 hour
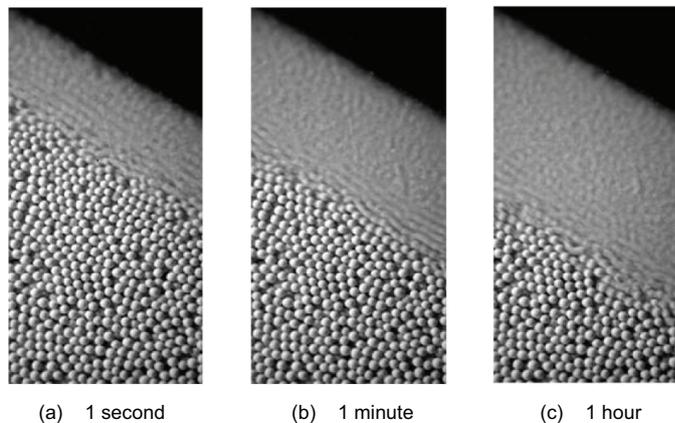
Figure 1.13: Creeping flow deep into a heap, onto which beads are continuously poured onto. After hours of flow at the surface, motion of the particles is observed even deep into the pile. Figure reprinted with permission from Ref. [50]. Copyright (2001) by the American Physical Society.

Yield stress -- Another profound problem in slow granular flows is that locally, flow can occur, even though the local stress has dropped below the global yield stress. This is evident in heap flow experiments, where even deep into the pile purely exponential flow profiles are observed, as was shown convincingly by Komatsu [50] (see Fig. 1.13), and experimentally confirmed over 6 orders of magnitude in flow rate in Ref. [43] by means of both Particle Image Velocimetry (PIV) and light scattering methods. The exponential profiles suggest that the flow goes smoothly to zero at the boundary of the flow geometry, instead of abruptly at the yield stress.

The role of fluctuations -- The failure of local rheologies for slow flows has stimulated the formulation of several non-local rheologies. A Kramer-Eyring transition state theory of activation rate process was invoked [28] in chute flows. This is a reasonable first guess, due to the particular form of the stress profile in the chute flow geometry. This stress profile is shown in Fig. 1.12b. Close to the wall, the stress τ on the granular flow is close to the yield stress of the material, which leads to zero shear velocity at the walls. Small fluctuations in the stresses close to the wall could then cause the material to intermittently experience stresses above the yield stress there, allowing local flow near the boundary. This physical picture was used to explain the exponentially localized shearbands, although the experimental resolution was not good enough to test the model

23

in great detail.

Other models invoking granular fluctuations were also proposed, for example a granular temperature in Ref. [20] to explain the shape of velocity profiles observed in Couette flows, or randomly varying local material failure strength [38, 51] to explain the finite width of the shearbands in the split-bottom geometry. Bazant put forward his 'spot'-model, which is based on the assumption that slow, dense granular flows are best described with a diffusion of low density regions in the material, called *spots* [52]. The two-dimensional model describes flow profiles in chute flow and Couette geometries reasonably well. However, recently it was shown [53] that the very structure of this model is incapable of capturing the observed velocity profiles in the split-bottom geometry.

1.5.3 Slow Flows -- Split-Bottom

The flows in split-bottom geometries have been simulated both by molecular dynamics simulations [34, 36, 39] as well as by contact dynamics [37], and a wide number of theoretical approaches have been put forward, including the spot model [54] and various other stochastic flow models [38, 51]. We briefly discuss some of these approaches here.
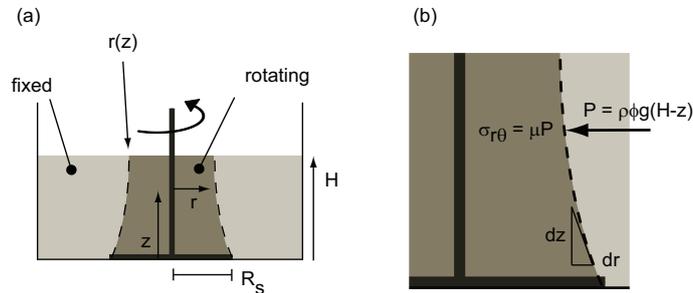
Figure 1.14: (a) An arbitrary shear zone of zero width $r(z)$ separates a rotating inner core and a static outer body. In (b): The frictional stress $\sigma_{r\theta} = \mu P$ on the shearing surface can be integrated to give the total driving torque necessary to rotate the disk in red. The integral is given in Eq. 1.18.

Variational principle -- The first attempt to describe the flows in split-bottomed geometries goes back to Unger and coworkers [41]. The flows are treated in a Mohr-Coulomb fashion, with shear bands of zero width. The idea is

to minimize the energy dissipation needed to sustain the flow. Calculating the total friction along the shear-sheet $r(z)$ using assumptions of constant friction coefficient μ and hydrostatic pressure P, amounts to finding the minimum of the functional

$$T(H) = 2g\pi\rho\Phi\mu \int_0^H (H-z)r^2 \sqrt{1 + (dr/dz)^2} dz \qquad (1.18)$$

Here ρ is the bulk density of the particles, Φ is the average packing fraction ($\sim$ 0.59 [2]) and μ is the effective friction coefficient. Identifying $r(z)$ with the center of the shearband $R_c(z)$, minimizing Eq. 1.18 gives predictions for the location of the shearbands in the split-bottom geometry. The location of the shear zones predicted for shallow layers are very close to those observed, and for deep layers the model predicts a hysteretic transition to dome-like shear. Hence, while a number of aspects of split-bottom flows can be captured already by this simple model, the hysteretic transition and zero width of the shear bands are clearly in contrast to experimental findings.

In subsequent work [51], this minimal dissipation model was extended by combining the variational principle with a self organized random potential as follows. At any given time, the shear band is still represented as having zero width. However, the granular material is now taken to be inhomogeneous, with a local strength field which varies with space and is updated every timestep. At any given time the surface that minimizes the torque can be obtained, after which the strength field is updated etc. A smooth flow profile is then obtained by averaging over the different shear bands. The resulting flow fields are very close to those observed experimentally, with the only adjustable parameter controlling the effect of disorder. One possible point of criticism is that the model assumes that the fluctuating shear bands are radially symmetric (see [38] for details).

Inertial flows -- Jop performed simulations of flows in a cylindrical split-bottom setup [55], using the 'inertial number' theory described in section 1.5.1. The location of the shear zones in the bulk, the smooth transition to precession and the dome flows were all recovered. The width of the shear zones was found to scale with driving rate as $\Omega^{0.38}$, and indeed for slow flows the shear zones attain zero width. The inertial model therefore does not fully capture the physics of the slow split-bottom flows, but it does slightly better than Ungers original model [41] in that it captures the smooth transition to precession.

Chapter 2

Dry Split-Bottom Flows: Singularities and Rheology

2.1 Introduction

In this section we probe the rheology of granular media in split-bottom geometries. The flow profiles in the rate independent regime have been studied extensively as we discussed in chapter 1, but here we extend those studies to the rate dependent regime. Moreover, we perform the first rheological measurements in this geometry, relating the driving torque T and driving rate Ω. Even in the rate independent regime this is unexplored territory, and given the rich flow structure in these systems, the dependence of T on filling height H is non-trivial.

We start by introducing our flow geometry in section 2.2. The main differences are that the outer container now is a square box (this does not influence the flow), and that the driving disk is slightly elevated with respect to the bottom plate, without allowing particles under the disk -- this makes the rheology well defined by controlling the sharp gradients near the split.

In section 2.3 we present our flow profiles and stress measurements. First of all, in the rate independent regime we find good agreement between the measured $T(H)$ and that predicted by the torque minimization argument of Unger *et al.* [41] -- this allows us to measure the effective friction coefficient from rheology. Second, we probe the onset of rate dependent behavior by quantifying the changes in the flow profiles (widening and inward shift of the

shear bands for small H/R_S, and increase in axial slip for larger H/R_s) and by the increase in torque. In addition, the normal force exerted on the disk also varies with driving rate, decreasing for small H/R_s and increasing for large H/R_s. Third, for rotation rates larger than $1\ s^{-1}$, the surface develops a depression in the center.

In section 2.5 we discuss the effect of the narrow slit for the rheology. This discontinuity of the driving can, in principle, lead to problems, although we will show that for the flow geometry discussed in sections 2.2 and 2.3 these problems do not occur. The first potential problem is that grains might get stuck, either in the gap between disk and bottom, or might be caught between their rough boundaries -- we find evidence that the latter problem plays a role for split-bottom geometries, where the roughness extends all the way to the edge of the disk (the typical case of grains glued to disk and bottom plate) and where the disk is flush with the bottom plate. Neither problem occurs in the flow geometry discussed in sections 2.2 and 2.3. The second problem can be thought of as hydrodynamic: the strain rates diverge near the split. In practice this singularity is cut off by the grain scale. We show experimentally that in a different flow geometry, where a disk is freely rotating in a bucket of grains and where this singularity does not occur, very similar flow profiles and torques are measured. Hence, this singularity does not dominate the behavior.

2.2   Elevated Disk Split-Bottom Setup

In this section we will describe rheological measurements on split-bottom granular flows. We have developed a flow geometry that allows for precise measurements of the driving torques necessary to sustain a certain flow rate, as well as to perform direct imaging of the surface flow profiles. Flow and torque measurements for deep layers ((H/R_s) of order one), and for rate dependent flows (Ω of order one rps) are possible, as well as measurements of the pressure exerted on the driving disk. The flow cell is water tight, which allows to do similar measurements in suspension flows, as described in subsequent chapter 5. In all experiments described in this chapter, we used dry polydisperse black soda-lime glass beads (Sigmund Lindner 450X-007-L), with diameters between 2 and 2.5 mm (unless otherwise stated), and a bulk density of 2.58 $\times 10^3$ kg/m^3.

Flow visualization setup -- Surface velocity profiles of can be measured in the setup depicted in Fig. 2.1a. The granular medium is contained in a square transparent box with an inner width of 150 mm and height of 120 mm. In the center of the box there is a recession in the bottom plate; the radius of the
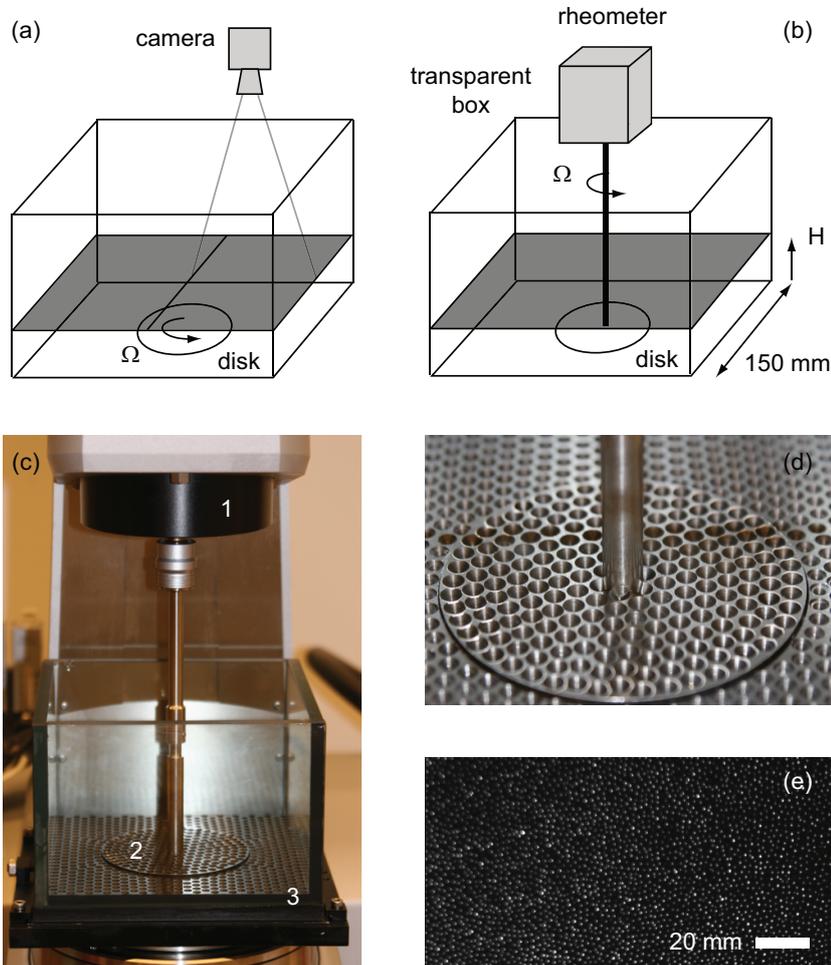
Figure 2.1: Elevated disk split-bottom setup. (a,b) Schematic overview of geometry suitable for imaging (a) and rheological measurements (b). (c) Picture of the actual setup, with 1: rheometer; 2: disk; 3: glass box. (d) Close up of the disk, showing the patterned holes that constitute the roughness of the disk and bottom plate. (e) Typical image of the surface used in the determination of velocity profiles.

recession is 0.1 mm larger than 45 mm, and about 10 mm deep. In the recession the driving disk with radius $R_s = 45$ mm is mounted. Both disk and bottom are rough to ensure a no-slip boundary condition (Fig. 2.1d). The roughness is

created by drilling conical indentations of 5mm in diameter and maximal depth of 6 mm. These are arranged on a honeycomb lattice with a maximum distance of 5 mm; for particle size below $\sim$ 5-6 mm, the spacing of the lattice, this does not induce significant crystallization.

The disk in this setup is driven from below with a stepper motor (Lin Engineering 5718L-01P) and a microstepping driver (CDR-4MPS); the number of steps per revolution is set to 51200 for smooth rotation of the disk. We image the granular (free) surface with a Basler A622f B/W FireWire camera (12 bit, 1280x1024 pixels), connected to a PC with frame grabbing software (DAS Digital Image Archiver System[1]). We use a fiber light source (Thorlabs OSL1-EC) to illuminate the surface; a typical image is shown in Fig. 2.1e. A sequence of these images can be used to extract surface velocity information with the particle image velocimetry technique discussed in appendix 8.

Rheological setup -- The flow geometry for the rheological experiments is identical in dimensions and roughness to that of the flow visualization setup. We drive the disk and perform the rheological measurements with a rheometer (Anton Paar MCR 501) in which the custom-built split-bottom cell is mounted. The rheometer is shown in Fig. 2.1c; number 1 in that figure is the rheometer head. We can raise the disk slightly above the surface of the static bottom to create an elevated disk split-bottom geometry -- typical disk elevations are 1 mm (Fig. 2.1c,d)

2.3   Flow: Profiles and Structure

In this section we investigate the onset of rate dependence in split-bottom flows. In section 2.3.1 we present data on the dependence of the surface flows on Ω, and find that rate dependence becomes detectable for $\Omega \approx 0.1$ s^{-1}, although the changes in surface flows are relatively mild. We turn our attention to rheological measurements in sections 2.4.1 and 2.4.2. In 2.4.1 we measure the driving torque as function of filling height H in the rate-independent regime, to test a prediction from the theoretical work of Unger *et al.* [41]. In section 2.4.1 we turn our attention to the dependence of the driving torque and normal forces on flow rate. In section 2.4.2 we report on correlations between the fluctuations of the driving torque and normal forces.

---

[1]From DVC Machinevision, Breda, The Netherlands; www.machinevision.nl
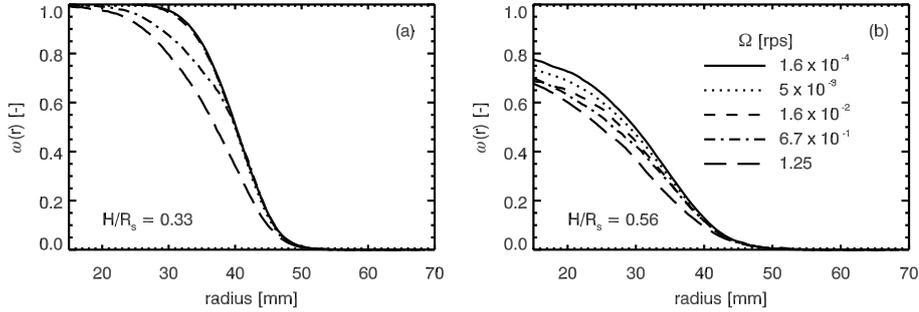
Figure 2.2: Flow profiles for two different filling heights $H/R_s = 0.33$ (a) and 0.56 (b). Linestyle depends on rotation rate, the legend applies to both panels.

2.3.1   Surface Flow Profiles

We determine the surface flows with the Particle Image Velocimetry (PIV) technique discussed in appendix 8.1. We measure the flow profiles over more than four decades in flow rate Ω, from 1.6×10^{-4} to 1.25 rps, for a range of filling heights: $H/R_s = $ 0.11, 0.22, 0.33, 0.44, 0.56, 0.67, 0.89, 1.0 [2]. We find that for low filling heights, the shear zone tends to broaden and migrate inwards with increasing rotation rate, as illustrated for $H/R_s = 0.33$ in Fig. 2.2a. Once precession (or axial slip) becomes appreciable, the shear zones develop an asymmetry with driving rate. Moreover, their center, defined as their inflection point, first moves inwards, then outwards, as shown in Fig. 2.2b. The amount of axial slip also increases markedly with Ω.

To further characterize the rate dependence of the flow profiles, we fit these to error functions as in Eq. 1.3 , and extract the axial slip $\omega(r = 0, z = H)$, the width of the profile W, and the center of the shear band R_c. We show the results of this in Fig. 2.3.

Our data for the axial slip at the surface as a function of filling height for slow flows (Fig. 2.3a) are consistent with earlier data [34]: $\omega(r = 0, H) \sim \exp(-H/R_S)$. We see no strong rate dependence in the axial slip -- Fig. 2.3b.

The width of the shear bands increases with driving rate as shown in (Fig. 2.3c). Jop modeled split-bottom flows with the inertial number based rheology for granular flows (see section 1.5.3), and found that the width of the shearband approximately scales as $W \sim \Omega^{0.38}$ [55]. Clearly, such models miss the

---

[2]We use frame rates between 33 mHz and 33 Hz. We obtain surface flow profiles as in Fig. 2.11. The interframe steps are 1 for all experiments but the largest filling heights, since at larger filling heights the surface flow becomes prohibitively slow.
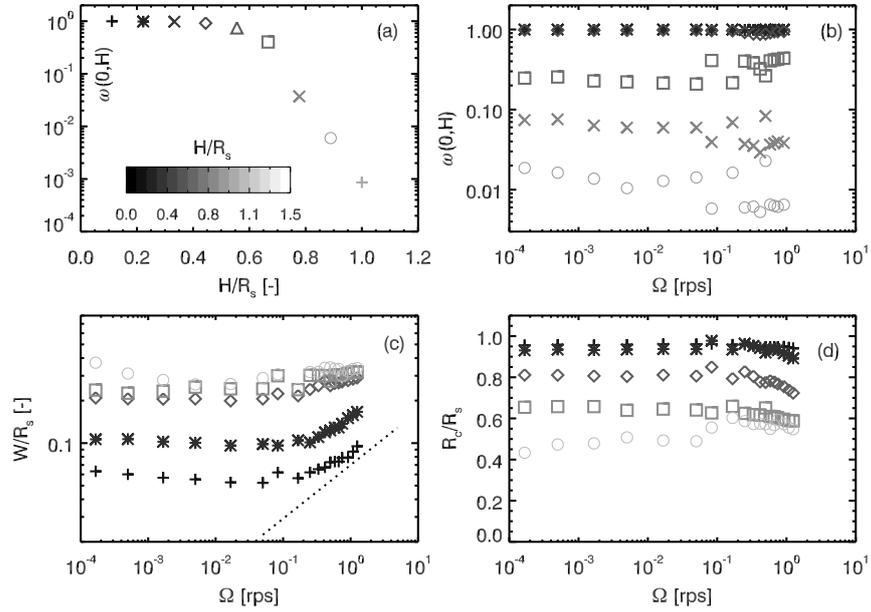
Figure 2.3: (a) The axial slip for slow flows in the rate independent regime $\Omega = 5 \times 10^{-4}$ rps. (b) The rate dependence of axial slip for a range of filling heights and rotation rates. (c) The width of the velocity profiles. The dotted line shows a power law $W \sim \Omega^{0.38}$ to allow comparison with predictions from Jop [55]. (d) The location of the center of the shear band. The different symbols indicate different filling heights.

finite and rate-independent width of the shear bands at low driving rates, but the model may capture the observed broadening of the shear bands at higher driving rate. However, the range over which we can check the validity of this scaling is very limited.

The shift of the shear bands already visible in Fig. 2.2 is shown in Fig. 2.3d. Partly because the onset of rate dependence also leads to asymmetries in the flow profiles, in particular for large filing heights, the error function fits are not very good. As a result the apparent positions R_c show considerable scatter, although the overall trends are clearly visible.
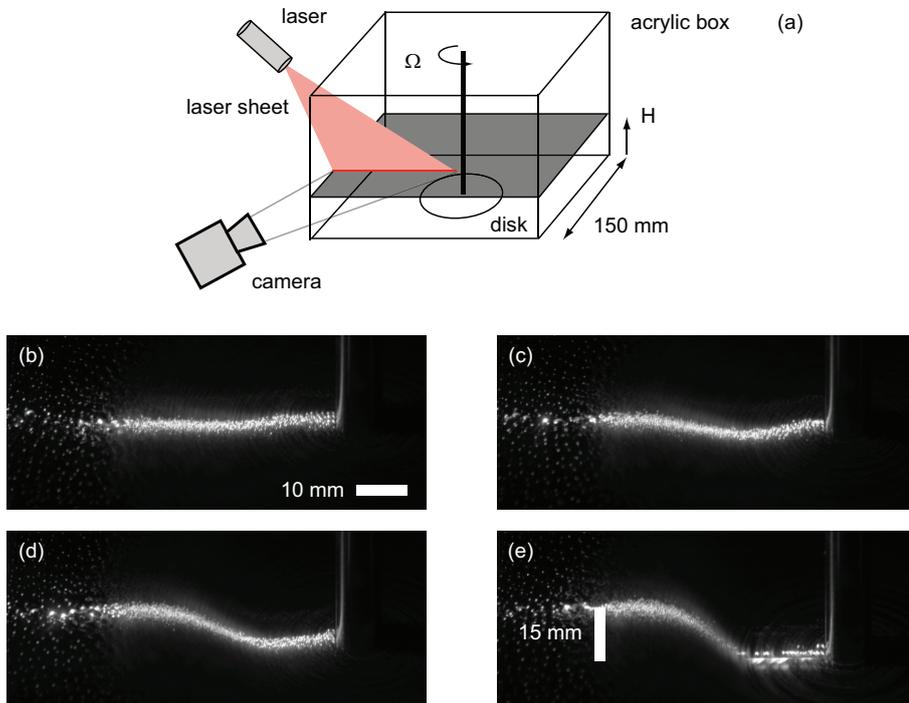
Figure 2.4: The setup depicted measures the evolution of the surface structure. Steady state surface structure snapshots for different Ω are shown in (b-e): (b): 0.7 rps; (c): 1.3 rps; (d): 2 rps; (e): 2.7 rps.In (e) the rotating disk is visible in the middle. The filling height H/R_s here is 0.3.

2.3.2   Surface Recession

For driving rates above 2 rps, where one would expect the rate dependent effects reported above to be more significant, the surface starts to develop a dip in the middle. This renders an accurate determination of the surface flow profiles difficult. This effect is reminiscent of Newtons bucket, where the transverse pressure gradient in a rotating Newtonian liquid creates a so-called paraboloid of revolution [56].

Corwin [57] explored this surface deformation effect in a variant of the split-bottom geometry where the rotating disk constitutes the whole bottom. Amongst other things, he observed that for low filling heights, the center of the system is evacuated completely at higher driving rates. For larger filling heights, this evacuation does appear.

We have probed the onset of the surface dip using the rheology setup depicted in Fig. 2.4a where a focusable diode laser (Thorlabs CPS196) behind a cylindrical lens creates a laser sheet that illuminates a line on the surface of the granular bed. We image the illuminated strip from the side and under an angle of 45° with a high-resolution digital camera (Canon EOS 20D), with an exposure time long enough to blur the otherwise patchy and scattered line of laser light. The results for $H/R_s = 0.3$ ($H = 12$mm) are shown in Fig. 2.4b-e, showing the development of the surface dip.

The onset of this effect can be estimated by comparing when the centrifugal force $F_c = mv^2/R_s = m(2\pi\Omega)^2 R_s$ becomes larger than $\mu m g$, the maximum radial frictional force a particle can bear under its own weight. These two terms equate for $1/2\pi\sqrt{\mu g/R_s} \sim 1.8$ rps, using a typical value of 0.6 for μ. Note that for high enough Ω, the center region indeed gets completely evacuated, in accordance with the observations from Corwin [57].

2.4 Rheology

2.4.1 Rate Independent Regime
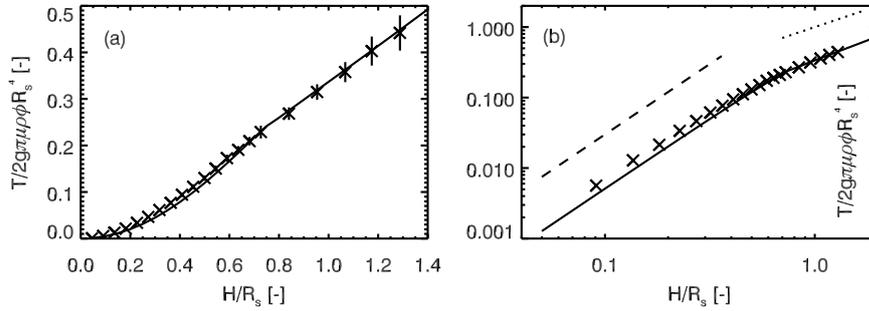
Figure 2.5: (a,b) A comparison between the numerically obtained $T(H)$ (line), and experiments ($\times$). The error on the average torque values is shown with the vertical bar through the data. The dashed line in (b) corresponds to $T \sim H^2$, the dotted line to $T \sim H$.

Due to the non-trivial structure of the flow profiles in the split-bottom geometry, the driving torque depends non-trivially on the filling height, even for slow, rate-independent flows. The procedure introduced by Unger (see section

1.5.3) minimizes the functional

$$T(H) = 2\pi\mu\rho\Phi g \int_0^H (H - z)r^2 \sqrt{1 + (dr/dz)^2} dz, .\qquad(2.1)$$

Here ρ is the bulk density of the particles, Φ is the average packing fraction (~ 0.59 [2]) and μ is the effective friction coefficient -- only the product of these three is relevant for the precise value of the torque T. Minimizing Eq. 2.1 not only leads to a good prediction for the position $R_c(z)$ of the center of the shear bands but also predicts the driving torque T as a function of the height H.

This prediction for the torque has not been tested experimentally. We have measured the average torque necessary to sustain a rotation rate of $\Omega = 1.7 \times 10^{-2}$ rps (clearly in the rate independent regime) over two full rotations, for filling heights $H/R_s = 0.085$ to 1.5. We performed the experiments in the setup described in section 2.2.

The resulting data is shown in Fig. 2.5 and compared to the theoretical predictions obtained by minimizing the functional Eq. 2.1 numerically. We have fixed $\rho = 2.85 \times 10^3$ kg/m^3, $\Phi = 0.59$ and have adjusted μ to obtain an optimal fit -- this yields $\mu = 0.47 \pm 0.03$ -- the error is due to the uncertainties in Φ, ρ and experimental noise in the determination of T. The simple model describes the experimental data rather well. The minimization procedure predicts quadratic behavior of $T(H)$ curve for small H/R_s. This crosses over to linear behavior for larger filling heights, where precession sets in. Indeed, above $H/R_s = 0.7$ we see a profound change in the curvature of $T(H)$: above this critical filling height, $T(H)$ is essentially linear in H.

2.4.2 Rate Dependent Regime

We measure the average driving torque necessary to sustain a flow over more than three decades in Ω, from 1.6×10^{-3} to 1.25 rps, for five different filling heights: $H/R_s = 0.25, 0.35, 0.45, 0.55, 0.75$. In each experiment at fixed filling height, the rotation rate is swept from low to high; a reverse sweep gives similar results as long as the averaging timescales are long enough to allow transients to die out.

The results of the rheological experiments are shown in Fig. 2.6. In Fig. 2.6a,c we plot the average normal forces acting on the disk; in Fig. 2.6b, d we show the average driving torques necessary to sustain rotation of the disk.

In the normal forces, we can observe several trends: for large filling heights, no rate dependence is observed at all, for Ω up to 1.25 rps. For the lower filling heights, we observe a reduction of the normal forces acting on the disk for $\Omega = 1$ rps and higher. This is due to the fact that at these rotation rates, the centrifugal
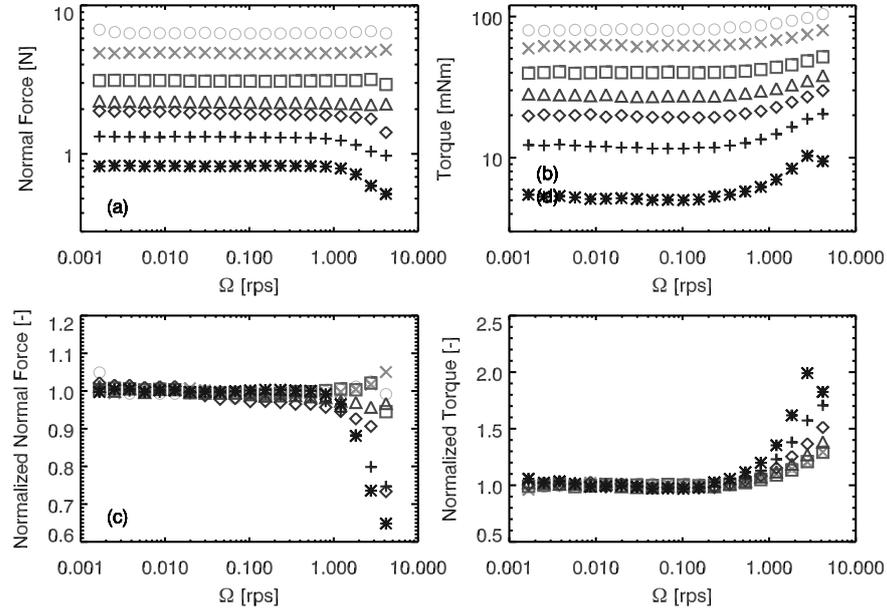
Figure 2.6: Averaged normal (a,c) and shear (b,d) forces measured at different Ω. Different H/R_s are indicated with symbols: 0.19; + 0.29; $\diamond$ 0.43; $\triangle$ 0.52; $\square$ 0.72; $\times$ 1.12; $\circ$ 1.52. In panel (c,d) the data is normalized by the average of the first 10 data points in the rate independent regime.

force is large enough to move particles in the radial direction -- the reduction of the normal forces is simply due to less particles resting on the disk. This phenomenon is accompanied by a change in the surface structure of the flow which will be discussed below.

The driving torques show more pronounced rate dependence. For all filling heights, the rate dependence sets in around 0.5 rps, and leads to an increase of the driving torque -- this increase is relatively largest for small filling heights.

2.4.3 Stress Fluctuations

During shear, the stresses fluctuate, and we have measured the normal and shear stresses exerted on the disk for a constant rate in the rate independent regime ($\Omega = 1.7 \times 10^{-2}$ rps), for a range of filling heights: $H/R_s = 0.05$ - 1.5. We sample the forces at 10 Hz, over two full rotations, amounting to 120 seconds. We ignore the first 20 seconds of each data set.
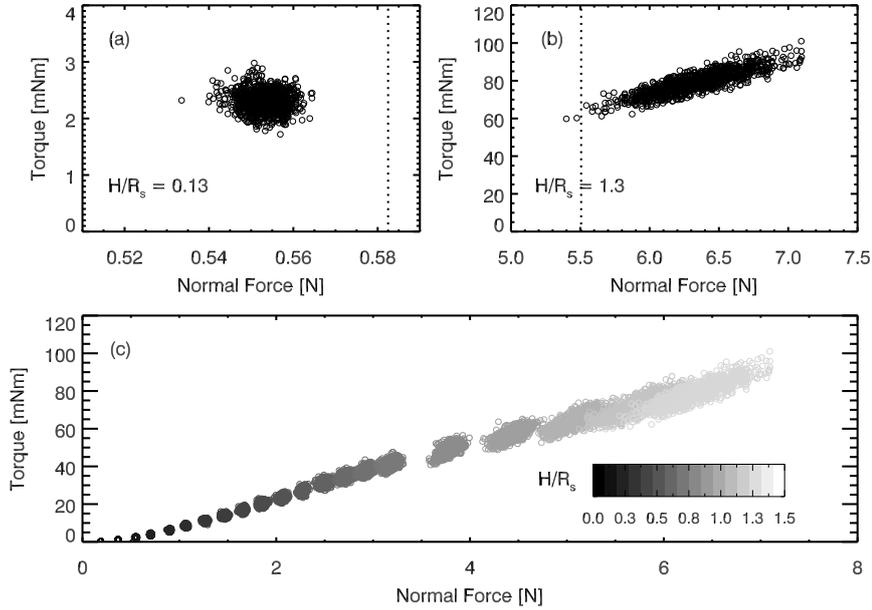
Figure 2.7: (a,b) Normal and shear forces for two filling heights, measured under continuous rotation with $\Omega = 1.6 \times 10^{-1}$ rps. The dashed line indicates the normal force one would expect based on the weight of the grains present in the cell. In these plots, larger normal forces correspond to larger weights pressing on the disk. (c) Scatter plots as shown in (a,b), here shown for all filling heights.

In Fig. 2.7a,b we present scatter plots of the torque T vs normal force N for $H/R_s = 0.13$ and 1.5. These illustrate that for low filling heights N and T are uncorrelated. The normal force deviates a few percent from the weight of the grains resting on the disk, but we attribute this to inhomogeneities in the packing density. Note that the fluctuations in the instantaneous torque are substantial.

For the large filling height data shown in Fig. 2.7b, the shear band has collapsed into a dome above the disk, and T and N display considerable correlations. Notice that for the dome shape, fluctuations in the normal stresses across the shear band can be expected to be picked up by the normal force exerted on the disk, while this is not the case for the shear bands on the shallow case. Hence, similar correlations between normal and shear stresses may also arise for shallow filling heights, but our probe is not sensitive to this.

In this regime the fluctuations of the normal force are substantial, and the instantaneous normal force is always substantially larger than the normal force based on the weight of the grains (dashed line). This suggests that the normal force can be seen as due to the sum of the weight of the grains and a dynamically generated normal stress, related to the dilatancy of the grains and the shear stress.

Fig. 2.7c presents a scatter plot for all filling heights, illustrating the occurrence of a linear correlation between the normal and the shear force for all $H/R_s \gtrsim 0.6$.
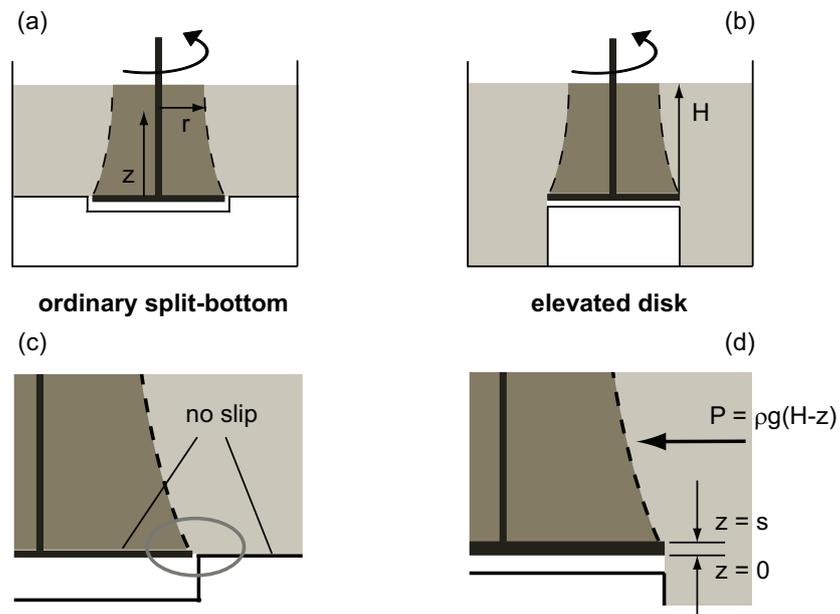
Figure 2.8: (a) A schematic drawing of the standard split-bottom geometry, and (b) of the disk geometry. (c) In the region emphasized by the oval, the strain rate is diverging at $z = 0$, $r = R_s$. (d) In the disk geometry, grains touch the smooth side of the disk between $z = 0$ and $z = s$, with s the thickness of the disk.

2.5 Flow Singularity

The discontinuity in the driving in the split-bottom geometries is a potential obstacle for doing rheology of such flows. In this section we compare the flow profiles and driving torques of the flow geometry discussed in section 2.2 to two

other geometries -- a standard split-bottom geometry where the bottom and disk are made rough by gluing grains on their surfaces and the disk and bottom are flush, and a disk geometry where the disk is freely moving in the granular medium (see Fig. 2.8).

Comparing the flow profiles and rheology of these systems allows us to identify and eliminate the problems due to individual grains being stuck near the split, and due to the 'hydrodynamic' singularity that is also present on the continuum scale. To probe the rheology, we focus on $T(H)$ for moderate shear rates

We will show that the flow profiles of split-bottom geometry, elevated split-bottom geometry and disk geometry become very similar for sufficiently large filling heights. The $T(H)$ curves show differences though. We find that the standard split-bottom geometry suffers from strong rate dependence and also leads to $T(H)$ not smoothly extrapolating to zero stress for zero height. The disk geometry does not show such anomalous rate dependence, but its $T(H)$ is not described by Unger's formalism -- drag forces exerted on the side of the disk also have to be taken into account. The elevated disk geometry, used in the previous sections of this chapter has none of these problems, showing that here the flow singularity is well controlled.

Here we first present a simple argument why the grain scale effectively limits the singularity. The maximum strain rate near the split can be estimated as $2\pi\Omega R_s/d$ -- i.e. all strain is concentrated over one grain diameter. For typical filling heights (2.5 cm), R_s (4 cm), this yields that the inertial number I, defined as $\dot{\gamma}d/\sqrt{P/\rho}$ with d the particle diameter, P the local pressure, and ρ the bulk density of the particles, equals 0.5Ω. Hence, in practice the inertial number remains quite limited, and no singular rheology is expected.

2.5.1   Split-Bottom and Disk Setups

We compare the flow profiles and rheology obtained in the elevated disk geometry to two other geometries, as shown in Fig. 2.9. Both geometries consist of a transparent acrylic cylinder with an inner radius of 70 mm, with a split-bottom disk of radius R_s of 40 mm. Both the bottom plate and the top surface of the disk are made rough by gluing glass beads on them. The sidewall is not made rough, but through the transparent sidewalls we do not observe any particle motion near the walls. To avoid the singularity at the split in split-bottom flows, we introduce here a modified version of the split-bottom, called the *disk* version. Here we remove the singularity by elevating the rough disk above the outer no-slip boundary. A hollow smooth cylinder is placed directly underneath the disk, such that no particles can get underneath the disk -- we also make the
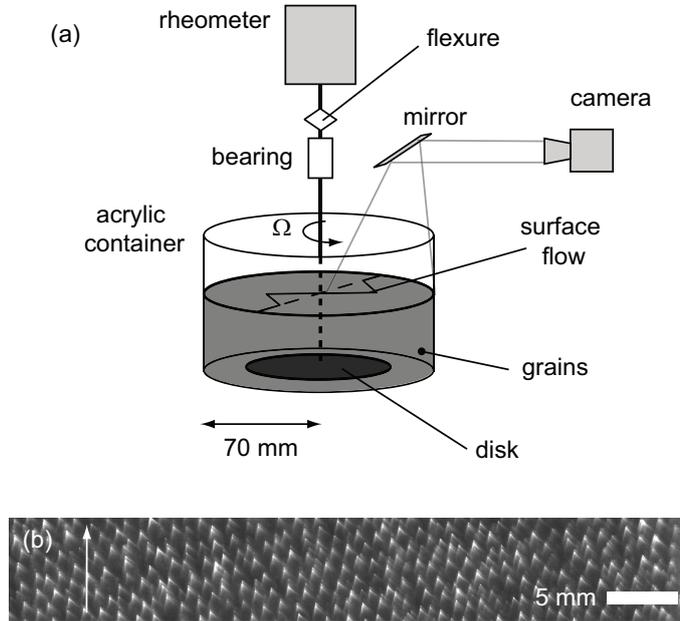
Figure 2.9: (a) The setups used to study the effect of the flow singularity. We change between the two types by replacing the bottom of the acrylic container. (b) Typical image of grain surface, with arrow indicating the flow direction.

gap between disk and the top of the cylinder smaller than a grain diameter. See Fig. 2.8b.

We use black soda-lime glass beads (Sigmund Lindner 4504-007-L), a polydisperse mixture with a diameter range from 1 to 1.3 mm. The disk is driven by a rheometer (Anton Paar DSR 301) in constant rotation mode only. The disk axis is held by a low-friction ball bearing, and the axis is connected to the rheometer via a custom built flexure with a stiffness of 4 Nm/rad. We observe surface flow in the cell with an 8 bit camera (Basler A101f) via a mirror. We extract the surface velocity profiles with particle image velocimetry (PIV) -- see appendix 8.1. The particles are illuminated with a fiber light source (Thorlabs OSL1-EC). The light source used is a, to a good approximation, a bright point source -- this aides the PIV technique in creating high contrast in the images.

40
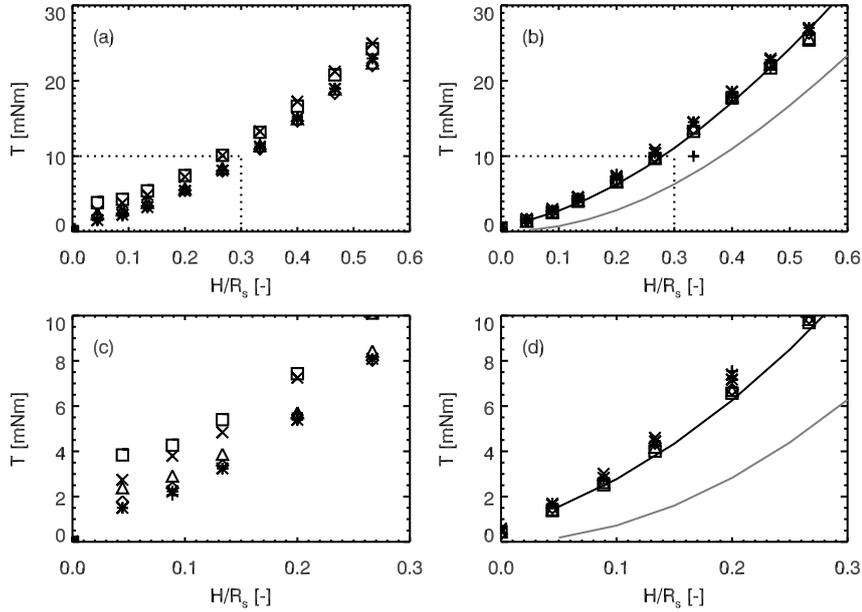
Figure 2.10: The different rheologies of ordinary split-bottom (a,c) and disk (b,d) geometries. Symbol legend: rotation rates Ω [rps] + 5×10^{-4}; 1.7×10^{-3}; $\diamond$ 1.7×10^{-2}; $\triangle$ 1.7×10^{-1}; $\square$ 5×10^{-1}; $\times$ 1. (c,d) show details of the main panels (a,b) as indicated by the dashed line.

2.5.2   Rheology of Split-Bottom and Disk Geometries

We measure the average torque $T(H, \Omega)$ necessary to sustain a constant rotation rate of the disk, for different filling heights and rotation rates. The driving torque is always averaged over at least 1 full rotation, for the highest rotation rates we average over 5 rotations. We observe that with an empty cell only very low average torques values, of the order of 0.01 mNm are necessary to sustain rotation of the disk -- the ball bearing does not influence the measurements.

The results of the experiments are shown in Fig. 2.10. Results for the split-bottom are shown in the left two plots. Results for the disk version are shown in the right two plots. For the split-bottom geometry $T(H)$ has a substantial offset for low filling heights, which moreover is strongly rate dependent; it increases threefold when Ω is increased from 1.7×10^{-2} to 0.5 rps, whereas the driving torques for the elevated disk version do not show any rate dependence here (Fig. 2.10c-d).

We believe that these anomalies are due to the sharp flow gradients near the split, and the possibility that grains get stuck intermittently here.

The data for $T(H)$ cannot immediately be fitted accurately by the numerical expression obtained from minimizing the torque, as was done in section 2.4.1. However, we can successfully capture $T(H)$ if we take into account the drag forces exerted on the side of the disk:

$$T(H) = T_U(H) + 2g\pi\rho\Phi\mu R_s^2[Hs + 0.5s^2] \,, \qquad (2.2)$$

where $T_U(H)$ is the torque obtained from the Unger model, and s is the thickness of the disk.

The black line in Fig. 2.10 is a fit of Eq. 2.2 to the data, while the grey line in this plot corresponds to the result without side-drag correction; the linear correction and offset are substantial but sufficient. The only fitting parameter in the model, even with the linear correction term included, is the effective friction coefficient μ, which we find to be $\mu = 0.57 \pm 0.03$.

2.5.3 Flow Profile Comparison

We have probed whether the flow profiles of the ordinary split-bottom cell are similar to the ones produces by the elevated-disk split-bottom cell for a rotation rate Ω of 1.7×10^{-3} rps. The normalized angular velocity profiles $v_\theta(r)/2\pi r\Omega$ are shown in Fig. 2.11a for the ordinary split-bottom geometry and in Fig. 2.11b for the disk geometry. The only significant point to note is how to define H in the disk geometry: only if we measure H from the *underside* of the disk, so at $H + s$, the flow profiles will overlap -- see Fig. 2.11d. This height correction works well for all other filling height with $H/R_s > 0.15$.

2.6 Discussion and Conclusions

In this chapter we have studied the rheology and flow profiles of dry granular flows in the split-bottom geometry, in both the rate independent, as well as the rate dependent regime of flow rates.

Rate independent regime -- We have seen that the large strain rates above the split between the two no-slip boundaries in the original split-bottom [31] can lead to problems when measuring the rheology in this system. We devised a modified version which we refer to as the elevated disk setup, which shows all the interesting flow phenomenology of the ordinary split-bottom geometry, but also allows for rheology experiments.
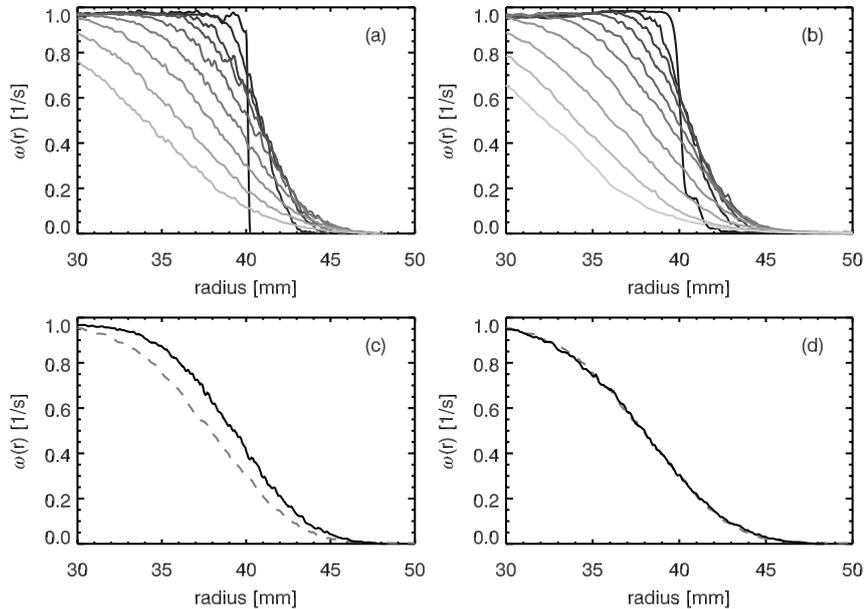
Figure 2.11: The normalized angular velocity profiles measured in the two different split-bottom geometries: (a) split-bottom, (b) free disk. (a,b) Shows all velocity profiles. Lighter color correspond to larger filling heights; the range is $H/R_s = 0$-0.53. c shows the velocity profiles for $H/R_s = 0.38$ for split-bottom (black) and free disk (dashed grey). In (d) the velocity profiles for $H/R_s = 0.38$ are again shown, now taking into account the correction for H necessary in the free disk type of the split-bottom (see text).

We test the Unger model prediction for $T(H)$, the height dependence of the driving torque in the rate independent regime. We do this for both small and large filling heights, and find good agreement between the prediction and the experimental results.

Rate dependent regime -- In the rate dependent regime, we measured rheology and flow profiles in the split-bottom geometry. While both flow profiles and rheology show rate dependence, the range is rather limited because for $\Omega > 1$ the surface develops a depression in the center region due to the centrifugal forces.

Finally we wish to suggest a simple argument for determining both the shift

of the center location of the shear zones and the increase in torque. The idea is to extend Ungers model with a rate dependent friction, and to model this rate dependence like is done in the inertial number framework. Hence, we should calculate $I = \dot{\gamma}d/\sqrt{P/\rho}$ with d the particle diameter, P the local pressure, and ρ the bulk density of the particles, and then replace μ by $\mu(I)$, which we approximate as $\mu(I) = \mu_0 + \mu_1 I$. We estimate the local strain rate to be proportional to the inverse of the width of the shear zones W, and we rely on earlier measurement which find that $W \sim z^{\alpha}$, with α around 1/3. In principle, both the shift of the center location of the shear zones and the increase in torque should be given by minimizing the integral:

$$T(H, \Omega) = 2\pi\rho\Phi g \int_0^H (\mu(I)H - z)r^2 \sqrt{1 + (dr/dz)^2}dz \,, \qquad (2.3)$$

$$\text{where } I \sim z^{-\alpha}/\sqrt{P} \,. \qquad (2.4)$$

Clearly, such a model contains a large number of fit parameters (in particular μ_1), but it would be interesting to see whether such model, at least in principle, can capture some of the observed phenomenology.

Chapter 3

Gravitational Suspensions:
Flow Imaging

3.1   Introduction

Granular materials are difficult to study in three dimensions because of their opacity -- only their surface is directly visible. There is however a simple technique that gives access to the bulk: index matched scanning (IMS). This technique works by immersing transparent particles in a fluid with the same optical index of refraction. This makes the resulting suspension transparent. The bulk is then visualized by adding a fluorescent dye to the fluid: when the dye is excited with a laser sheet, only the fluid will fluoresce and the particles will appear as dark spots in a bright, well defined cross section of the suspension.

In this chapter we apply the IMS technique to the split-bottom geometry, an ideal system for this purpose due to the rich three-dimensional structure [31--34] The IMS technique is still under development; the split-bottom flow experiments can serve as a test bed for the validation, of its three-dimensional imaging capabilities. On the other hand, many aspects of the three dimensional microstructure of granular flows in this and other geometries are not known, and we anticipate that IMS will play an important role in elucidating this.

In the following section, we describe how we employ the IMS technique to study granular flows in the split-bottom geometry. The basis of the IMS setup we used to do the flow structure experiments was developed in Wolfgang Losert's group at the University of Maryland. Initially, the IMS setup in that

group was designed to study the structure of static granular packs in three dimensions under thermal cycling [58]. Krisztian Ronaszegi adapted it to study shear reversal effects in the split-bottom geometry [59]. In close collaboration with the group, mainly during a two month visit in 2008, we modified the scanner to use it to study the flow of suspensions in the split-bottom geometry, and to do the experiments discussed in this chapter. The complete Maryland setup is described in section 3.2.

In the subsequent sections, we will show that IMS scanning is perfectly suited to study granular flows in the split bottom geometry. Our first goal is to check whether in the slow driving limit, the flow structure of our gravitational suspensions[1] corresponds to the flow features established for *dry* granular flows in such geometries. We verify this by comparing the flow profiles of the gravitational suspensions in the split-bottom geometry to empirically determined flow profiles of dry granular materials in that same geometry; we find an excellent quantitative agreement. This validates the IMS technique for the study of slow, dry granular flows.

Our second goal is to use the interstitial fluid, necessary for the IMS technique, to our benefit, and explore the rate dependent flow structures that ensue when the driving rate Ω is increased. As we will detail in section 3.4, the rate dependent suspension flows tend to Newtonian flows, and the crossover from the granular to the Newtonian regime is well captured by a previous scaling theory proposed by Cassar in Ref. [60]. The theory predicts that the behavior of the suspension is Newtonian near the onset of this *rate-dependent* regime. We verify the theory by numerically solving the steady state Navier-Stokes equation in the split-bottom geometry for a Newtonian rheology. The flow profiles obtained are then compared to the measured flow profiles, and we find a good agreement between the two.

3.2 Flow Measurements with Index Matching Scanning

The IMS setup we use to investigate suspension flows in the split-bottom geometry was developed in Wolfgang Losert's group at the University of Maryland. This IMS was initially developed to study static granular packings [58], for which the imaging speed does not have to be fast; its imaging rate is limited to 3 images per second. That imaging rate is however sufficiently fast to probe steady state flows in two dimensional cross sections inside sheared suspensions, for flow speeds up to 2.5 cm/s. We will refer to the setup described in this chapter

[1]We use the name *gravitational suspensions* to denote suspensions win which the density of the fluid and particles are not matched.

with setup M from now on; this will also facilitate distinguishing it from another, faster, IMS setup developed in Leiden and described in chapter 4.

3.2.1 Index Matching Setup: Version M
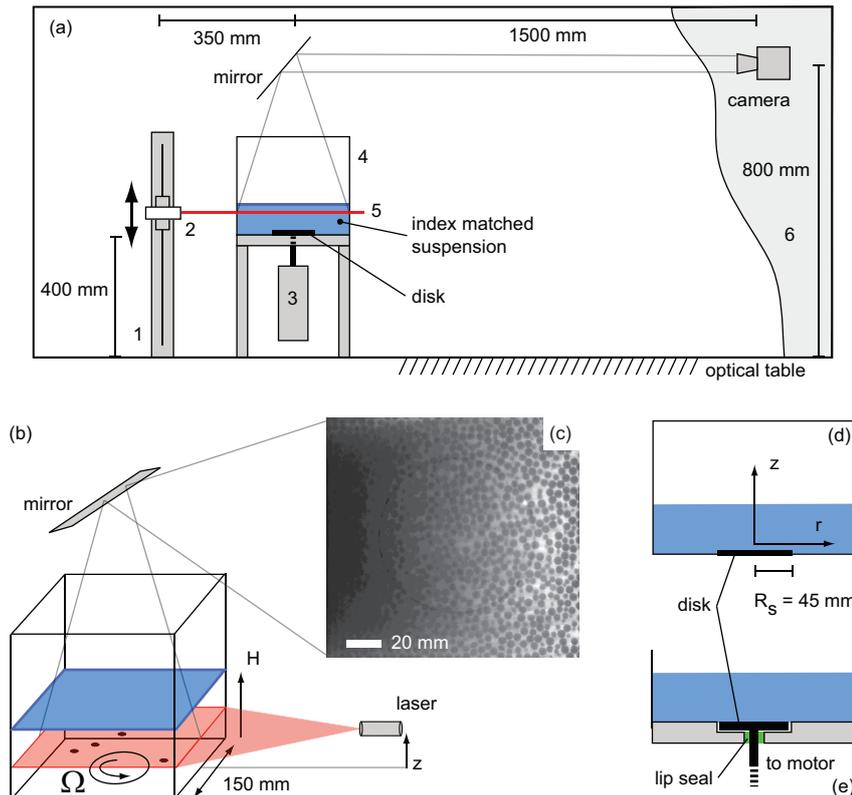
Figure 3.1: Setup M. (a) A schematic side view. 1: Translation stage; 2: Laser; 3: DC servo motor; 4: PMMA box; 5: Laser sheet; 6: Black curtains. (b) Shows a three dimensional representation of the flow cell, with the disk at the bottom. (c) Shows a typical image. The coordinate system used throughout the text is depicted in (d). In (e) the bottom, with the disk mounted in the recession is shown. The motor drives the disk from below; a lip seal (in green) ensures the cell is water tight.

The IMS scanner developed in Wolfgang Losert's group at the University of Maryland is depicted schematically in Fig. 3.1. We give the details of the setup

below:

Laser -- The scanning laser sheet is generated by a Stocker Yale (SNF-501L-635-S-35-30) 635 nm, 25mW laser. The laser has optics mounted directly on it to generate a laser sheet and to be able to focus the laser sheet. The focussing is used to adapt the distance where the sheet is at its thinnest. Typically the laser is placed at a distance of the split-bottom cell of $\sim$ 35 cm; this distance is referred to as the projection distance. The sheet is about 100 micron thick here. Laser beams display beam divergence: they are not uniform in thickness but become thicker with increasing distance to the projection distance. The distance at which the thickness is $\sqrt{2}$ thicker than at the projection distance is called the depth-of-field. At 35 cm focus this depth-of-field is at least 50 cm. This depth of field is large enough to image the whole measurement cell which measures 15 cm in diameter. The laser sheet is generated with a fixed opening (fan) angle of $30°$.

Translation stage -- The laser is mounted on a translation stage, to allow imaging of different cross sections of the suspension. The translation stage (Velmex Bislide, size 23) is driven by a stepper motor and can make 1 micrometer steps, significantly smaller than the 100 micron laser sheet thickness. The stepper motor is controlled by a computer operated stepper motor driver (Velmex VXM-1). Automated measurement cycles that involve synchronizing the motion of the laser with camera operation are therefore possible; for slow flows the time between two images required for imaging the flow is of the order of minutes, and allows for acquiring cross sections at more than one imaging position; this parallel acquisition of the two dimensional flow field at different imaging positions reduces total measurement time substantially.

Digital camera -- The computer controlled digital camera used to image the cross sections illuminated by the laser, is a Sensicam 370KL. The camera is placed at 2 meters distance of the split-bottom cell. The focal depth of the camera is set before the start of the experiment. For the camera placed at that imaging distance, the different cross sections imaged are all while the laser sheetis moved.

At such a large imaging distance, little fluorescent light is available, so pixel noise in the CCD chip becomes significant. Therefore, the CCD chip of the camera is cooled to 20 degrees below ambient. This cooling reduces the dark current and increases the quantum efficiency (QE) of the camera[2].

---

[2]The dark current is the anomalous 'detection' of photons by the pixels on the CCD chip, even

The resolution of the B/W CCD is 1280x1024 pixels, with 12 bit depth. Imaging the complete cell, which measures 15 cm in diameter, corresponds to a surface area of $\sim$ 200x200 micron per pixel. The exposure time can be adjusted between 10 microseconds to several hours. The maximum frame rate of 3 frames per second is set by the minimum amount of time it takes to transfer the images from camera memory to the computer hard drive. The lens used on the camera is a zoom lens with an aperture of 2.8.

The setup -- See Fig. 3.1a. The setup is placed on a large optical table. The optical pathway from the camera to the measurement cell is about two meters and therefore relatively large. To accommodate this large optical pathway within the confined space of a laboratory room and optical table, a mirror is used. The whole setup is shielded from external light with black curtains.

Flow geometry -- The split-bottom geometry (standard type -- see section 2.5) in which the flow takes place, is a square box of 15 cm width, and 20 cm height. The walls of the box are made of transparent PMMA[3]. The driving disk is mounted in a recession in the bottom of the flow cell. The disk radius R_s is 4.5 cm. The disk is driven from below by a DC servo motor (type) via a 1/25 gearbox. Driving rates are $\Omega = 8.3 \times 10^{-5}$ to 8.3×10^{-2} rotations per second. The hole through which the disk is connected to the motor is sealed by a lip seal, to make the box watertight; see Fig. 3.1e. To the bottom of the box, as well as to the disk, a disordered, low density arrangement of 1/8" ($\sim$ 3.1 mm) PMMA particle is glued with an epoxy glue, to make the surface rough and provide a no-slip boundary condition for particles up to about 6 mm in diameter.

Particles -- We use 3/16" ($\sim$ 4.6 mm) PMMA particles (Engineering Labs). They are spherical, monodisperse, polished transparent particles with an index of refraction n_D of 1.48-1.50, depending on the production batch. Their density is 1.18 $\times 10^3$ kg/m^3.

Index matching fluid -- As an index matching fluid we use Triton X-100, mixed with water and zinc chloride, based on Ref. [61]. The density of the fluid is around 1.08 $\times 10^3$ kg/m^3. The density difference $\rho_p - \rho_f$ between the fluid is always positive and in the range of 10-110 kg/m^3; the particles will therefore always settle when inside the fluid. The viscosity of the fluid varies slightly between

---

if no light reaches the photosensitive parts. The QE is the number of photons needed to release a single electron in the photosensitive part of each pixel.

[3]PolyMethyl MethAcrylate, also known as acryl or Plexiglas

0.2 and 0.5 Pa·s, depending on the preparation of the fluid and the amount of water evaporated. We cover 3 decades in driving rates, so this variation in the viscosity will not affect our conclusions significantly. See section 3.2.2 for more details regarding the preparation of index matching fluids.

Fluorescent dye -- In the index matching fluid we dissolve a small amount of fluorescent dye. We use Nile Blue 690; see section 3.2.2 for more details regarding the use of the dye.

Laboratory environment -- All experiments are carried out in a laboratory with climate control, hence under ambient yet constant temperature and humidity. The temperature control is relevant, since the temperature affects the viscosity of the index-matching fluid used. Evaporation of water from the solution has not been prevented, so over the course of days the density and viscosity change slightly. See section 3.2.2 for more details.

Operation -- The suspension in the split-bottom cell is imaged by placing the laser sheet parallel to the bottom of the box, at imaging position z. See Fig. 3.1b for a schematic picture of this imaging method. Since the dye inside the fluid fluoresces when excited by the laser light, the particles appear as dark spots in a bright background -- Fig. 3.1 shows a typical image. To image the flow at a particular height z, we take a 'movie' of the flow with a fixed number of images, usually 1000, with several seconds between the acquisition of two images. This is done while the disk is driving the suspension. To image the flow at different heights, the laser sheet is moved to a different height, and another sequence of images is acquired.

Analysis of data -- From the cross sections of the suspension, we obtain the velocity profiles with PIV. This method is described above in appendix 8.1

Limitations -- The flow rates that can be studied with this setup are limited from above by camera acquisition speed: the upper limit in flow speed is 2.5 cm/s, or equivalently: 5 rotations per minute = 8.3×10^{-2} rotations per second. The lower limit on the flow rates is the constraint of having a reasonable measurement time. However, the fluid stability is sometimes a limiting factor as well; see section 3.2.2. The zinc chloride precipitates in the form of small white crystals after a few days. This precipitate scatters light and makes the laser sheet disperse, whence imaging becomes progressively more difficult. Replacement or mechanical mixing of the fluid is then necessary. The laser dye also photobleaches, but this happens on longer timescales. Considering all of

the above, the lowest rotation rate we were able to attain was roughly 1 rotation per 3 hours, or 8.3×10^{-5} rotations per second.

3.2.2 Making Index Matched Suspensions

In this section we list techniques, tricks and caveats to keep in mind to accomplish index matching for Triton and PMMA particles. Matching the index of refraction of a fluid to that of a solid, as it turns out, is much more of an art than a science. We will therefore describe the methods mostly as recipes, without much supporting evidence as to why these methods work. We index matched PMMA particles with a mixture of the following components: Triton X-100 (a polymer fluid), $ZnCl_2$ and H_2O.

Composition of the fluid -- Ref. [61] states the following relative quantities that can be used for index matching: 77.9% Triton, 13% H_2O, 9% $ZnCl_2$, all fraction by weight. However, this mixture has several disadvantages: it is almost density matched[4], so the particles take a long time to settle. The mixture is cloudy, which inhibits transmission of laser light. The fluid is also very viscous[5]. In Ref. [62], we find a slightly different composition of Triton, water and zinc chloride used to index match PMMA: 92% Triton, 4.67% H_2O, 3.22% $ZnCl_2$ and 0.1% 12M HCl. Considering the literature, the precise recipe to achieve index matching is therefore ambiguous. There are two however two more considerations that make creating the right composition of constituents difficult: absorption of the fluid by the PMMA particles, and precipitation of the zinc chloride. We explain these two phenomena below.

Absorption -- Absorption of the polymer fluid can change the refractive index of the beads slightly[6]. We observe that washing and drying the PMMA particles after having submersed them in Triton often makes them develop cracks. This evidences that absorption and desorption occurs in our PMMA

---

[4]Ref. [61] states that the recipe is index and density matched with PMMA. However, we find that a 3 mm PMMA sphere settles settles 47 mm in 526 seconds at $22°$C. The particles used in Ref. [61] were about 0.1 mm in diameter, so most likely made with a different process, and therefore probably had a slightly different density.

[5]The viscosity of a Triton-water mixture for 10% water is more viscous than pure Triton itself, by at least 10%.

[6]In Ref. [63] it was observed that n_D could change by 0.0025 by letting a PMMA film dry in vacuum. This change was attributed to solvents degassing under vacuum, stated as follows in Ref. [63]: *"Any variations of the residual water content and solvents in the polymer material can induce an index change [...]"*.

particles; these processes most likely develop stresses in the PMMA[7].

Zinc Chloride -- Zinc chloride is added to improve the miscibility of water and Triton, and to change the density of the fluid. Zinc chloride however seems to precipitate out of the mixture[8]. Using less zinc chloride ensures that less will precipitate. Note that in Ref. [62] it was mentioned that adding HCl to the fluid diminishes the formation of this precipitate; we have confirmed that this is indeed the case: the turbidity of the mixture disappeared completely after adding 2 ml of a 37 % HCl solution to 1.5 liter of the Triton mixture.

A new protocol -- The considerations outlined above have led us to develop a new protocol to achieve index matching. This protocol is stated below. Note that we did not use the HCl to prevent the formation of precipitate; we use such small quantities of $ZnCl_2$ that this is not necessary. The protocol does not use a fixed amount of water/$ZnCl_2$, but instead adapts this amount to achieve best index matching:

1 Soak the particles in pure Triton for a few days.

2 Premix water and zinc chloride; we found 10 grams of zinc chloride per 100 ml of water to be sufficient.

3 Remove the particles from the Triton they were soaking in, and add the particles in the measurement system. Do not wash all Triton from the particles at this step.

4 Add enough pure Triton in the measurement system to submerse the particles -- make a layer of 1 cm of pure Triton above the surface of the suspension. This layer is to ensure when the granular suspension expands due to shear, it will not experience the surface tension of the fluid layer above it.

5 Add small amounts (0.1% of the total liquid volume in the box) of the H_2O/$ZnCl_2$-mix repeatedly until index matching is achieved. Below we describe a way to determine this.

6 Once the PMMA particles have been in contact with the Triton based fluid, store them submersed in pure Triton to prevent drying of the particles.

---

[7]Although according to the manufacturer, PMMA is supposed to absorb only 0.3% of its volume on water per day, and therefore even less for a far larger molecule like Triton X-100.

[8]Although the water/zinc chloride mix is not saturated: water can dissolve about 400 gram of zinc chloride per liter.

Note that the density and viscosity of this mixture have to be measured separately, since they are not a priori known. This recipe can therefore not be used to achieve density matching.

Achieving index matching -- Step 5, the index matching step, is best done inside the measurement system itself, using the laser light that is to be used also for illumination. The index of refraction depends both on the temperature and the wavelength of the light. Refractometers typically use the D lines of sodium (589 nm) in the determination of the index of refraction, and if the laser light used in the experiment is not of the same wavelength, good index matching based on the n_D values might prove to be insufficient in the experimental setup.

An effective way to check for index matching is to see whether one can read a text printed in a large font through the suspension inside the 15 cm wide box. We have found the readability of such a text to be a sufficient criterion for achieving images that are good enough for at PIV techniques.

Index of refraction -- The index of refraction of most materials show modest temperature dependence. Generally speaking, the refractive index of liquids and solids goes down with temperature. Typical temperature coefficients are in the range of 0.0001-0.0005 K^{-1} [64, 65].

Laser dye -- The dye we use is Nile Blue 690. The dye is available in the form of small crystals, which do not dissolve easily in either Triton or water. Therefore, we dissolve 1 mg of Nile Blue 690 crystals in 1 liter of ethanol, in which the dye dissolves easily. One milliliter of the ethanol-dye solution is added to every 100 ml of index matching fluid. The ethanol affects the index of refraction of the fluid, but this effect is limited, due to the small amounts of ethanol added. Moreover, the ethanol evaporates from the index matched fluid. Naturally, the more dye one adds to the index matched suspension, the larger the contrast one can get in the images. However, the dye also absorbs the light, and the more dye is added, the less light is available for imaging deeper inside the bulk of the suspension. See Fig. 3.2 for an illustration of a high dye concentration (a), and a low dye concentration (b) fluorescence gradient. The precise quantity of dye that is to be added therefore depends on how many particle layers one wants to or can image, the desired location within the suspension where one wants to image, and the imaging rate.

Nile Blue spectrum -- Nile Blue 690 perchlorate has a different absorption and emission spectrum, depending on the liquid it is dissolved in [66]. We observed that *pure* Triton with Nile Blue added to it becomes pink. Adding small

amounts of water gradually shifts the color from pink to dark blue, which is the color Nile Blue obtains when dissolved in ethanol. This implies that one always has to add a certain amount of water to the Triton in order to tune the spectrum of the dye. For Triton-based index matching fluids, the amount of water necessary to achieve index matching is usually also enough to make the spectrum of Nile Blue 690 compatible with the laser light used in our experiments. In combination with other index matching liquids, this amount of water is not necessary: in section 4.4.1 we will describe a dimethyl-sulfoxide (DMSO) based index matching liquid, in which the amount of water necessary to achieve index matching is not sufficient to change the spectrum of Nile Blue 690 enough. In that index matching liquid, we therefore use another fluorescent dye. Note that adding milliliter quantities of an HCl solution to Triton is also sufficient to shift the spectrum of Nile Blue to the desired wavelength; this effect can also be used with DMSO, to avoid the necessity of changing the dye.

Photobleaching -- The laser dye loses its ability to fluoresce over the course of weeks. This process is called bleaching, and is enhanced under the influence of light (photobleaching). Therefore, it is advisable to protect the dye in the fluid or in storage from light at all times. The laser used in the experiments can actually be triggered, such that it is only on during the exposure time of the CCD. Using this feature ensures that the laser beam is not bleaching the dye unnecessarily. Under standard laboratory lighting conditions, a prepared batch of index matched fluid with the dye added was found to lose its blue color, which presumably is the sign of photobleaching, over the course of 2-3 weeks. This makes photobleaching seem to be not such an important issue. Yet, since the optimal contrast and gradients in the acquired images depend exponentially on the dye concentration, it is still recommended to avoid this whenever possible.

3.3   Comparison to Dry flows

We verify experimentally that the split-bottom suspension flows at slow driving indeed correspond very well with flow profiles measured for dry flows in the same geometry. To do this, we measure the flow profiles of 4.6 mm PMMA particles suspended in an index matched Triton-based fluid, based on the recipe from Ref. [61]. We measure the flow profiles at a rotation rate of the disk Ω of 8.3×10^{-5}. We perform all the experiments in setup M described above.

We measure these profiles for different filling heights H: 22, 32 and 45 mm. We will refer to these filling heights as *low*, *medium* and *high* respectively. The
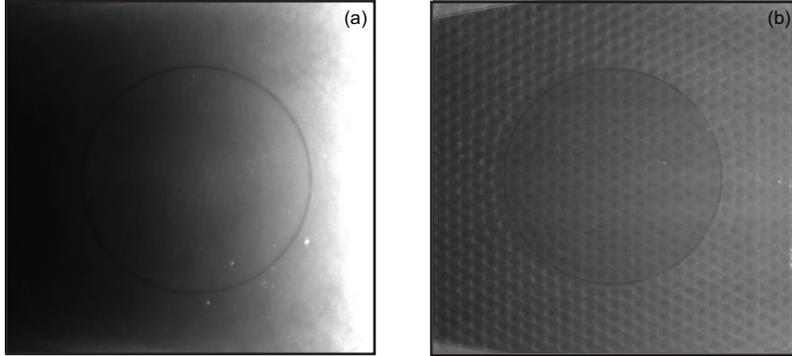
Figure 3.2: Top views of a cross section of the split-bottom box. The laser sheet shines from the right and intersects a layer in which only the dyed fluid is present, above the suspension. (a) An image in which the gradient in the fluorescence is clearly visible. (b) Using a smaller dye concentration, the contrast is decreased, and even deep in the box, far to the left, fluorescence is still observed.

radius of the disk R_s is 45 mm. H/R_s is then: 0.5, 0.7 and 1.0, all ± 0.05. From the estimate that the measured filling height H has an error bar of $\delta H \pm d/2$, we it follows that $\delta H/R_s \pm 0.05$.

We image the flow in several horizontal slices at position $z < H$. The imaging positions are as follows: for the low filling height, $z = 3, 7, 10, 13, 17$ mm. For medium, we use $z = 3, 9, 15, 21, 27$ mm, and for the largest filling height we use $z = 4.5, 9.5, 14.5, 19.5, 24.5, 29.5, 34.5$ mm. For all positions z, the error bar is ± 1.5 mm from the uncertainty in determining where the rough bottom starts.

We use PIV methods to extract the velocity profile; see appendix 8.1 for details. For each imaging position we acquire 1000 frames, with an interframe time of 40 seconds. Total measurement time is then 11 hours. At Ω of 8.3×10^{-5} rps, this interframe time limits the maximum displacement per image pair approximately 5 pixels. This is less than the ideal strain mentioned in appendix 8.1, so in the PIV we use n=10. For small r, we cannot reliably obtain $v(r)$; we place the cutoff at $r \sim 18$ mm. The profile is smoothed by subdividing the r-coordinate range into 20 bins of $\sim d/2$, with d the particle diameter, and averaging the values for $\omega(r, z)$ in those bins.

55
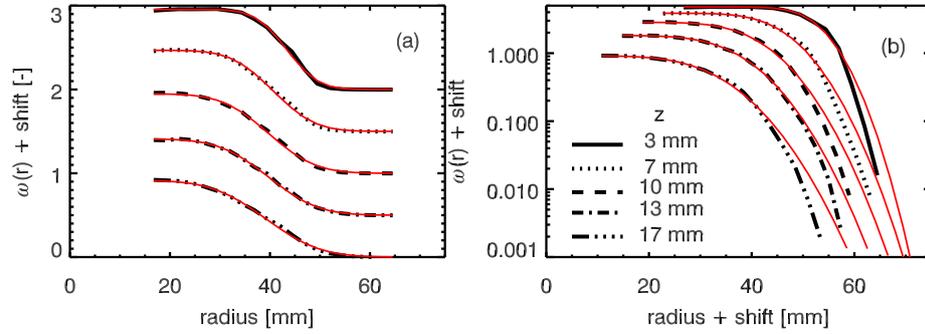
Figure 3.3: Normalized angular velocity profiles $\omega(r) = v(r)/2\pi r\Omega$ for the $H/R_s = 0.5$ suspension flow, for $\Omega = 8.3 \times 10^{-5}$ rps. (a) Shows the data on linear scale, with all the curves shifted upwards for clarity, (b) shows the same data on logarithmic scale -- here the curves are shifted horizontally as well as vertically. The range on the abscissa corresponds to the width of the cell. The line style indicates the imaging position z, given in the legend, and the solid red line is an error function fit.

3.3.1   Qualitative Comparison: Low Filling Height

In Fig. 3.3 we plot the individual profiles measured for the low filling height, $H/R_s = 0.5$. For all imaging positions z we see that the $\omega(r, z)$ data qualitatively resemble an error function. This is evidenced by the red line in Fig. 3.3, which is an error function fit. This is the same function Eq. 1.3 as used to fit dry granular flow profiles in the split-bottom geometry; we reproduce this equation here:

$$\omega(r, z) = \frac{1}{2} - \frac{1}{2} erf\left\{\frac{R_c(z) - r}{W(z)}\right\}.$$

This suggests that the suspension flow behaves as a dry granular flow at this flow rate. Also, the trends in the smaller details of the angular velocity profiles for increasing imaging position z give more evidence for dry granular flow behavior in the suspension. We some trends that are very similar to what is observed in dry granular flows: the point $R_c(z)$, the center of the shearband where $\omega(r, z) = 0.5$, moves inwards for increasing z. The error functions also clearly broaden with z. This same behavior is also found for dry flows, see Eq.1.8:

$$z = H - R_c(z) \left[1 - R_c(z)/R_s(1 - H/R_s)^{2.5} \right]^{1/2.5},$$

and Eq. 1.5 respectively:

$$W(z) = W(z = H)\sqrt{1 - (1 - z/H)^2}.$$

In Fig. 3.4a the individual normalized angular velocity profiles from Fig. 3.3 are combined and plotted as a contour plot. $\omega(r, z)$ here is interpolated and color-graded in the two dimensional vertical cross section (r, z); red means $\omega = 1$, so there the material co-rotates with the driving disk. Blue/black shows that no motion is present in that region. In the white areas, flow is also absent. The trends observable in Fig. 3.3, such as the widening of the shear zone and the inward movement of the center of the shear band, are now clearly observable. It is also obvious that the 'trumpet' - shaped part of the suspension just above the disk is co-moving with the rotating disk; the angular velocity in the region $r < 30$ mm is clearly very close to one.

To compare the contour plot of the suspension flow, we create the same contour plot for what a dry granular flow would have been in the split-bottom flow cell with the same dimensions. We use the equations from Chapter 1, that were reiterated above. These empirical equations have only one fit parameter: $W(z = H)$. W encodes for the fact that particles with a different roughness, aspect ratio or diameter create different overall widths of the shear bands. We determined the best fit for $W(z = H) = 14$, by overlaying contour plots of the suspension flow data $\omega_S(r, z)$ and the predictions based on the equations $\omega_D(r, z)$. This best fit is shown in Fig. 3.4b. The contour plot in Fig. 3.4b is remarkably similar to the plot in (a), even though only one fit parameter was used to match the two profiles, instead of three per individual profile. This gives further evidence for the similarity of suspension flow profiles to dry flows.

3.3.2   Quantitative Comparison: Low Filling Height

The strictest, quantitative test we can apply to compare the suspension flow profiles to the dry flow profiles is the following. We make a scatter plot of $\omega_S(r, z)$, the set of angular velocities measured in the suspensions at different locations in the cell, as a function of $\omega_D(r, z)$, the set of the angular velocities at those same locations, extracted from the empirically obtained dry granular flow profiles. This plotting is shown in Fig. 3.4c on a linear scale and in (d) on a logarithmic scale. If all data points were on the straight line, it would indicate that the two profiles are identical. Even in this strict quantitative test, it is clear the the flow profile for the suspension at $\Omega = 8.3 \times 10^{-5}$ rps matches almost perfectly with
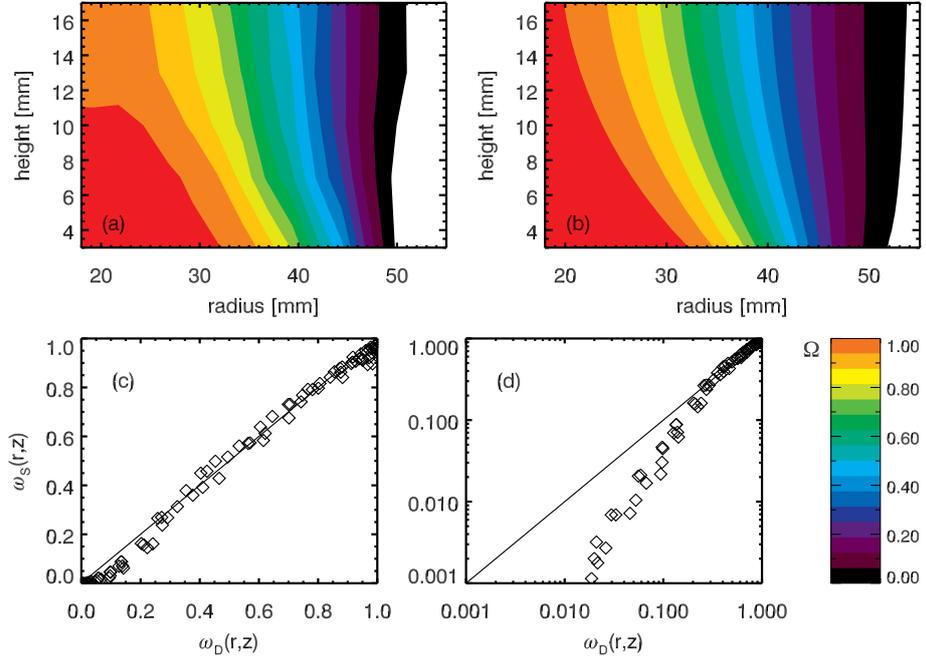
Figure 3.4: The normalized angular velocity profile measured at $\Omega = 8.3 \times 10^{-5}$ (a), and the empirical dry granular flow profiles (b, see text for explanation). In (c) all $\omega_S(r, z)$ values measured in the suspension flow are plotted against the expected $\omega_D(r, z)$ at that location. (d) Shows the same data as (c), but on double logarithmic scale. The straight line would indicate a perfect agreement between the profiles in (a) and (b).

the dry granular flow profiles. The deviations visible in Fig. 3.4d are most likely attributable to systematic experimental inaccuracies.

We also used this scatter plot to optimize the fitting parameter $W(z = H)$. By reducing $W(z = H)$ from 14 to 13, we observe that the tail of the logarithmic plot improves its linearity substantially, whereas the scattered data on the linear plot Fig. 3.4(c) then starts to deviate more from the ideal straight line, especially for $\omega_D(r, z) \sim 1$. For $W(z = H) = 15$, this trend is reversed: linearity on the linear plot is improved, but curvature in the scatter plot on the logarithmic scale is increased. These trends also show that $W(z = H) = 14$ is the best fitting parameter, with which we can get excellent agreement between the established dry granular flow profiles and the measured suspension flow structure.
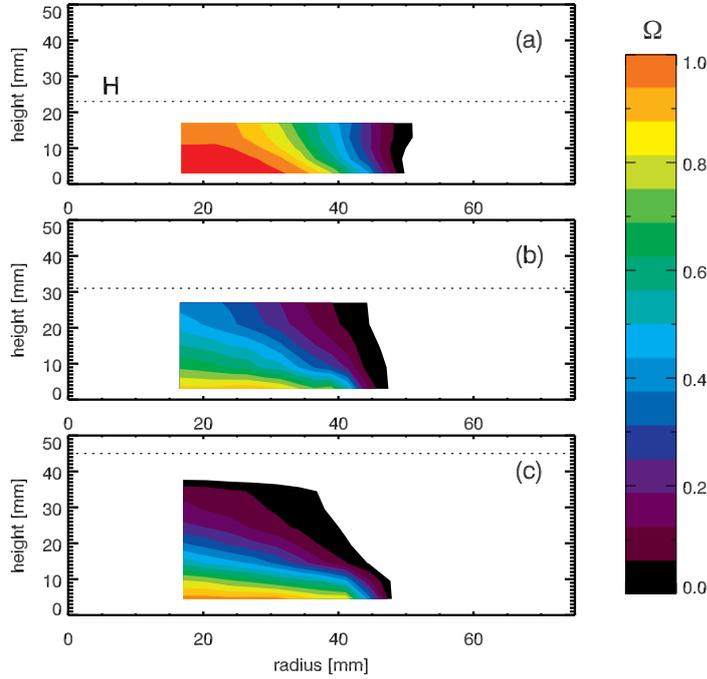
Figure 3.5: Contour plots for the $\Omega = 8.3 \times 10^{-5}$ rps flows measured in the suspension. (a) to (c) show the angular velocity profiles $\omega(r, z)$ for three different filling heights: $H/R_s = 0.5$, 0.7 and 1.0. The color indicates the normalized angular velocity. The dashed line shows where the surface at height H is.

3.3.3   Comparison for Different Filling Heights

To further test the similarity between the suspension flow profiles and the dry granular flow profiles, we can also see whether the trends observed in dry flows in which the filling height was increased, are visible for the suspensions.

For dry flows in the split-bottom geometry, the flow field depends strongly on the filling height H/R_s. This phenomenology is described in section 1.4.4, we will briefly mention it again here: in the dry flows, for low filling heights with $H/R_s \lesssim 0.6$ there is a 'trumpet'-shaped shear zone propagating through the granular medium from the edge of the disk to the surface of the granular bed; for large filling heights $H/R_s \gtrsim 0.7$ the shear zone is entirely confined to the bulk, in a 'dome'-like structure.

We measure the normalized angular velocity $\omega(r, z) \equiv v_\theta(r, z)/r\Omega$ for $\Omega =$

8.3×10^{-5} rps, for the three filling heights low, medium and high. In the flow profiles of the slowly driven suspension, we can see a trend that is strikingly similar to the behavior observed in dry flows: the contour plots of the flow profiles for the suspensions with the low, medium and large filling height are shown in Fig. 3.5(a), (b) and (c) respectively. Indeed, the shearband, evidently propagating to the surface in (a), is confined to the bulk in (c). Fig. 3.5(b) shows a transitional regime also described in section 1.4.4. This shows that the slowly driven suspension flows in the split-bottom geometry are also very similar to dry granular flows for large H/R_s.

A quantitative comparison between the dry flow profiles and the suspension flow profiles is not possible, since for $H/R_s > 0.6$, no complete empirical description of the dry granular flows is available. The axial slip profile $\omega(r = 0, z)$ measured by Cheng [34] cannot be checked for consistency with the suspension flow data, since we cannot reliably measure $\omega(H)$ close to the center $r = 0$ of the cell.

3.4   Beyond Slow Flows

For increased driving rates, viscous drag forces will start to play a role in the dynamics of the particle. In this section we will show that this has a profound effect on the velocity profiles of suspensions in the split-bottom geometry -- by increasing the driving rate by three orders of magnitude, we go from the rate independent flow regime to the rate dependent regime.

We apply the inertial number theory described for dry flows in section 1.5.1 to our suspension flow in this faster flow regime. This theory will explain the observed change in the flow profile as follows. We will show that the stresses in suspension flows in the rate dependent regime are predicted to be dominated by a term $\sim \dot{\gamma}$, which makes the suspension Newtonian in this limit. We verify this prediction by numerically calculating the flow profiles for a Newtonian fluid in the split-bottom geometry. The Newtonian flow profiles are indeed strikingly similar to the profiles observed in the suspension.

3.4.1   Measured Flow Profiles

We measure the flow profiles of the PMMA-Triton suspension for three values of $\Omega = 8.3 \times 10^{-4}, 8.3 \times 10^{-3}$ and 8.3×10^{-2} rps, for the low, medium and large filling height. For the low filling height, we show the three velocity profiles measured at these Ω in Fig. 3.6b-d. We also include the velocity profile measured in the slow flow limit, at $\Omega = 8.3 \times 10^{-5}$ rps in Fig. 3.6a. The change in the flow profiles
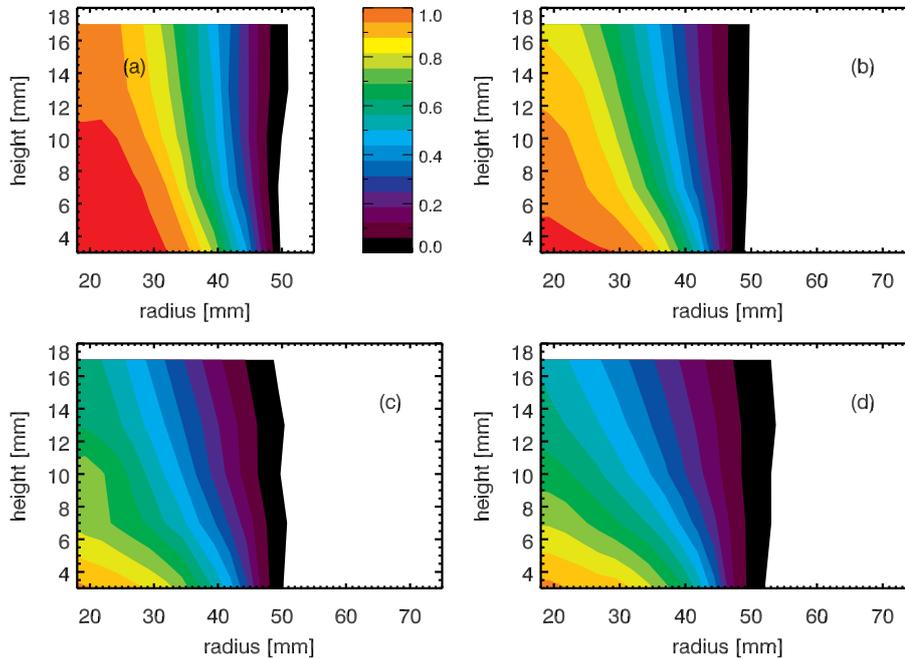
Figure 3.6: Contour plots for the normalized angular velocities for $H/R_s = 0.5$ (a) Through (d) show data for $\Omega = 8.3 \times 10^{-5}$, 8.3×10^{-4}, 8.3×10^{-3} and 8.3×10^{-2} rps. Color code is identical to color code in Fig. 3.5.

is striking: the solid-like core that co-rotates with the disk at $\Omega = 8.3 \times 10^{-5}$ rps vanishes completely with increasing driving rate -- the shearbands broaden substantially with Ω.

Slip -- At the largest Ω, the normalized angular velocity profile does not reach 1 anywhere in the suspension, not even close to the bottom. This suggests slip is present. At this $\Omega = 8.3 \times 10^{-2}$ rps, we push the imaging capacities of the IMS system to its limits: motion blur is clearly visible in the images, so the presence of some imaging artifacts cannot be ruled out. However, since the flow profiles are still smooth some slip is certainly present.

For $\Omega = 8.3 \times 10^{-2}$ rps, we show contour plots of the flow profiles for the three different filling heights used in Fig. 3.7. The broadening of the shearzone with increased Ω is also apparent for $H/R_s = 0.5$ and 0.7, although it is less evident for these filling heights. Slip is present to the same extent for all filling heights.
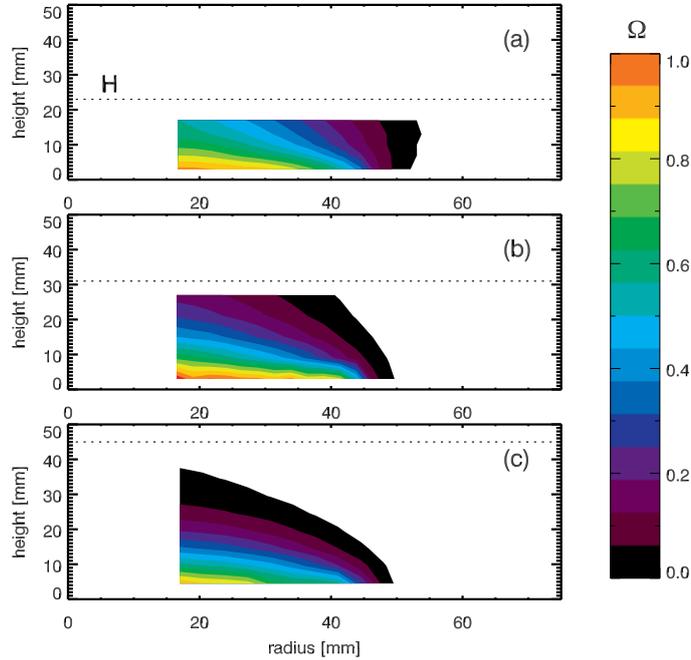
Figure 3.7: Contour plots for the $\Omega = 8.3 \times 10^{-2}$ rps flows measured in the suspension. (a) to (c) show the angular velocity profiles $\omega(r, z)$ for three different filling heights: H/R_s = 0.5, 0.7 and 1.0. The dashed line shows where the surface at height H is.

3.4.2 Theory: Rearrangement Timescales

We want to establish a mapping between the inertial number theory described in section 1.5.1, established for dry flows, and the submersed flows we study here. Such a mapping will give insight on how the rheology of the suspension depends on the driving rate. This in turn will tell us more about the rate dependence of the structure of the flows. We will show that the theory gives a reasonable bound for which Ω the rate independent regime should end. Moreover, we will show that in the rate dependent regime, the theory gives remarkably accurate predictions for the structure of the flow of gravitational suspensions.

In the inertial number theory the behavior of dry granular flows is described with the so-called inertial number. As detailed in section 1.5.1, the inertial number is the dimensionless product of the shearrate and the typical rearrangement timescale of a particle. For dry flows, the rearrangement timescale of a particle is

simply $d/\sqrt{P/\rho_p}$. For suspension flows, the viscosity of the interstitial fluid plays a role in the rearrangement process of the particle, and hence the particulate rearrangement timescale in suspensions will be different.

To estimate the relevant timescales in the dynamics of the particles in the suspension at these driving rates, it is necessary to write down an approximation for their equation of motion. In this analysis, we follow Courrech du Pont *et al.* and Cassar *et al.* [60, 67].

The equation of motion for a particle in a fluid can be stated as follows:

$$\frac{\pi}{6}\rho_f d^3 \frac{dv_p}{dt} = \frac{\pi}{4}Pd^2 - F_d,$$ (3.1)

Here ρ_p is the bulk density of the material the particle is made of, d their diameter, v_p their velocity, P is the confining pressure due to the presence of other particles, and F_d the drag force experienced by the particle.

For a particle moving in a fluid, the drag force can have a different functional dependence on the velocity of the particle, depending on the particulate Reynolds number. This dimensionless number is the ratio between inertial and viscous forces acting on a particle:

$$Re = \frac{\rho v_p d}{\eta_f}$$ (3.2)

For $Re \ll 1$, the particle experiences viscous or Stokes drag: $F_d \sim v_p$. For $Re \gg 1$ the particle experiences inertial drag forces: $F_d \sim v^2$. We can estimate the Reynolds number by assuming that $v_p \leq 2\pi\Omega R_s$. We then find that even for the largest rotation rates possible in our system, 8.3×10^{-2} rps, that $Re \leq 1$. Therefore we can assume the drag forces on the PMMA particles in our Triton suspension are purely viscous.

The proportionality factor in the relation $F_d \sim v_p$ can be estimated as follows: the movement of a grain inside a packing requires the displacement of an equal volume of liquid. The resistance that this liquid experiences by having to flow through the packed bed is equal to the drag force on the particle. So if we know the resistance the fluid experiences, we also know the drag force on the particle. We calculate the resistance as follows. The pressure difference required for a fluid to flow through a medium of porosity $k = ad^2$ with velocity v_p is given by Darcy's law [68]:

$$\Delta P_{fluid} = \frac{-v_p L \eta_f}{sk},$$ (3.3)

Here L is the length over which the pressure gradient exists - in this case the volume inside the packing in which the particle moves. Using $L = d$, we arrive at

the resulting drag force on the particle:

$$F_d = \frac{\pi}{4}d^2 \Delta P_{fluid} = \frac{v_p d\eta_f}{-a},$$ (3.4)

The parameter a is given by the Carman-Kozeny equation[9], and depends on the size distribution of the particles, their shape and also on the density of the granular bed [70][10].

$$a = \frac{\varPhi_S^2 \epsilon^3}{150(1 - \epsilon)^2},$$ (3.5)

with ϵ the porosity, equivalent to $1 - \varPhi$ where $\varPhi$ is the packing fraction. $\varPhi_S^2$ is the sphericity [70] of the particles, which equals 1 for spheres. For our suspensions, we assume $\varPhi = 0.59$, the typical value of a settled granular bed. This gives $a = 0.001$.

   With the equation of motion for our particles, we can now estimate the rearrangement timescale for a particle in the fluid. With this estimate of the rearrangement timescale for particles in a fluid, we can recalculate the inertial number for these flows, and then apply the inertial number framework from dry flows to suspension flows.

   In a static packing the hydrostatic pressure on a single particle is balanced. Due to rearrangements, this balance may disappear. The particle will then accelerate when it has space to do so. We assume that when the balance disappears, the confining pressure from the mass of the particles above the moving particle will act on it as force $P_g d^2$. When the particle accelerates, it will start to experience a drag force. The limiting velocity v_{inf} at which the accelerating force is equal to the viscous force is then

$$v_{inf} = P_g a d/\eta_f$$ (3.6)

The particle will reach this velocity in a characteristic time t_a:

$$t_a = \frac{2\rho_p a d^2}{3\eta_f}$$ (3.7)

---

[9]The Carman-Kozeny (see e.g. Ref [69] and references therein) equation is an extension of Darcy's law and gives a prediction for the proportionality constant in Darcy's law. The Carman-Kozeny equation in its turn is the low Re limit of the Ergun equation, the more general equation for the pressure drop in flow across a porous medium. The Ergun equation also accounts for inertial dissipation in the fluid, that occurs at higher Re. Since we work at low Re, the full Ergun equation does not have to be used here.

[10]Note that this only applies to homogeneous porous media; for heterogeneous media the determination of the prefactor is more involved; see e.g. Ref. [71].

For our suspension, $t_a < 1$ ms. Comparing this to the shearrate, which even for our fastest driving rates is maximally $\sim 2\pi\Omega R_s/H \sim 2\pi\Omega$, we can assume that during the complete rearrangement process, the particle travels with v_{inf}. Therefore the typical rearrangement timescale for the particles in the suspension becomes $d/v_{\mathrm{inf}} = \eta_f/P_g a$. With this the inertial number for suspension flows becomes

$$I_S = \frac{\dot{\gamma}\eta_f}{P_g a} \tag{3.8}$$

3.4.3   Theory: An Upper Bound for Slow Flows

With the inertial number scalings presented, we first want to establish where the theory predicts that the rate independent regime crosses over into a rate dependent regime -- this we can readily check with the data presented in section 3.4

For $I_S \ll 0.01$, submersed granular flows should behave as dry granular flows [23]. Estimating that in the split-bottom geometry, $\dot{\gamma} \sim 2\pi\Omega R_s/H$, and given that $H \sim R_s$, I_S gives an estimate for which rotation rates we do not expect viscous interactions to be important:

$$\frac{2\pi\eta_f\Omega}{a\Delta\rho g R_s} \ll 1 \rightarrow \frac{a\Delta\rho g R_s}{2\pi\eta_f} \gg \Omega \tag{3.9}$$

For the PMMA/Triton suspension, $I_S = 0.01$ at $\Omega \sim 0.002$. We estimate that that for driving rates less than about $10^{-3} - 10^{-4}$ rotations per second, a rate independent regime should be observed. The approximations made above and the uncertainty in η_f and $\Delta\rho$ mean that we cannot precisely determine where fluid drag becomes negligible. However, it is already clear that the inertial number scaling gives the right estimate for the order of magnitude where rate dependence should start to be observed. This is apparent in Fig. 3.6.

3.4.4   Theory: Prediction for Faster Flows

Knowing the inertial number for suspension flows, we also can try to use the inertial number theory established for dry flows [2] in suspensions. We write for the stress τ:

$$\tau = \mu(I)P, \tag{3.10}$$

with $\mu(I)$ the an empirical function. For low inertial numbers, $\mu(I)$ can be approximated by $\mu(I) = \mu_0 + \mu_1 I$ (Ref. [60], Fig. 13), with μ_0 and μ_1 empirical values,

as was also done in Ref. [23]. Using this $\mu(I)$ in Eq.3.10 together with Eq. 3.8, we arrive at:

$$\tau = \mu_0 P + \mu_1 \frac{\eta_f \dot{\gamma}}{a} \qquad (3.11)$$

In other words: the local stress in a suspension is a linear combination of a frictional stress and a purely viscous stress. This also means that if we increase the driving rate Ω in the split-bottom cell, we should see less and less of the frictional nature of the interactions between the particles in the suspension.

Consequences for the flow -- For large driving rates and small pressures, the stress τ in Eq. 3.11 will essentially be given by $\tau = \mu_1 \frac{\eta_f \dot{\gamma}}{a}$: the suspension should become Newtonian, with an effective viscosity $\mu_1 \eta_f / a$. Indeed, in the high rotation rate limit, the rheological data that we will discuss in the next chapter, indicates that the behavior of the suspension becomes approximately Newtonian. To verify that we are in a regime where the inertial theory becomes applicable, we calculate the spatial distribution of the inertial number $I(r, z)$ for the flow profiles measured in the suspensions. For each flow profiles measured at a different Ω, we then obtain a set of inertial numbers found in that flow profile. These sets for different Ω are plotted against Ω in Fig. 3.8.

Newtonian Flows -- For Newtonian fluids, we can numerically predict what the flow profile should be in the split-bottom geometry. We can then compare the flow profiles of the suspension to numerical predictions of Newtonian flows in the split-bottom geometry.

We use a Finite Element Method (FEM) software package (COMSOL) to compute the stead state Navier-Stokes flow equations for a Newtonian incompressible fluid in the split-bottom geometry. We assume rotational symmetry to reduce the problem to a two-dimensional configuration; we use no-slip boundary conditions for the disk and the static bottom and the walls, a slip condition for the surface, and drive the flow with the condition $v_\theta = 2\pi\Omega r$ at the disk, where v_θ is the velocity in the azimuthal direction. For details regarding the COMSOL calculation, we refer to appendix 3.6.1.

We solve the Navier-Stokes equations for the three different filling heights for which we also measured the suspension flow profiles: $H/R_s = 0.5, 0.7, 1.0$. The results are shown in Fig. 3.9a-c. We observe that in the solutions, a change from trumpet-like shearbands to dome-like shearbands is also visible, when changing the filling height from low to high. However, the shearbands for the low filling height are broad; most notably, the solid like inner core, that for dry flows co-rotates with the disk, is absent in the Newtonian flow solution. Note
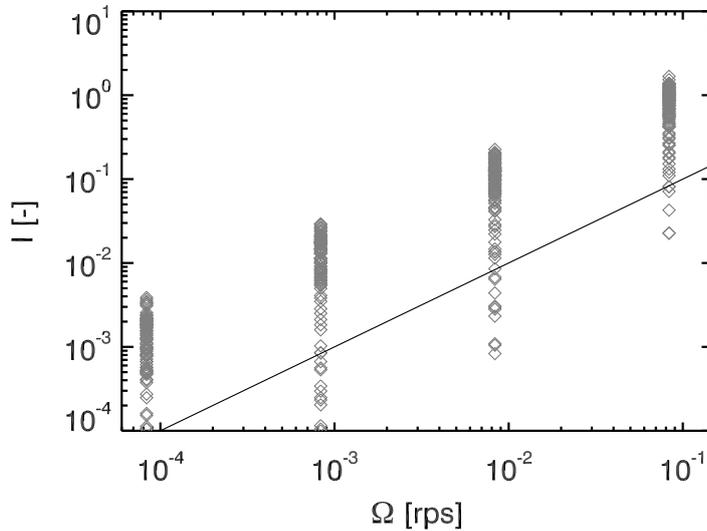
Figure 3.8: A scatter plot of the set of inertial numbers found for the flow profiles measured at four different Ω. The black line corresponds to $\Omega = I$.

that in the steady state Newtonian flow approximation, the rotation rate Ω only enters into $\omega(r, z)$ as a trivial prefactor as long as centrifugal forces are small. See Appendix 3.6A for a more detailed treatment of the influence of centrifugal forces on the flow profile of Newtonian flows in the split-bottom geometry.

3.4.5   Validation of the Inertial Number Theory

We can compare the Stokes flow prediction shown in Fig. 3.9 to the flow profiles measured at $\Omega = 8.3 \times 10^{-2}$ rps shown in Fig. 3.7. The qualitative similarity between the contour plots is strong. For both Newtonian and suspension velocity profiles, we see the same trends with increasing filling heights: consider the band for which $\omega = 0.5$, which is the light blue band. For the lowest filling height, this band still reaches the surface in the Newtonian flow profile, and the data shown for the suspension flows also strongly suggests that this band reaches the surface of the suspension, although at a slightly smaller r. For the larger filling heights, the $\omega = 0.5$ band is confined to the bulk. However, the suspension flows seem to be more confined to the bulk, than the Newtonian flow profiles. We can again also quantitatively compare the predictions for the Newtonian flow profiles with the suspension data in a scatter plot, as was done
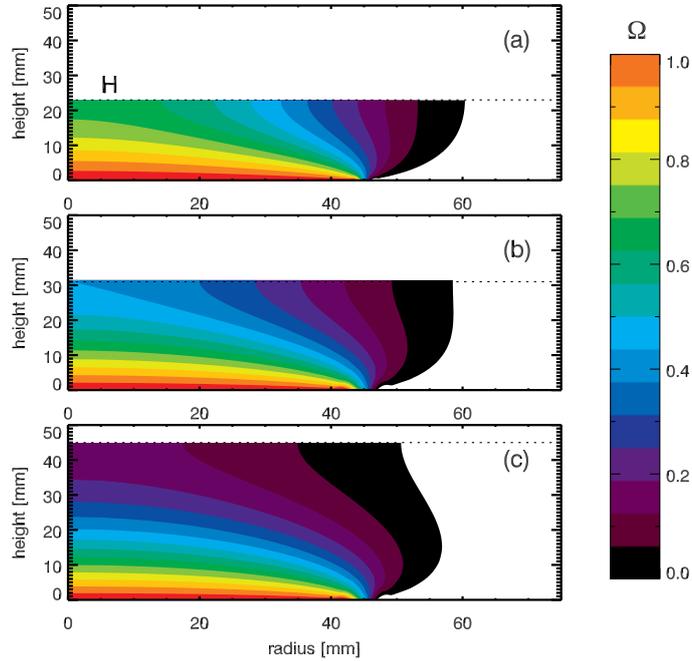
Figure 3.9: Stokes flow solutions for the split-bottom for three different filling heights. From (a) to (c): H/R_s = 0.5, 0.7 and 1.0. The contour plot shows the normalized angular velocity, Ω is arbitrary in this approximation, see text. The dashed line shows where the surface at height H is.

in section 3.3 when we compared the dry granular flow profiles to the slowly driven suspension flow profile.

In Fig. 3.10, we plot $\omega_S(r, z)$, the set of angular velocities measured for $\Omega = 8.3 \times 10^{-2}$ rps in the suspensions at different locations in the cell, as a function of $\omega_N(r, z)$, the set of the angular velocities at those same locations, extracted from the numerically calculated Newtonian flow profiles. We do this for the three different filling heights in Fig. 3.10a-c. Although the matching is quite good, especially for Fig. 3.10a, evidently the match is not as good as the match in Fig. 3.4. There are two possible effects that can cause this discrepancy. First of all there is 30% slip at the driving disk; the suspension flow profiles nowhere reach $\omega > 0.7$. This effect can be taken into account by comparing the data points to the line $\omega_S(r, z) = 0.7 \times \omega_N(r, z)$. This line is also plotted in Fig. 3.10a-c. Clearly the data lies closer to that line, but the finite curvature in
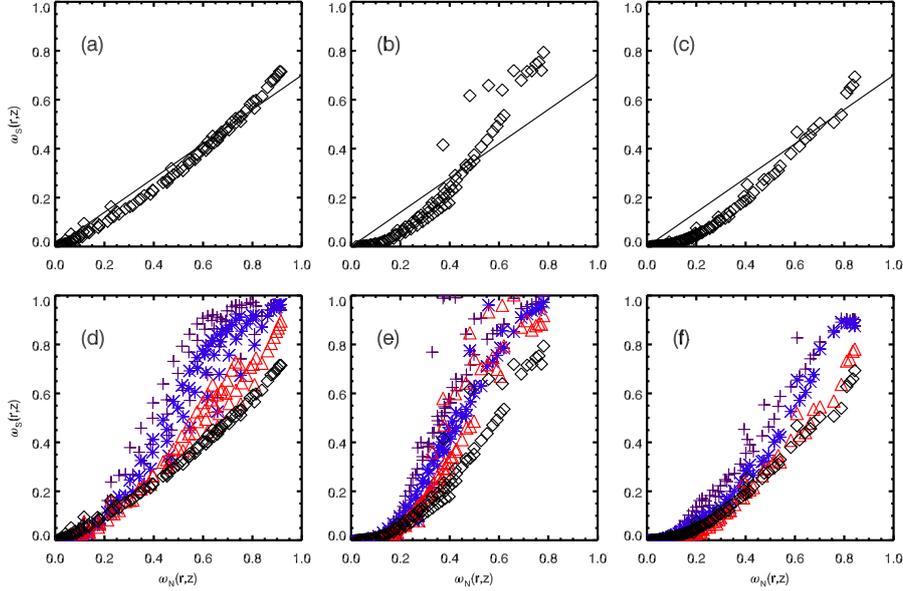
Figure 3.10: Comparison for three different filling heights of the Stokes flow solution to the velocity profiles found in the suspensions. H/R_s: (a),(d) = 0.5, (b),(e) = 0.7 and (c),(f) = 1.0. The upper row shows only the comparison between Newtonian and the $\Omega = 8.3 \times 10^{-2}$ rps suspension data. The line indicates equivalence between Newtonian and suspension flows, assuming a slip of 30 %. The lower row shows this comparison for all Ω. Different symbols and colors indicate different Ω; black $\diamond$ = 8.3×10^{-2} rps, red $\triangle$ = 8.3×10^{-3} rps, blue $*$ = 8.3×10^{-4} rps, and purple + = 8.3×10^{-5} rps.

the scatter plot, observed for all filling heights, cannot be explained by this. The second effect that has not been considered is the fact that the suspension rheology is not Newtonian throughout the whole flow. In regions in the flow where the local strain rate $\dot{\gamma}$ is small the local rheology given by Eq.3.11 might still be dominated by the frictional stresses $\mu_0 P$. In steady state flow, local stress balance has to hold. For small stresses of the order of $\mu_0 P$, and for the rheology of Eq. 3.11, this stress balance can be achieved locally with very small $\dot{\gamma}$ correction on the already present $\mu_0 P$ - term. A Newtonian rheology can only achieve stress balance by adjusting $\dot{\gamma}$, and is therefore inclined to have larger $\dot{\gamma}$ where the local stresses become of the order of $\mu_0 P$. The concave shape of the scattered data is

69

precisely an indication of this overestimation of $\dot{\gamma}$.

3.5   Conclusions
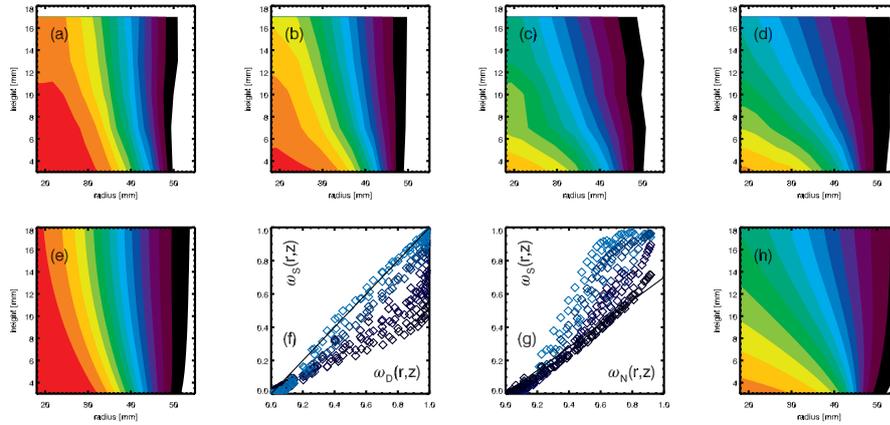
Figure 3.11: For $H/R_s = 0.5$: (a-d) The velocity profiles at driving rates $\Omega = 8.3 \times 10^{-5}$ rps (a) to $\Omega = 8.3 \times 10^{-2}$ rps (d), as in Fig. 3.3. In (e) the profile for dry granular flows; compare this to (a). In (f) the profile for Newtonian flow is plotted; compare this to (d). (f) has a scatter plot comparison between the dry flow profiles $\omega_D(r, z)$ and the measured suspension flow profile $\omega_S(r, z)$ for the driving rates shown in (a-d); darker blue is faster driving. (f) has a scatter plot comparison of $\omega_S(r, z)$ to the Newtonian profile $\omega_N(r, z)$.

In this chapter, we described the application of the IMS technique to split-bottom flows. We showed that there is an excellent quantitative agreement between the empirically established flow structure equations for dry split-bottom flows, and the measured flow fields for slowly driven suspensions -- see Fig. 3.11a-e. This means that for slow driving rates, suspension flows in the split-bottom geometry behave as dry granular fluids -- the interstitial fluid does not affect the flow field.

At increasingly larger driving rates, we observe a change in the flow profiles of the suspensions, as shown in Fig. 3.11a-d. We apply the inertial number

theory for suspensions to the regime of flow rates and find that the theory predicts Newtonian behavior for faster driving rates. Comparing the measured flow profiles to that of Newtonian flow in the split-bottom geometry as done in Fig.3.11d-f, we see that this inertial number theory captures the flow behavior of the suspensions in the fast driving rate limit very well.

3.6 Appendices

3.6.1 A: Details of the COMSOL Calculations
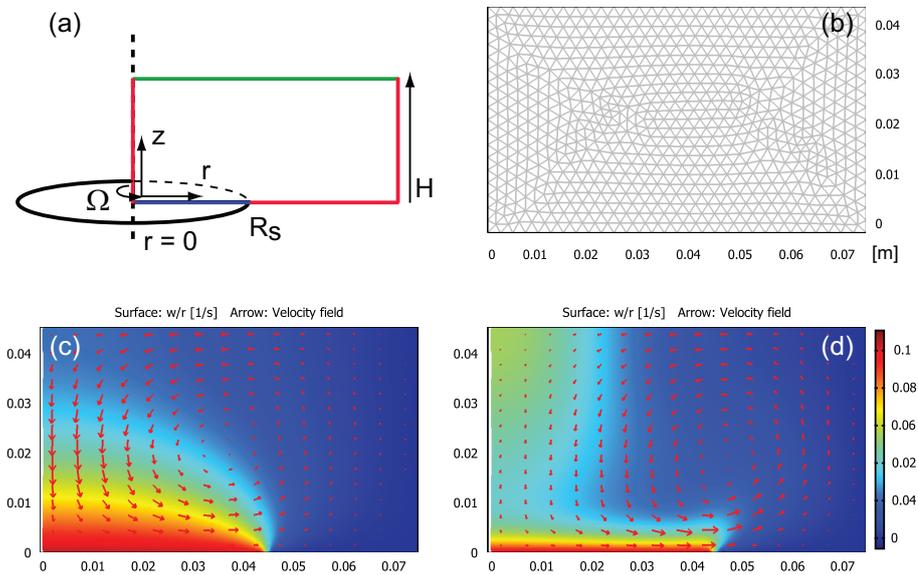
Figure 3.12: (a) The boundary conditions of a two dimensional cross section of the split-bottom cell. Red: no-slip boundary conditions. Green: slip. Blue: no-slip with the condition $v_\theta = 2\pi r\Omega$. R_s is equal to that of the setup used: 45 mm. (b) A typical mesh with nodes with which the flow equations are solved numerically. (c) The flow field for pure Triton at 1 rpm driving rate. The contour plot shows the angular velocity ω, the arrows indicate the magnitude of the local in-plane flow field v_r and v_z. (d) The flow field for water driven at 1 rpm. The lengths of the vectors for water are reduced by a factor 40. Units on abscissa and ordinates are all in [m].

[11]We used the Finite Element Package (FEM) COMSOL to solve the steady state Navier-Stokes equations [72] in the split-bottom geometry. In this section, we give the details of how the calculations were carried out. The rotational symmetry of the cell allowed us to reduce computation time by solving the equations on a two-dimensional cross section in the split-bottom geometry. This cross section is shown in Fig. 3.12. Solving the steady state Navier-Stokes equations for this geometry in three dimensions essentially gives the same results, but is more CPU and memory intensive [73].

Boundary conditions -- The boundaries are shown in Fig. 3.12. The surface is fixed and horizontal. We verified experimentally that the surface of the suspended particles is flat up to $\sim 1.5 \times 10^{-1}$ rps, so for the range of rotation rates encountered in this section, the flat surface assumption is appropriate. The disk, the outer wall and static part of the bottom are treated as no-slip boundaries. The disk has the velocity condition $v_\theta = 2\pi r\Omega$, where r is the radial coordinate.

Centrifugal forces -- In the split-bottoms geometry, centrifugal forces set up a secondary flow in the fluid. This can be shown easily with the FEM calculations. The magnitude of this secondary flow, however, depends on the rotation rate and the viscosity of the fluid. This can be seen in Fig. 3.12c-d. Flow fields for both Triton and water are shown as contour plots. Also, the in-plane velocity fields are plotted as vectors. The magnitude of the vector in the x-direction is given by v_x, the magnitude of the local velocity component in the x direction. Mutatis mutandis for the component in the z-direction, we obtain an indicator for the secondary flow profile, set up by the centrifugal force. Note that the vectors in the plots for both Triton and water are rescaled to have similar length. The maximum in-plane flow velocity for Triton is 1.9×10^{-5} m/s, for water this is 7.7×10^{-4} m/s, whereas the driving rate is 0.1 m/s. We conclude that for Triton, with a viscosity of 0.2 Pa·s, the secondary flow strength in the range of rotation rates reported in this chapter is not significant. So in the limit of $\Omega \to 0$, all the flow profiles are as in Fig. 3.12c. However, for low viscosity liquids such as water, with a viscosity of 1 mPa·s, at 8.3×10^{-2} rps, a significant secondary flow develops at the highest rotation rate seen in the suspension experiments.

Strain rate above split -- In the COMSOL calculations, there is an infinite strain rate precisely at the location of the gap. We verify here that this divergence does not affect the flow field predictions for Triton. We compare a

---

[11]Many thanks to support engineer Anders Ekeroth from COMSOL for help with the software package.
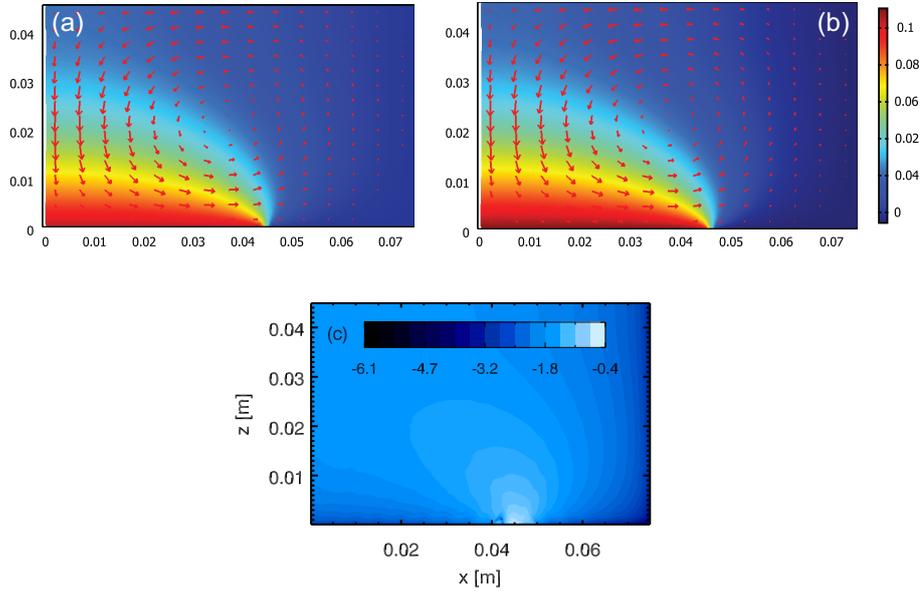
Figure 3.13: (a) The flow field calculated without the slip region next to the disk. (b) The flow field with the slip region included. (c) The absolute difference between (a) and (b), normalized with the rotation rate and on logarithmic scale. Units on abscissa and ordinates are all in [m].

rate independent flow profile for $H/R_s = 1$, shown in Fig. 3.13a, to a flow profile calculated with slightly different boundary conditions: we add a 2 mm wide gap with a slip boundary condition next to the rotating disk. This slip region represents the small gap between the rotating disk and the static bottom. Note that 2 mm is a strong overestimation of the size of the gap; in actual experiments the gap is never larger than 1 mm. The flow profile predicted for this geometry is shown in Fig. 3.13b. The difference between the two flow profiles in that figure is very small and only notable near the disk edge region. In Fig. 3.13c, we plot the logarithm of this difference, normalized by $v_\theta(R_s) = 2\pi R_s \Omega$. It is obvious that in the numerics, removing the divergent strain rate near the edge by adding a slip region is not necessary -- it does not affect the results appreciably.

3.6.2 B: IMS and Other Visualization Techniques

There are more experimental techniques to study granular flows in three dimensions. Each has its own advantages; to highlight under which circumstances

the IMS technique is beneficial, we briefly describe the other techniques, their typical use, and advantages and disadvantages in this appendix.

The IMS approach is a relatively young technique, and has so far only been applied to silo flows [74] and flows in plane shear [18], albeit only in preliminary form. The first study in which the benefit of IMS has been used to its full extent, is in the analysis of the static three dimensional structure of granular packings exposed to thermally induced expansion and contraction cycles [58].

The index matching scanning technique offers some benefits over other methods to study granular materials in three dimensions. The most common other techniques are X-ray tomography, Magnetic Resonance Imaging (MRI), and confocal imaging; we give a short overview of the existing techniques.

MRI techniques have been used to study flow profiles and density profiles inside sheared granulates [34, 40, 75]. MRI techniques have a submillimeter accuracy in macroscopic volumes, but only at a slow scanning rate. They are very sensitive to density differences, but can only track small numbers of tracer particles, and are limited to tracking materials that contain a high density of hydrogen atoms[12], like organic materials. The use of magnetic components in any MRI setup is impossible.

X-ray tomography has been used to reconstruct the three dimensional stacking structure of granular piles [76, 77], and has been used to investigate the overall density of vibrated granular beds [78]. Also X-ray tomography can achieve very high resolution, but the scanning time can be up to a few hours, although recent development has decreased that scanning time to minutes. It requires substantial CPU time to analyze experimental data, partly due to the fact that direct imaging of cross-sections, as is done in MRI scanners, is not possible. Due to the ionizing energies of X-rays, also personal safety is a concern. MRI and X-ray based scanners can be used for both dry granular flows and suspensions.

Confocal imaging can nowadays image quickly, and with high resolution, both simple cross-sections and complete volumes. It can only be used for index matched[13] suspensions, since its imaging technique uses visible light to access the interior. It has however been developed to study small systems, with particle sizes ranging from hundreds of nanometers to a few microns, and scaling this technique up to systems with millimeter-sized particles poses significant challenges.

The essential advantages of IMS can now be summarized: the single slice illumination technique allows one to image a full cross section within only one

---

[12]Strictly speaking any non-magnetic material with a non-zero nuclear spin will suffice.

[13]Although the index matching does not have to be very well tuned, since the scatter of visible light with $\sim$ micrometer sized particles is not very much affected by interfaces with slightly different indices of refraction.

exposure time of a digital camera. The system sizes that IMS can image are only limited from below by the in-plane resolution. This resolution is set by the optics used, and can therefore be on the order of a few micron. The imaging speed is independent of the resolution, and set by the amount of fluorescent light available. In Chap. 4, we will describe an IMS we developed at Leiden University, in which exposure times of 10 milliseconds can be reached and still give sufficient contrast, putting the imaging rate of IMS on par with the fastest confocal scanners nowadays available. Scanning three dimensional volumes can be done by moving the sheet through the suspension, while taking pictures with a camera. Moving the sheet can be done at practically arbitrary rates[14], so three dimensional samples consisting of hundreds of cross-sections can be imaged within seconds.

Another advantage of the IMS technique is that it is cheap compared to the other techniques mentioned. The technology required is a standard workstation, a laser sheet on a translation stage, and a digital camera, so cost are about 10-20 k\$[15]. In comparison, an MRI scanner costs on the order of 1 M\$, X-ray tomography scanners cost several 100k\$, and a fast confocal 100-200k\$. These scanning techniques are also usually bought as stand-alone units, and cannot easily be adapted to the requirements of the specific experiment; IMS, with its simple components, can be almost freely adapted to any suspension and flow geometry.

There are also a few disadvantages to the IMS technique: only suspension flows can be images, since the particles always have to be studied in an index matched fluid. Voxel[16] resolutions are limited by the thickness of the laser sheet used, which is usually on the order of a few tens to a few hundred microns. The technique also requires very good matching of the refractive index of the particles and the fluid, otherwise light scatter will limit visibility to only a few layers in the bulk. We have so far been able to visualize 20-30 layers with relative ease.

---

[14] Mechanically, by moving the laser, or optically, by illuminating a cross-section via a rotatable mirror.

[15] The cost of software are not taken into account.

[16] A voxel is the three dimensional generalization of the concept of a pixel, a unit of surface.

Chapter 4

Towards Faster Flow Imaging

4.1 Introduction

Although the IMS approach can scan quickly in potential, the setup M described in section 3.2 has yet a very limited imaging speed. Increasing that would allow us to extend the exploration of the Newtonian regime, or to check the viscosity and density scaling predicted by the inertial number theory. Since particle *tracking* over an extended range of rotation rates would also become feasible, it would also enable us to look at the microstructure of the suspension flows. Evidently, faster imaging can give access to a vast amount of new physics.

In this chapter, we describe a new IMS setup under construction in Leiden, which can scan up to 100 times faster than the setup described in section 3.2. We will show that we can image flow speeds up to about 1 rps, and that we reduce the time to take three dimensional reconstruction scans to several seconds. In short, with this faster imaging system, we are able to image *faster* flows, and image flows *faster*.

We carried out preliminary studies of fast flows in the split-bottom geometry in this setup. We looked at the particle size dependence for 3 mm particle size suspensions. We also extended the range of flow rates imaged by a decade to 8.3×10^{-1} rps. This new regime of flow rates opens a whole new range of unexplored suspension dynamics, in which centrifugal forces overtake gravity. We also did some preliminary three dimensional scans, and show that three dimensional images, in which clearly identifiable particle are present, can be obtained within seconds.

To distinguish it from setup M described before, we will refer to this faster IMS setup as setup L.

4.2 Index Matched Scanning: Setup L
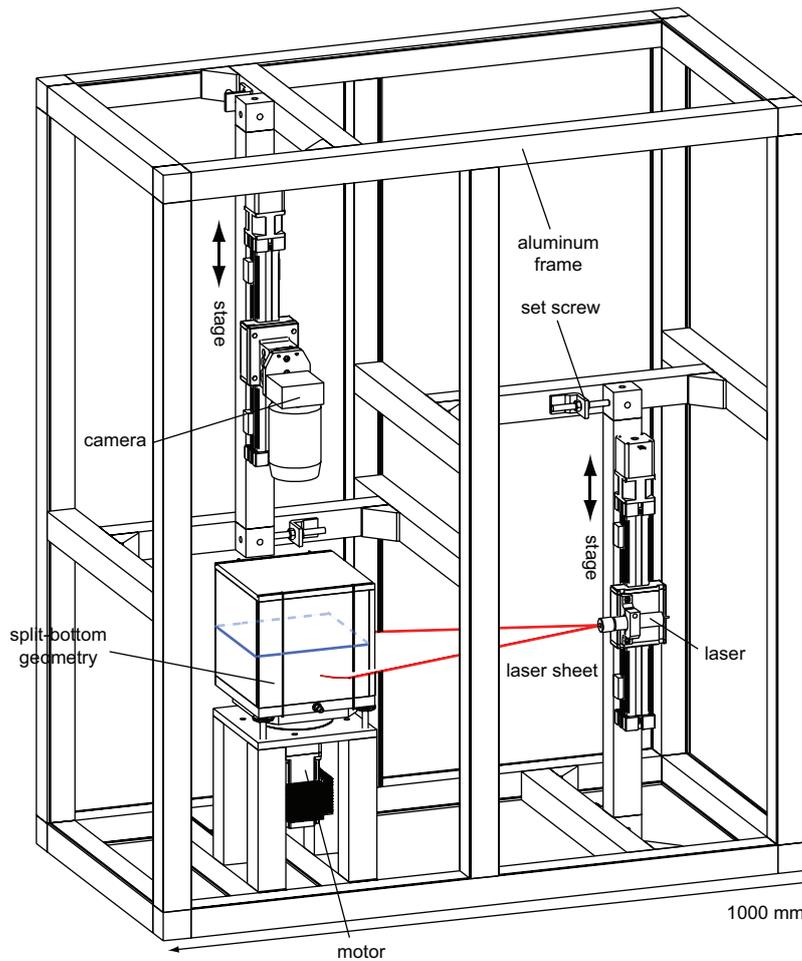
Figure 4.1: The setup under development in Leiden. The drawing is to scale. The aluminum frame can be closed off on all sides with opaque panels.

In order to increase the imaging rate in setup M, two main limitations had to be overcome: first of all, the imaging system used was not capable of storing

78

images fast. Secondly, the camera is positioned at a large distance from the measurement cell, which reduces the influx of light. We will discuss the solutions implemented to solve these problems first, and then we will describe the setup in full detail.

4.2.1   Increasing the Imaging Rate

Imaging system -- The main speed limitation for imaging systems nowadays is storing the digital images -- there is a tradeoff between having a small amount of fast memory modules that can be accessed quickly, or having a large amount of memory that can only be accessed relatively slowly. High speed cameras capable of imaging more than 1 million frames per second are commercially available nowadays [79], but they can typically only buffer a few thousand images, which after completing the acquisition have to be transferred to a permanent storage location at a much slower rate. Slower camera systems, that use computer hard drives as storage modules, can store up to 1 million images easily, but usually at a rate of a few tens of frames per second.

This limitation in imaging systems affects the way we improve the imaging rates in setup L. There are two ways of imaging suspension flows with IMS. In one approach, the position of the sheet inside the suspension is kept at a fixed position, and a number of images is recorded. To image another cross section of the flow, the sheet is moved and another set of images is acquired again. This method was used to obtain all the flow profiles shown in chapter 3. We will refer to it as *serial flow imaging*. One sequence of images is typically only 1000 images large, so only a high speed memory buffer of 1000 images has to be available to store the images temporarily before writing them to slower memory modules like a computer hard drive: this can be done at an arbitrary rate in the time between two recordings at different positions in the suspension.

To increase the imaging rates for serial flow imaging, we therefore use a high speed camera (Phantom V4.2).

The other way IMS can image suspension flows is by moving the sheet continuously through the suspension, while recording images. After the complete volume is traversed by the sheet, the process is repeated. With this method the whole three dimensional flow is imaged in parallel; we will refer to it as *parallel flow imaging*. The maximum displacement for a particle between two consecutive volume scans should be less than a particle radius[1]; only then can

---

[1]There are ways to loosen this constraint; for example using Particle Image Velocimetry (PIV) techniques first to subtract the overall mean displacement field, and then only to use particle tracking to extract the position or displacement fluctuations superimposed on the mean flow profile [80].

the particle trajectories in the three dimensional volume can be tracked, which is necessary for the study of diffusion of particles. Three dimensional imaging thus not only requires reasonably fast scanning to keep the total strain per consecutive volume low, it also requires significant amounts of memory space in the 'buffer' to store images acquired by the camera: A typical measurement requires 1000 three dimensional volumes of about 150 images each. Assuming that a typical image has 640x480 pixels, with a 12 bit depth, its size is $\sim$ 500 kB per image, and the total amount of data in this measurement is 75 GB. Most fast cameras, like the Phantom series, have only a few gigabytes of buffer memory, and will therefore not suffice for three dimensional imaging. Therefore, we use the DAS Digital Image Archiver system[2]. This system is capable of acquiring images from a high speed FireWire camera continuously, and storing images directly to the optimized hard drive on the workstation it is running on. The speeds at which it can acquire and save images are limited by the hard drive write speed, which is typically 50 MB per second. Assuming again a typical image size of 500 kB, this sets the acquisition of a full three dimensional stack of 150 images to 1.5 seconds. For comparison: this is comparable to the fastest confocal scanning setups nowadays available.

Photon flux -- To increase the frame rate with a faster imaging system, the exposure time per image has to be decreased. To keep a good contrast however, a certain photon flux has to reach the camera. To image faster, it is necessary to get more photons per unit area on the photosensitive CCD chip. In the IMS technique, the number of photons available per pixel is set by a few factors: the intensity of the laser beam, the total area of the laser sheet, the local concentration of the dye, the quantum yield[3] of the dye, the distance to the fluorescent spot, the aperture of the lens, and the quantum efficiency of the CCD chip.

In setup M, the main light capturing limitation is the distance to the fluorescent dye: the distance of the camera to the measurement cell is 2 meters. We recall that this is done to avoid issues with focussing on different imaging planes. To be able to achieve higher image acquisition speeds, we therefore placed the camera closer to the flow geometry to be studied. This necessitates moving the camera together with the illuminated plane. This is to keep the images focussed for all imaging locations inside the suspension. Therefore, the camera has to be mounted on a translation stage. This however also allows us to use a fixed focal length objective, which typically have a larger aperture. This

---

[2] From DVC Machinevision, Breda, The Netherlands; www.machinevision.nl
[3] This is the ratio of emitted over absorbed photons.

also increases the number of photons available per pixel.

A typical three dimensional scan is as deep as a typical filling height H in the split-bottom cell, so a few centimeters deep. The camera has to traverse this distance within the scan time of a complete volume, which is on the order of a few seconds. This limits the total weight of the camera; we therefore use a camera/lens combination with a total weight of around 300 gr.

4.2.2   Setup Description

The split-bottom setup type L is shown in Fig. 4.2. Its design is inspired by setup M described in a previous chapter; however in some crucial aspects the setup is different. Below, we will discuss the components used in setup L separately, as was done for setup M.

Laser --   The laser used in the setup was identical to the one employed in setup M. We use the external trigger capabilities of the laser to turn it on only during the camera exposure time. This limits the effects of photobleaching -- see section 3.2.2

Translation stages --   We use (BAHR ELK80) translation stages for both camera and laser motion. The stages are spring-loaded to ensure they have no backlash. The stages are capable of moving quickly, up to 10 cm per second, and can carry large loads. They are driven by high torque stepper motors from Lin Engineering (4118L-01). The stepper motors are controlled by stepper motor drivers (CDR-4MPS). The maximum[4] step size of the stages is 5 micron. The step size can be decreased by a factor 256 with the micro stepping capabilities of the stepper motor driver.

Digital camera --   The digital camera used to image the cross sections illuminated by the laser, is a Basler A622f FireWire camera. It is operated with the DAS Imaging Archiver software mentioned above. The QE maximum of the CMOS chip used in the camera is with 25% maximal between 550 and 650 nm. The resolution of the CMOS is 1280x1024 pixels. The exposure time can be adjusted between 80 microseconds to 0.32 seconds. The maximum frame rate at full resolution is 25 frames per second; the frame rate can be increased by using fewer pixels in the Region Of Interest (ROI). The lens used on the camera is a fixed focal length lens with an aperture of 2.8.

---

[4]Stepper motors have a fixed step angle (1.8° in this case. Microstepping drivers can reduce this fixed step angle by a certain factor.

Enclosure -- To reduce the influence of background light, the flow-box/laser/camera assembly is mounted in a custom-built dark enclosure. The whole setup is mounted on two stacks of concrete slabs; vibration damping is achieved by sandwiching rubber mats between the concrete slabs.
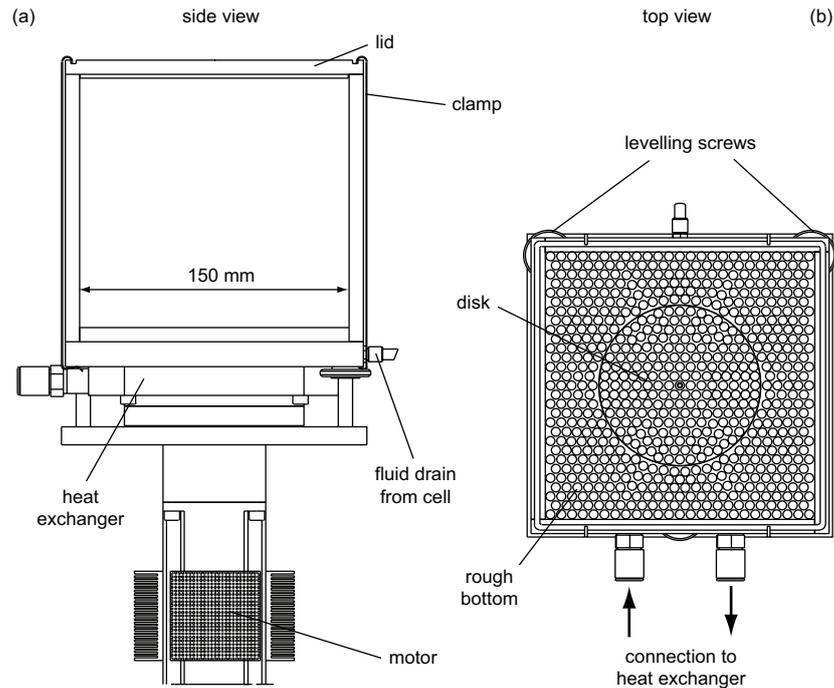
Figure 4.2: The split-bottom cell in setup L. (a) is a side view, (b) a top view. The heat exchanger is discussed in section 4.4.

Flow geometry -- The split-bottom geometry has the same design and size as type M described in the previous section. It is a square box of 15 cm sides, measuring 20 cm in height. In this setup however, the walls of the box are made of glass, to allow for the use of more aggressive index matching fluids[5]. The disk in this setup is driven by a stepper motor (Lin Engineering 5718L-01P), with a micro stepping driver (CDR-4MPS). The minimum step angle is $0.007°$. The bottom of the box, as well as the disk, are made rough with a hexagonal (i.e.

---

[5]Some fluids with a high index of refraction, such as Eugenol, dissolve PMMA. See section 4.4 for an overview of index matching fluids, particles and considerations

ordered) array of conical holes, with a maximum cross section of 5 mm (similar to the setup described in section 2.2). The box can be sealed with a transparent lid, to be able to use index matching fluids that degrade when exposed to air, like Eugenol, but also to prevent evaporation of solvents in the index matching liquids, which changes its index of refraction.

Environment -- The setup is placed in a lab with only modest temperature and humidity control. Depending on the season, the relative humidity ranges from 20 to 50%, and the temperature varies between 20 and 25 °C. Both variables affect the evaporation rate of the water in the Triton-based index matching liquid, and therefore the viscosity and density of the fluid.

4.3 Preliminary Experiments

In this section we describe several preliminary experiments that demonstrate the functionality of setup L. We check whether the inertia theory scaling is indeed independent of particle size, by studying flow profiles and rheology of a PMMA/Triton suspension with 3.2 mm sized particles. Surprisingly, we find that the flow profiles, in contrast to rheology and inertial theory scaling, shows a particle size dependence.

We also look at what happens to suspension flows at rotation rates higher than reported in chapter 3 -- for example the centrifugal force at some rotation rate overtakes the gravitational force in magnitude. The onset of the influence of centrifugal forces is already apparent at rotation rates of 3.3 $\times 10^{-1}$ rps, i.e. at much lower rotation rates than one would expect from the relative size of the gravitational and the centrifugal forces.

Setup L is designed with fast scanning in mind. We show that the setup delivers: one of our first tests was a three dimensional scan of an index matched suspension. The total scanning time was three seconds -- the result of the scan is discussed in section 4.3.3.

4.3.1 Triton Suspensions: Different Particle Size

The inertial number for fluid-saturated granular flows, $I_S = \frac{\dot{\gamma}\eta_f}{P_g a}$, is independent of particle size, as we have seen in section 3.4.2. To test this, we image the flow of 3.2 mm (1/8") PMMA particles suspended in the Triton mix. We use a filling height $H/R_S = 0.5$, since for that filling height the transition from dry granular flows to the Newtonian regime is best observable in the flow profiles.
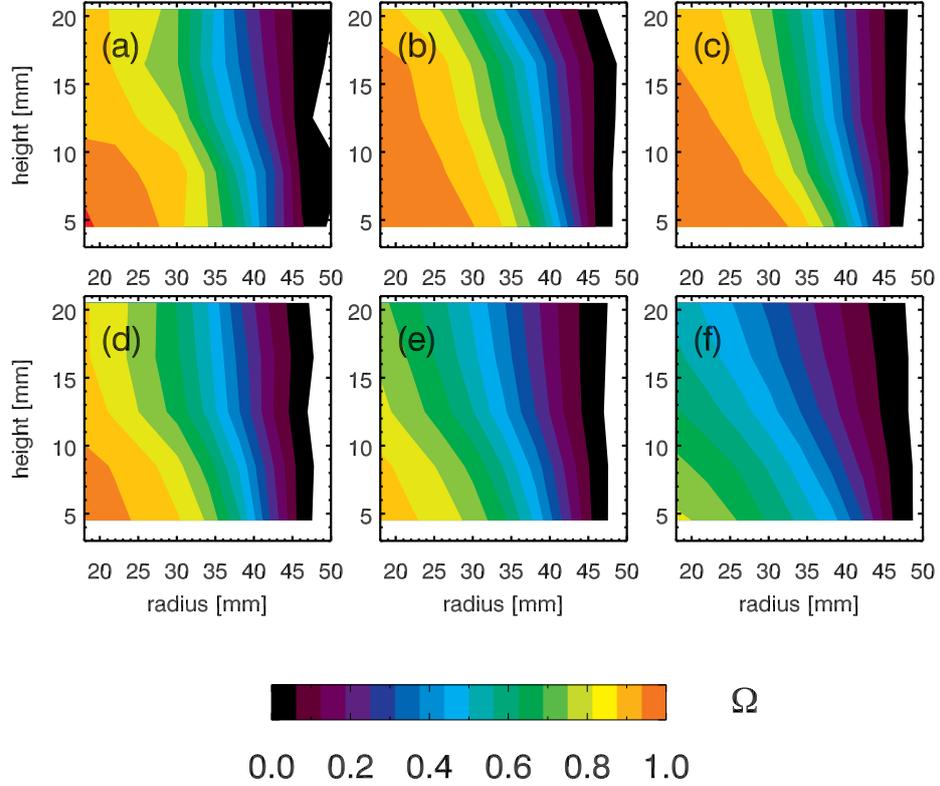
Figure 4.3: Normalized angular velocity profiles for 3.2 mm PMMA particle suspension. Different rotation rates are depicted: (a) - (f) are $\Omega = 1.6 \times 10^{-6}$, $1.6 \times 10^{-5} \dots 1.6 \times 10^{-1}$ rps. Color schema as indicated in the color bar, ranging from 0 to Ω. Surface of suspension is at 23 mm.

We image the velocity profiles for over a large range of rotation rates: $\Omega = 1.6 \times 10^{-6} \dots 1.6 \times 10^{-1}$ rps. For Ω below 5×10^{-5} rps, the interframe time is always larger than 40 seconds, which is enough time to image the slices at the five different heights (4.5, 8.5, 12.5, 16.5, 20.5 mm) we use to measure the flow profile. This means that for these slow runs, we image in parallel mode. The interframe time decreases from 300 seconds at the lowest rotation rate measured, to 150 milliseconds at the fastest driving rates. For the slowest two rotation rates measured, the total strain is about half a rotation of the disk, which

may not be enough to set up a steady state flow throughout the whole cell, as was observed in [37], Fig. 5. Note that in this experiment, we used a Foculus FO 432b camera, instead of the Basler camera mentioned earlier.

For the slowest runs, that take a few days to complete, we prepare the index matching fluid slightly differently; see section 3.2.2. Instead of using the recipe with a substantial amount of water and zinc chloride, as was used for the measurements at higher rotation rates, for the low rotation rates of $\Omega = 1.6 \times 10^{-6}$ rps, we now add only enough water and zinc chloride to make the dye have the proper absorption and emission spectrum. The reduced amount of zinc chloride used reduces its precipitation, so that the fluid is usable for several days, which increases the total useful measurement time.
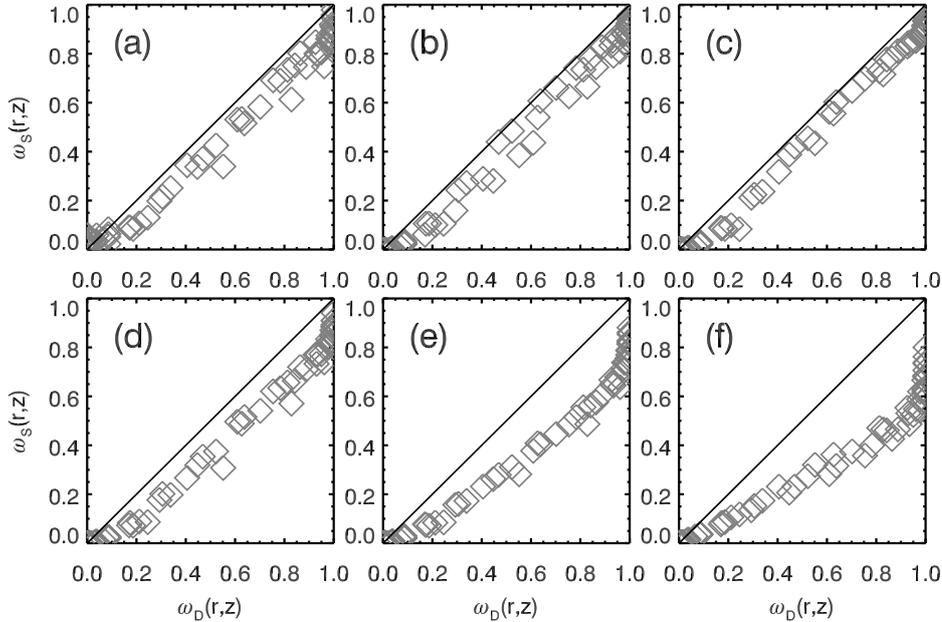
Figure 4.4: A comparison between the normalized angular velocity profiles and the dry granular flow equations. Again, different rotation rates are depicted: (a) - (f) are $\Omega = 1.6 \times 10^{-6}, 1.6 \times 10^{-5} \ldots 1.6 \times 10^{-1}$ rps.

Slow flow limit -- The results of the experiments are shown in Fig. 4.3. Note that we imaged more rotation rates than shown in that figure (11 in total); we

leave half the data out for clarity. From the contour plots, it is again obvious that at lower rotation rates the flow profiles are very similar to dry granular flows. This is shown in more detail in Fig. 4.4; the point-by-point comparison with the dry granular flow model is quite good at the lower rotation rates. The comparison for $\Omega = 1.6 \times 10^{-6}$ rps seems slightly worse; in that experiment the limited amount of strain may impede the matching to the dry flow profiles.
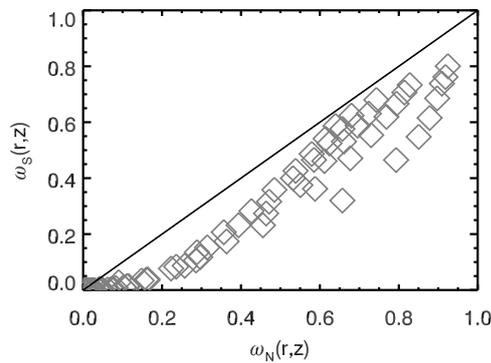
Figure 4.5: The comparison of the normalized angular velocity profile data from the 3mm PMMA suspension to the Stokes flow solution. The suspension was driven at $\Omega = 1.6 \times 10^{-1}$ rps.

Fast flow limit -- We compare the velocity profile measured at 1.6×10^{-1} rps with the Newtonian profile in Fig. 4.5. We see again that the flow profiles for the suspension tends towards Newtonian behavior, although the suspension with the 4.6 mm particles was already almost fully Newtonian at half that rotation rate. This suggests that the rate dependence of the flow behavior for these 3.2 mm suspensions is different from the 4.6 mm suspensions.

To see how strong the particle size dependence is we compute for each rotation rate the average mean squared difference $\sum (\omega_S(r, z) - \omega_D(r, z))^2/N$ between the measured velocity profiles and the dry granular flow equations. Here N is the total number of datapoints for which the normalized angular velocity $\omega(r, z)$ is available. The onset of rate dependence should then be visible as an increase of this quantity with increasing Ω -- indeed we see this quantity rise earlier for the 4.6 mm suspension than for the 3 mm suspension; see Fig. 4.6a.

Mismatch in rate dependence -- What can explain this large mismatch observed in the moment of the onset of rate dependence in the velocity profiles for the two different suspensions? From the scaling arguments, it is unlikely that this is due to the particle size. Moreover, the rheological data of the 4.6 and 3.2 mm suspensions (reproduced from section 5.4.2 in Fig. 4.6b), are virtually indistinguishable from each other, although a small particle size cannot be ruled out.

One difference between the two experiments is the temperature of the fluid: Setup M, in which the 4.6 mm particles were imaged, was located in a laboratory with temperature control, and room temperature there was never higher than 22 °C. Setup L does not have temperature control. Moreover, the stepper motor used to drive the disk was directly coupled to the bottom of the flow cell, and warmed up substantially when in use. This heated the fluid to a temperature of about 27 °C. In appendix 5.7.2 it was shown that Triton has modest temperature dependence in its viscosity between 22 and 27 degrees; its viscosity changes by almost a factor 2 in that range. The 3.2 mm particle suspension experiments were therefore most likely carried out with an index matching fluid that had a lower viscosity, which would shift the onset of rate dependence to higher rotation rates, consistent with the trend observed in the data.

The other difference between the two suspensions is the preparation of the index matching fluid. Small variations in the amount of water mixed into Triton can change its viscosity substantially. Combined with the temperature dependence of the fluid, we can most likely account for the shift on the logarithmic scale in Fig. 4.6, between the data sets for the different suspensions.

We conclude that the mismatch in the rate dependence for the suspensions with different particle sizes is therefore most likely due to experimental issues.

4.3.2 Fast Flows

The role of centrifugal forces -- In the limit of very high rotation rates, the centrifugal force on the particles starts to dominate over the gravitational force. We have already seen this in chapter 2. There, we estimated, on the basis of the balance of centrifugal force and gravitationally induced frictional forces that the centrifugal forces come into play at rotation rates of 1 rps and higher. However, as shown in the appendix 3.6 of chapter 3, the centrifugal force also sets up a counterclockwise (as seen looking into the direction of the rotational flow) secondary flow in Newtonian fluids, driven in the split-bottom geometry. We know from the previous two chapters that above 0.1 rps the suspension starts to behave as a Newtonian fluid. So at the rotation estimated above, the secondary flow in the fluid has already developed substantially, and is probably
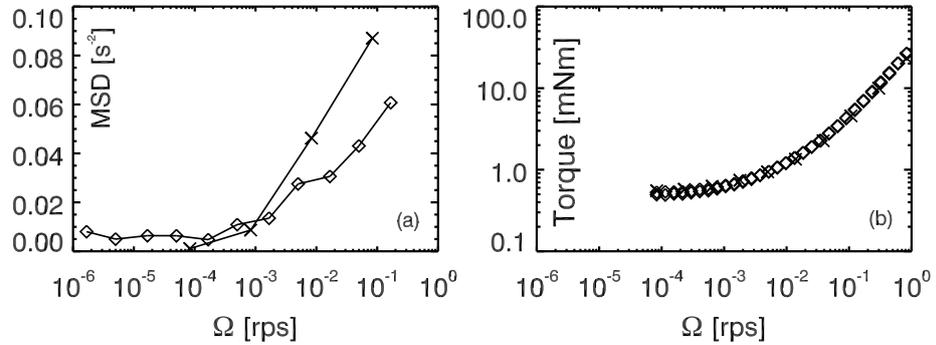
Figure 4.6: (a) The average mean squared difference (MSD) as a function of Ω. For small Ω, the MSD is small since the flow resembles dry granular flows. Symbols: $\diamond$ = 3 mm PMMA particles, $\times$ = 4.6 mm PMMA particles. (b) $T(\Omega)$ of the two different suspensions. Symbols are the same as in (a).

the dominant driving mechanism of all radial particle motion.

Radial flow measurements -- To clarify whether centrifugal force alone, or the secondary flow itself is dominating the particle motion in the suspension flow, we image a vertical cross section of the flow in the split-bottom setup, while rotating the disk at 0.016 to 0.8 rps. We use a filling height H/R_s of 0.5. To image the fast flows, we use a Phantom V4.2 B/W camera (512x512 pixels, 8 bit) with an exposure time of 10 ms. See Fig. 4.7 for a schematic drawing of the setup.

In Fig. 4.7b-e, snapshots of the surface structure are shown. The overall shape of these structures is stable in time. At 0.016 rps the surface of the suspension is flat, except for the heaps at the edges, which are present even without rotation and can be removed by more careful leveling of the surface. We see that at 0.16 rps, a small dip is developing in the center of the suspension. The dip becomes more pronounced at 0.4 rps, and at 0.8 rps, the whole center is empty of particles. This rotation rate is well below the estimate based on the balancing of frictional and centrifugal forces on an individual particle. Most likely, the secondary flow that develops in the fluid/particle mixture, that is essentially Newtonian around 0.1 rps, drives the particles outward. Note that the flat surface of the suspension restores itself almost completely after switching of the driving disk.
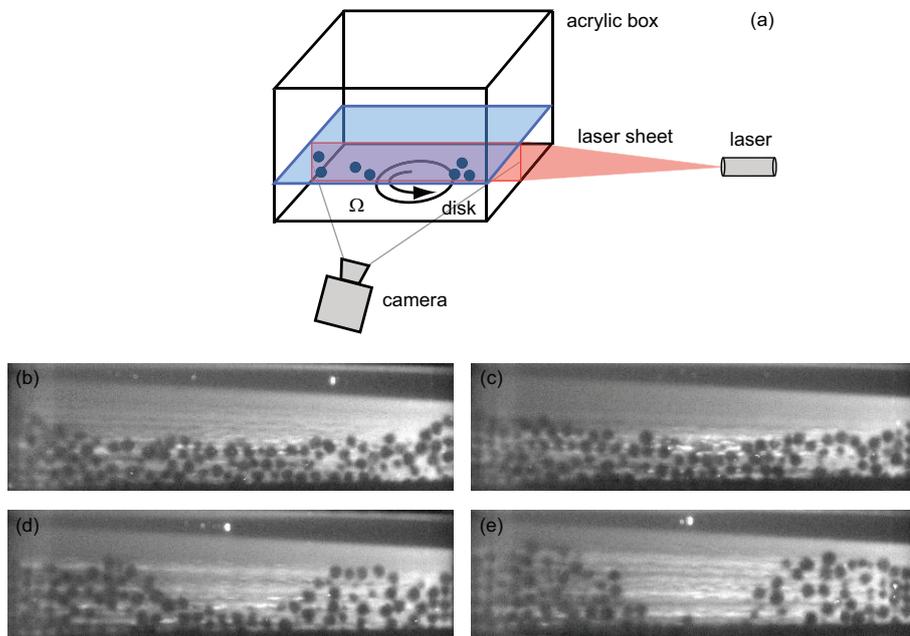
Figure 4.7: The setup used to look at the surface structure of the fast flows is shown in (a). Typical snapshots of surface structures are shown in (b)-(e), for different Ω: 0.016, 0.16, 0.48, 0.8 rps.

4.3.3 Three Dimensional Scanning

A very early test in which a full three dimensional reconstruction scan was taken with setup L is shown in Fig. 4.8. Each reconstruction scan consists of 125 scans, acquired in less than 3 seconds. The number of slices per cm is 30. Only histogram equalization (see appendix 8.1) was applied to improve the contrast; no band pass filtering [81] or smoothing was used. The reconstruction scans have enough contrast for particle tracking methods [82]. The streaks visible at the surface are due to a slight index mismatch between particles and fluid. This also reduced the resolving power at greater horizontal depths -- in the second half of the box laser scatter makes distinguishing particles by eye impossible.

4.4 Improvements

Setup L is still under continuous development and offers many directions in which its functionality can be improved rather easily and fruitfully. In what
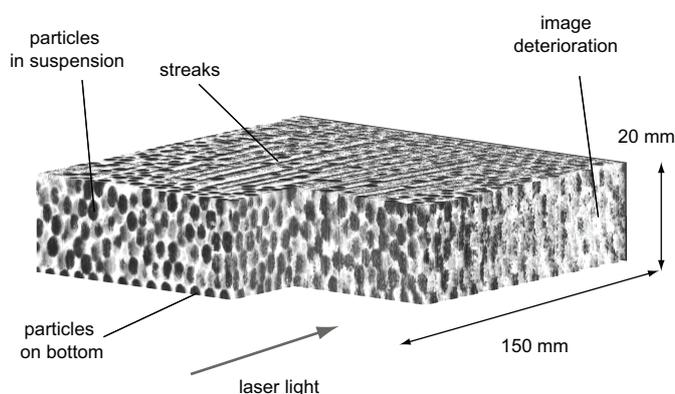
Figure 4.8: A three-dimensional reconstruction scan acquired in setup L. Particles and direction of the laser light are indicated.

follows, we give a list of possibilities. We discuss how different suspensions can give access to different regimes of suspension flows, or even allow one to combine rheology and imaging. We also discuss several different ways to improve the imaging methods we use now, and mention some other simple modifications that have been made since the experiments, mentioned in this chapter, were carried out.

4.4.1   Other Suspensions Types

The physics of suspensions depends on the relative densities of particles and fluids and the viscosity of the fluid. In particular, the inertial number for suspensions introduced in section 3.4.2 depends directly on the viscosity, and the granular pressure, which is set by $\Delta\rho$, the density difference between the fluid and the particles used. Here, we list a few different fluids and particle types that can be used for index matching. We have not used them extensively, so the list of their advantages and disadvantages is not exhaustive. Naturally, to verify scalings in rheological experiments, the restrictions on particle properties are much less severe.

Other particles -- Besides PMMA, there is another material which is used to produce spherical particles, and which has a low index of refraction: borosilicate glass. Sigmund Lindner for example sells borosilicate glass spheres (type P), with an optical index n_D of 1.47. The glass beads do not absorb any fluids, and therefore are not susceptible to index changes or cracking, as the PMMA

particles are.TThey can also be washed and reused in different index matching liquids. The bulk density ρ_p of the particles is 2.4 $\times10^3$ kg/m³. This makes them heavier than PMMA, and they can therefore not be density matched with Triton. Note that Mo-Sci also sells borosilicate glass spheres with the same low index of refraction, but they seem to display surface defects that scatter light and hence render them unusable for the scanning techniques.

Dimethyl Sulfoxide -- [6] Dimethylsulfoxide (DMSO) has an optical index n_D of 1.479, and can therefore be used to index match both PMMA and borosilicate glass spheres (the latter treated below). It has a viscosity of 2 mPa·s, and a density of 1.1 $\times10^3$ kg/m³. DMSO mixes very well with water, so its index can be tuned simply by adding water. Adding NaI[7] to the solution can increase the density of the fluid, to match the density of PMMA.

The amount of water one needs to reduce the index of DMSO to that of the borosilicate glass spheres is not enough to use Nile Blue 690 perchlorate -- with such a small amount of water its spectrum will not be tuned to the wavelength of the laser. In DMSO, we use Atto 633, a rhodamine based dye that is not very expensive and made to absorb light at 633-635 nm. The dye dissolves very well in both DMSO and water.

Eugenol -- Eugenol is a relatively safe and cheap liquid with very high index of refraction (n_D =1.541). Its index can be tuned with ethanol with which it mixes very well. It has a low viscosity of 2 mPa·s, comparable to that of DMSO. Its disadvantages are that it degrades over time when exposed to oxygen, and it has a very strong clove-like odor. It also dissolves PMMA, so it cannot be used with PMMA particles. The density of eugenol is 1.06 $\times10^3$ kg/m³; it is compatible to Nile Blue 690.

Sodium Polytungstate -- SodiumPolyTungstate (SPT) can be used if a high density liquid is necessary. It is a salt that mixes well with water, and it can therefore be used to make a solution whose density can be tuned between 1 and 2.8 $\times10^3$ kg/m³. The index of the solution changes with its density from 1.33 to values larger than 1.6. Note that its viscosity also increases with its density. We verified that it is compatible with Nile Blue; Nile Blue 690 added to an SPT solution remained blue for a timespan of several days, after which we stopped observations.

---

[6]Many thanks to Kinga Lorincz for sharing this recipe with us.

[7]Mixing NaI with water and DMSO will result in a yellow liquid. Adding a small amount of sodium thiosulfate removes this coloring.

The high density of SPT combined with its index matching capabilities can be used to do rheology and flow imaging simultaneously in the following way.
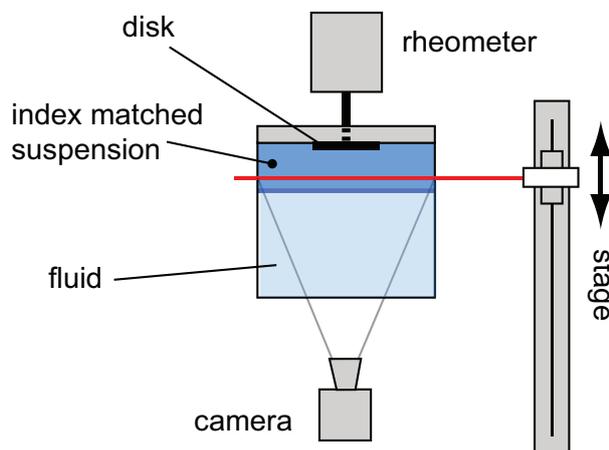
Figure 4.9: An hypothetical 'inverted' flow cell, capable of simultaneous imaging and rheology. The particles in the suspension are pushed upwards due to buoyancy.

In the present setups, the disk used to drive the flow is located at the bottom, and the flow is imaged from the top. The motor cannot be used to do rheological experiments -- ideally, one would like to drive the disk with a rheometer that can record the applied torques while driving the flow. However (stress driven) rheometers typically drive a system from above, and in the current setup the imaging devices is already located there. Another drawback of driving the suspension from above with a rheometer, is that it requires the presence of a suspension-penetrating rod, connecting the driving disk and the rheometer, which blocks parts of the laser sheet.

With an SPT solution, index matched to borosilicate glass spheres, these problems can be solved: SPT at this index of refraction has a density higher than that of the glass spheres, so the buoyancy force on the submersed particles then pushes them up, which makes driving the system from above necessary. The system can this be driven from the top with a rheometer, and imaged from below. See Fig. 4.9 for a schematic drawing of this setup

4.4.2   Imaging Improvements

Small fan angle laser sheet --   It is possible to increase the photon yield substantially by using a line generator with a smaller fan angle. This can be used if one is only interested in a small subsection of the flow -- the same output power of the laser is then distributed over a smaller area. This can be used both for two dimensional cross section studies of very rapid flows, but also for rapid three dimensional scanning of small volumes. We used a $5°$ fan angle to achieve an increase in fluorescence of more than a factor 10.

Wavelength filter --   Particle Tracking Velocimetry (PTV) methods applied on the three dimensional reconstruction scans obtained by parallel imaging are sensitive to image noise. One source of image noise is (Rayleigh) scattering of the laser light on objects in the flow cell. The scattered photons will show patterns and spots in the scanned images: see for example Fig. 3.2. In these images, the disk at the bottom is clearly visible, while only a cross section of the fluid far away from the disk is illuminated.

To reduce the influence of Rayleigh scattered photons on experimental images, a filter is used, that blocks all light that does not come from fluorescence. Since the emission peaks of the fluorescent dyes are tens of nanometers in width, and since all the fluoresced light can be used to enhance contrast, we use a longpass filter, that filters out the light below a threshold wavelength. Nile Blue 690 perchlorate fluoresces at wavelengths > 690nm, so with this dye we use a cutoff wavelength of 665 nm. The dye Atto 633, necessary in combination with DMSO, has a much smaller Stokes shift, i.e. its emission peak at 657 nm is very close to that of the excitation laser wavelength of 633 nm. Therefore a longpass filter with a steep edge around 640-650 nm is required.

Larger aperture lens --   Fixed focal length optics with an aperture of 0.95 are available from Schneider. The large aperture in these lenses increases the amount of light by a factor 2 to 4 with respect to the current lenses used. This translates into more contrast, or allows for faster scanning. The Schneider lenses have the drawback that they can only be used with the Atto 633 dye, since they are designed for wavelengths λ between 400 and 700 nm, and the light emitted by Nile Blue 690 perchlorate has λ > 700 nm.

4.4.3   Miscellaneous

Different Bottom Roughnesses -- The hexagonal pattern of holes drilled in the bottom plate tends to induce crystallization for the 4.6 mm PMMA spheres

we have used. For 4.6 mm spheres, we will therefore use a bottom plate with a different roughness: the bottom plate will have holes of

Temperature control -- The viscosity, index of refraction and density of the fluids and particles all depend on temperature. It is therefore important to keep the temperature as constant as possible. To ensure temperature stability in the system, we mounted a heat-exchanger to the bottom of the disk. The heat exchanger, connected to a heat circulator (Haake EZ Cool 80) keeps the temperature of the measurement cell constant to within 0.1 $^\circ$C in the range of -20 to 80 $^\circ$C. Note that this temperature control was not implemented when doing the experiments described in section 4.3.1.

4.5 Conclusions

In this chapter, we have described the development and some testing of a new fast IMS setup. We have shown that we improved the scanning time with respect to setup M by more than an order of magnitude. We have demonstrated that setup L is capable of carrying out the same experiments as were done in setup M.

We have shown that being able to image suspension flows faster gives access to new types of flow. Furthermore, we have shown that there is still a substantial amount of simple improvements to be made, that can extend the applicability of the fast scanning setup even more.

Chapter 5

Gravitational Suspensions: Rheology

5.1 Introduction

In this chapter, we study the *rheology* of gravitational suspensions in the split-bottom geometry and test whether their rheological signature is consistent with their flow behavior observed in chapter 3. For example, we observed in the flow profiles that PMMA/Triton suspensions display a transition from a rate independent, dry granular regime to an approximately Newtonian rate dependent flow regime -- we will find a similar transition in the rheology.

In chapter 3 we derived a local flow rule for rate dependent suspension flows. This local flow rule is a relationship between the local stresses and strain rate, and therefore also predicts the outcome of rheological experiments. We observed that the inertial number based local flow rule summarized in Eq. 3.11 describes the flow profiles of suspensions in the split-bottom geometry well.

The rheology experiments reveal that the model is indeed capable of capturing the the essential features of the flow properties of suspensions.

For slow driving rates, we find that the rheology is rate independent. This suggests that the flow of suspensions at small driving speeds is dominated by frictional interactions. This enables us to measure the lubrication of particles in a suspension, since we know (chapter 2) that an effective friction coefficient of granular materials can be measured in the split-bottom geometry by measuring $T_0(H)$, the filling height dependence of the driving torques in the rate indepen-

dent regime. We use this method to measure and compare the effective friction coefficients of both submerged and dry spherical PMMA particles. The naive expectation would be that the presence of a fluid will lubricate the contacts between particles and give rise to a smaller effective friction coefficient. We find that this is not the case -- the effective friction coefficient of PMMA particles suspended in Triton is within error bars indistinguishable for that of dry PMMA particles.

For faster flows, the rheology shows a transition to essentially viscous behavior.

Suspension viscosities have been studied intensively since Einstein's seminal work in the early 20th century. We can also use the split-bottom to investigate the effective viscosity. Since we only focus on gravitational suspensions, we necessarily always look at dense suspensions. Surprisingly, we find only a very small increase of the viscosity, of less than a factor 4. A very common viscosity model such as the one by Krieger and Dougherty [83] would then predict that our particle density in the suspension is about 37 %. For the driving rates at which this value is observed, as discussed in section 1.5, this value is far too small.

5.2   Rheology Setup

We perform the rheological experiments in the same setup described earlier in section 2.2. It consists of a square box of 150 mm width and a 120 mm height, with glass sidewalls and an aluminum bottom. In the center of the box, a recessed region is made in the bottom, in which a disk with radius $R_s = 45$ mm can rotate. The disk is driven from above with a rheometer (Anton Paar MCR 501). Both the bottom and the disk are made rough to ensure no-slip boundary conditions by drilling conical holes in them in a regular pattern. See Fig. 2.1 for more details.

Temperature control is achieved with a Peltier element (Anton Paar P-PTD200) mounted beneath the bottom of the disk. The cooling to the peltier element is supplied by a heat circulator bath (Haake DC10), and allows us to set the temperature to any value between 15 and 35 °C.

For all experiments described in this chapter, we use the 4.6 mm diameter PMMA particles described in section 3.2.1. These particles were also used for the flow visualization experiments described in chapter 3. To check for particle size dependence in the rheology, we also used 3.2 mm PMMA particles in one experiment -- see section 5.4.2.

5.3   Suspension Rheology in the Split-Bottom Geometry
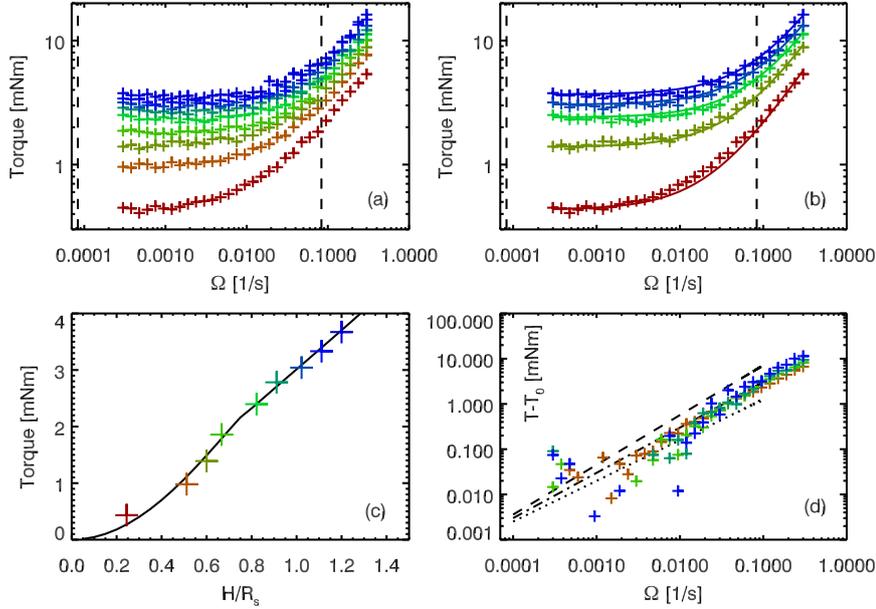
Figure 5.1: Rheology of 4.6 mm PMMA particles in pure Triton X-100. $T(\Omega)$ for several different filling heights; color indicates H/R_s. (a) shows the average torque as a function of driving rate. (b) Shows the same data, including a fit of the form $T = T_0 + C\Omega$; some filling heights are left out for clarity. The dashed lines in (a,b) show in which regime of rotation rates the velocity profiles were also measured as described in chapter 3. (c) shows the $T_0(H)$, the plateau values as a function H; the symbol size represents the approximate error on the data. Compare (c) to Fig. 2.5a. In (d) we subtracted the low Ω limit plateau values from the data. The lines have different slopes: dash: 1.1; dot: 0.9; dashdot: 1.0.

We measure $T(H, \Omega)$ for nine different suspension filling heights, and a range of rotation rates: H/R_s = 0.24, 0.51, 0.60, 0.67, 0.82, 0.91, 1.0, 1.1, 1.2, for $\Omega = 3.0 \times 10^{-4}$ to 0.3 rps. During an experimental run, Ω is swept from low to high values; we average the measured torque values over at least 3 rotations, usually over much larger strains. The transients in the rheological data are always around 10-20 seconds, no long time transients have been observed in the split-bottom rheology. See appendix 5.7.1 for a more elaborate exposition of the transients in the rheology of gravitational suspensions.

For these rheology experiments, index matching is not necessary, but an accurate determination of the density of the fluid is required. Therefore we use pure Triton X-100 to make the suspension, whose density can be measured accurately and does not change at all over the course of the experiment, as might be the case when adding water to the Triton: water slowly evaporates from the system. We add 4.6 PMMA particles described elsewhere in this thesis. The temperature in all these experiments is fixed at $25°$.

We make sure that there is always at least half a centimeter of fluid above the suspension to ensure that the surface tension of the fluid will not affect the dilation of the packing. The disk is positioned 1 mm above the static bottom to avoid the singularity discussed in chapter 2.

The results are shown in Fig. 5.1a. The trends in the rheology are essentially similar for all three filling heights: we see a rate independent regime at small driving rates, which crosses over into a rate dependent regime around $\Omega \sim 0.01$ rps.

The flow profiles over the whole range of rotation rates covered in the flow experiments were qualitatively consistent with the local stress-strain rate relationship $\tau(\dot{\gamma})$ summarized in Eq. 3.11:

$$\tau = \mu_0 P + \mu_1 \frac{\eta_f \dot{\gamma}}{\alpha}.$$ (5.1)

This relation also gives a prediction for the global driving torque $T(H, \Omega)$ in the suspension flows, which is the quantity to which we have experimental access. To obtain this prediction, one would have to integrate the above equation over an arbitrary surface in the flow. Unfortunately, we do not have access to the whole strain rate field in the suspension flow, so we cannot perform this integration. However, since the only Ω-dependence is in the $\dot{\gamma} = \dot{\gamma}(r, z)$ term, as long as the flow profile $\dot{\gamma}$ does not change strongly nonlinearly with Ω, we can write

$$T = T_0 + C\Omega,$$ (5.2)

with T_0, C fitting parameters that depend on H. We show this fit in Fig. 5.1b -- it fits the data very well, considering that there is only one fit parameter, namely C. We now discuss the rate independent and -dependent regime in more detail.

Rate independent regime -- At small driving rates, there is a rate independent regime, where $T(H, \Omega) = T_0(H)$. This is in line with the observations in the flow profiles: in the flow profiles we observed that in the slow driving rate

limit, the suspension flow profiles are rate independent and essentially similar to flow profiles of dry granular flows. This suggests that rate independent frictional interactions dominate in that regime. More evidence for this picture comes from a comparison of $T_0(H)$ to the Unger model prediction in Fig. 5.1c, a model discussed in section 1.5.3 that is based on purely frictional interactions and which predicts the height dependence of the driving torque. The $T_0(H)$ for the suspension is very well fitted by the Unger model predictions. For the fit we take for ρ the buoyancy corrected density of the PMMA particles; the friction coefficient μ is obtained by minimizing the total squared difference $\Sigma(T_m - T_U)^2(\mu)$ between data T_m and the Unger model T_U. The minimum is at $\mu \sim 0.59$. In the next section we will see whether the friction coefficient for wet particles is the same as for dry particles.

Rate dependent regime -- The driving rate at which the stresses become rate dependent, around $\Omega \sim 0.01$ rps, is consistent with the point where in the flow profiles significant deviations from 'dry granular' flow profiles are observed; cf. Fig. 3.6. The onset of the rate dependence is not related to the change in the surface structure as observed in section 4.3.2 -- that occurs at driving rates of $\gtrsim 0.5$ rps only.

The quality of the fit of Eq. 5.2 is reasonable, but deviations are visible in the onset of the rate dependent regime. This could be due to transients detailed in appendix 5.7.

In Fig. 5.1d we look at whether Newtonian behavior is observed in the rate dependent part. We show there the same experimental data as in Fig. 5.1a,b, but now with the mean of the 5 data points at the lowest Ω subtracted. We see that power law behavior $T \sim \Omega^n$ is observed, with $0.9 < n < 1.1$; consistent with Newtonian behavior, for which $n = 1$.

5.3.1 Comparison to Dry PMMA Particles

To compare the friction coefficient of wet and dry PMMA particles, we do experiments to extract $T_0(H)$ of dry PMMA particles. We make sure that we use clean, new PMMA beads from the same manufacturer and from the same production batch, since surface properties strongly influence the effective friction coefficient on granular materials [84]. In these experiments, also humidity control is used, since capillary condensation of water or other liquids can strongly affect the rheology of granular materials [85]. The relative humidity is controlled at $\sim 7\%$ by sealing the box and rheometer head with plastic wrap, and flushing the enclosed volume with dry, pure nitrogen gas.

We show $T(H, \Omega)$ for several different filling heights ($H/R_s = 0.11, 0.22, 0.33,$
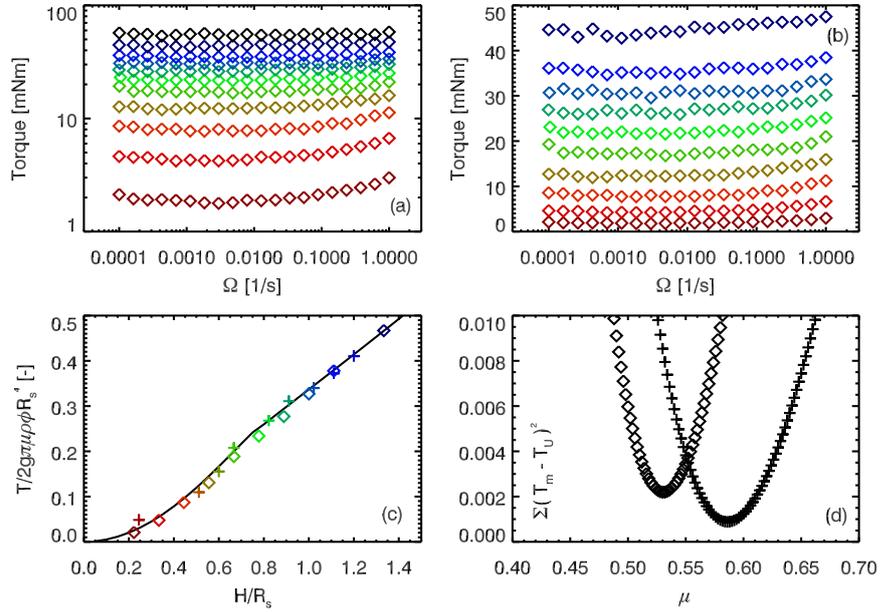
Figure 5.2: (a,b) Rheology of dry 4.6 mm PMMA particles in pure Triton X-100. $T(\Omega)$ for several different filling heights; color indicates H/R_s. (a,b) show the average torque as a function of driving rate on different scales. (c): The plateau values of $T(\Omega)$ for both dry particles ($\diamond$), and for the wet PMMA particles (+) from Fig. 5.1, together with the Unger model prediction (dotted line). (d): The total squared difference $\Sigma(T_m - T_U)^2$ between data and model as a function of μ; again for both dry particles ($\diamond$), and for the wet PMMA particles (+).

0.44, 0.56, 0.67, 0.78, 0.89, 1.0, 1.1, 1.3, 1.6) and for $\Omega = 1 \cdot 10^{-4}$ to 1 rps in Fig. 5.2a,b. From this data, which is rate independent in the low Ω limit, we extract the rate independent plateau values $T_0(H)$, and plot them as a function of H/R_s in Fig. 5.2c; for comparison, the data for the submerged particles is also included (+ - symbol). The data fits the Unger model well for a friction coefficient of $\mu = 0.53$. We extract this friction coefficient in the same way as was done for the suspension data: we minimize the total squared difference $\Sigma(T_m - T_U)^2(\mu)$ between the model and the experimental data. The approximately parabolic total squared difference function is shown in Fig. 5.2d.

Fig 5.2d shows that we cannot distinguish the friction coefficients of dry and wet PMMA particles; the difference in μ indicated in that panel of about 10% is within the compounded uncertainty from PMMA and Triton density; the

buoyancy corrected density of wet PMMA is 1.10×10^2 kg/m³, with an error of 0.14×10^2 kg/m³, since the relative error on the determination of the density of both PMMA and pure Triton is 0.1×10^2 kg/m³.

This however also sets an upper limit of any lubrication effect. The minute difference in friction coefficients however does not imply directly that submersed granular materials do not flow more easily; the frictional forces between particles is still reduced by the buoyancy, since buoyancy reduces the normal forces between particles.

5.4 Different Suspensions Composition

In this section we will examine whether different suspension compositions change the rheology of suspensions significantly. We try two different suspensions: first we add the chemicals necessary to make Triton index matching with PMMA to the PMMA/Triton suspension mentioned above. Secondly, we will change the particle diameter of the suspension from 4.6 to 3.2 mm.

5.4.1 Adding Index Matching Components

We probe the rheology of index matched suspension for which we also obtained flow profiles. The fluid used has the same composition as was used for the index matching, with 78 % Triton X-100, 13 % water and 9% $ZnCl_2$ by weight -- the recipe from Ref. [61].

As above we measure the average driving torque $T(H, \Omega)$ necessary to sustain rotation of the disk for rotation rates $\Omega = 8.3 \times 10^{-5}$ to 8.3×10^{-1} rps, for filling heights $H/R_s = 0.5$, 0.7 and 1.0. In a single experimental run, we vary Ω from low to high. We average the torque for each individual Ω over at least half a rotation or at least 10 seconds; many runs are averaged over much larger strains. Note that we did not employ temperature control in these experiments; however the laboratory temperature was constant to within 1 degree around 26 °C.

In Fig. 5.3a we plot the average driving torque as a function of Ω. The phenomenology is as in Fig. 5.1a. Adding water and zinc chloride to the Triton can affect its viscosity, which would produce a horizontal shift of the data -- we see no substantial shift in the data however. A small vertical shift is observed however: the plateau value for the $H/R_s = 0.5$ set is at 0.55 ± 0.05 mNm, but for the pure Triton/PMMA suspension it is at 1 ± 0.1 mNm. This can be (partly) explained by noting that the buoyancy corrected density of the PMMA particles in the index matched suspension is much closer to density matching than in the pure Triton fluid, due to the presence of $ZnCl_2$: the density of PMMA is 1.18
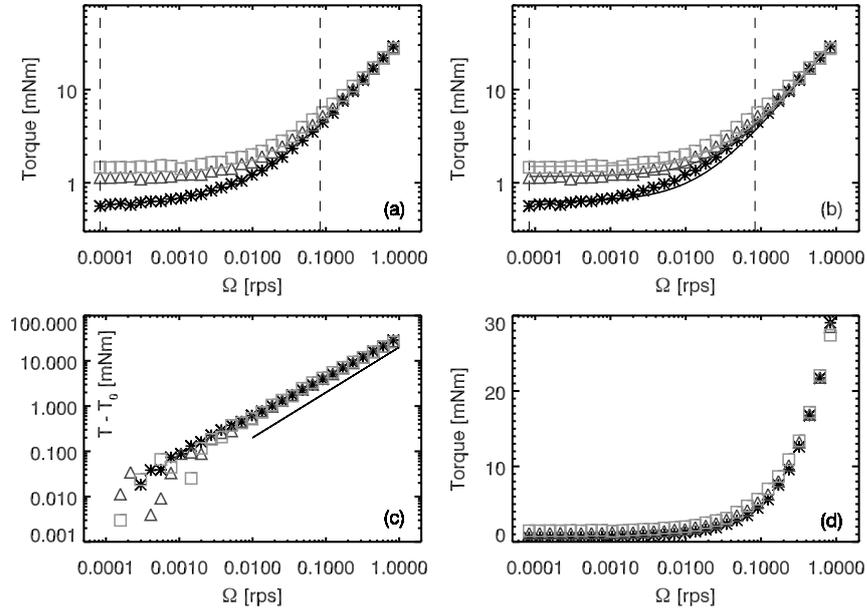
Figure 5.3: $T(\Omega)$ for three different filling heights. H/R_s: $= 0.5$, $\triangle = 0.7$, $\square = 1.0$. (a,b) show the average torque as a function of driving rate. The dashed lines in (a,b) show in which regime of rotation rates the velocity profiles were also measured as described in chapter 3. (b) Shows includes a fit of the form $T = T_0 + C\Omega$ -- see text. in (c) we subtracted the low Ω limit plateau values from the data. The line has slope one. (d) shows the same data as a, but with linear scaling on the ordinate.

kg/m^3, and the density of Triton is 1.08 $\times 10^3$ kg/m^3. Adding 13 weight % of zinc chloride and some water will make the fluid and particle densities come closer. A lower density reduces the normal forces and therefore the frictional forces between the particles.

The fit to Eq.5.2 also works as well for this type of suspension: Fig. 5.3b shows these fits.

In the current suspension experiments, we probe the rheology over a larger range of rotation rates than was done in Fig. 5.1a. This allows us to look in more detail at both the high and low rotation rate regime in more detail.

Small Ω limit -- To examine the exponent of the rate dependent contribution to the torques, $T \sim \Omega^n$ more closely, we plot $T(H, \Omega) - T_0(H)$ for the three filling

heights on double logarithmic scale in Fig. 5.3c. We see now that the suspension does not satisfy $T \sim \Omega$ - behavior: the exponent is slightly smaller than one.

This deviation from Newtonian behavior can at least partly be explained by noting that $\dot{\gamma}$ is not strictly proportional to Ω: the width of the flow profile changes significantly with the driving rate, as was shown in section 3.4. Specifically, we observed that the velocity profiles broaden with Ω, and this broadening of the velocity profiles reduces $\dot{\gamma}$, which gives rise to the sublinear behavior as observed in Fig. 5.3c.

Large Ω limit -- Deep into the rate dependent regime, around driving rates of 0.5 rps, we had observed a profound change in the surface structure of the suspension, as evidenced in section 4.3.2. Interestingly, the rheology in that regime of driving rates does not show any noticeable features at those rotation rates; the power law behavior shown in Fig. 5.3 continues all the way up to 1 rps.

5.4.2   Particle Size Effect
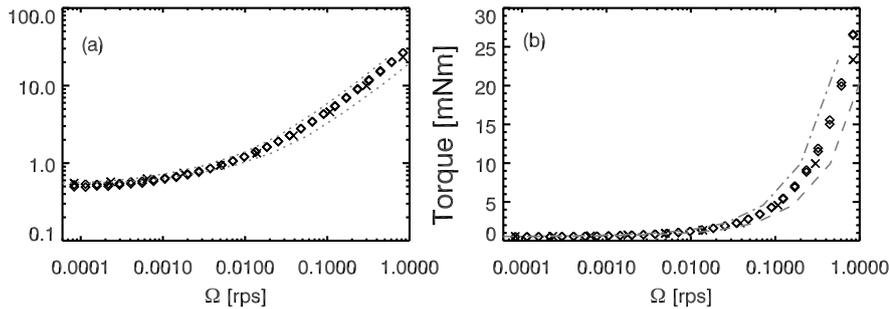
Figure 5.4: (a,b) $T(\Omega)$ of the two different suspensions. Symbols: $\diamond$ = 3 mm PMMA particles, $\times$ = 4.6 mm PMMA particles. In (b) the grey lines show the data for the 4.6 mm particles, plotted versus Ωd (dashed line), and Ω/d (dash-dotted line).

The inertial number for submersed granular flow $I = \dot{\gamma}P/a\eta$ is independent of particle size. However, in section 4.3.1 it was shown that the flow profiles for 4.6 and 3.2 mm particle size suspensions show a substantially different onset of the rate dependent regime. Therefore we measure the rheology of a Triton/PMMA based suspension with 3.2 mm particles, and compare it to the rheology of the 4.6 mm particle suspension as measured in section 5.4.1. We repeat the same rheological protocol as used for the 4.6 mm particle suspensions for one filling height. We use H/R_s = 0.5, at the filling height the rate dependence is strong.

Fig. 5.4a,b show the rheology for the 3.2 and 4.6 mm particle suspensions. The data sets are indistinguishable from each other. Considering the error in the repeatability of the experiment, we cannot rule out that the excellent match shown is simply fortuitous. However, we can conclude that the huge shift in the onset of rate dependence observed in section 4.3.1 is certainly larger than the uncertainty in this measurement. This substantiates the claim made in section 4.3.1 that the shift in rate dependence observed is most likely experimental in nature, due to the fact that the experiments were done two different setups, with different suspension compositions.

We also plot the data for the 4.6 mm particles with rescaled values for Ω: Ωd (dashed line) and Ω/d (dash-dotted line). The shift that this rescaling of the rotation rate produces is too small to exclude a particle diameter effect.

5.5   Suspension Rheology: Effective Viscosity
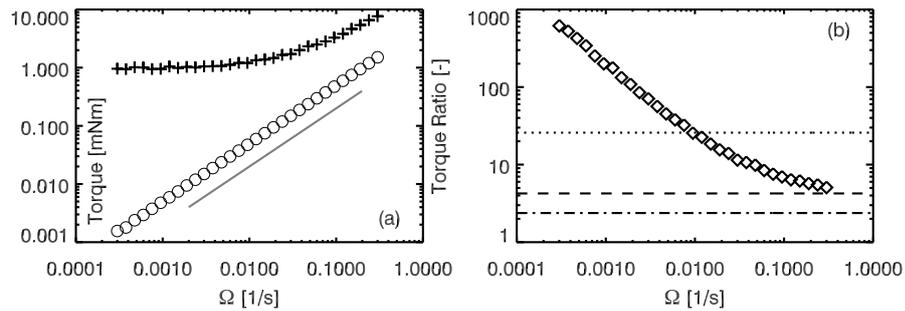
Figure 5.5: (a) Average driving torque as a function of driving rate for a Triton/PMMA suspension (+), and a layer of pure Triton (○). The grey line has slope 1. In (b), we show the ratio between the two data sets shown in (a), the ratio of their viscosities. For a concentration of $\Phi = 55\%$, we plot the ratios predicted by Einstein (dash-dot), Batchelor (dashed) and Krieger-Dougherty (dotted).

Particle laden fluids have a higher viscosity than the fluid itself. We expect to see this effect also in the rheology of split-bottom flows.

It was famously shown by Einstein in 1906 that for small concentrations, the effective viscosity of a particle laden suspension is

$$\eta_S = \eta_f(1 + 2.5\Phi), \tag{5.3}$$

where η_S and η_f are the suspension and pure fluid viscosity respectively, and Φ is the concentration of particles suspended in the fluid. This expression holds or Φ

up to 5%. For larger concentrations, the prefactor for the second order correction Φ^2 was calculated by Batchelor in a now classic paper [86]. For concentrations up to 20% (see Ref. [87] and references therein), it was shown that

$$\eta_S = \eta_f(1 + 2.5\Phi + 6.2\Phi^2).$$ (5.4)

For highly concentrated suspensions, several analytical approximate equations have been put forward, but none seem to work in all cases. However, there is a phenomenological equation put forward by Krieger and Dougherty [83] in 1953 that is now widely used for particle concentrations up to the random close packing limit $\Phi_{rcp} \sim 63\%$, where any packing of hard spheres acquires a finite yield stress [21], and cannot be viewed as a liquid anymore:

$$\eta_S = \eta_f(1 - \frac{\Phi}{\Phi_{rcp}})^{-2.5\Phi_{rcp}}.$$ (5.5)

In this equation, the factor of 2.5 in the exponent is sometimes allowed to vary freely, but it is usually set to 2.5 to make the equation compatible with the Einstein result at low concentrations.

We can measure the effective viscosity correction factor also in the split-bottom geometry. Even though we do not have access to the stresses and strain rates applied, we can compare the ratio η_S/η_f in the split-bottom flows, by measuring the driving torque for both pure fluid and the suspension as a function of Ω. We look at this ratio for a 4.6 mm PMMA particles suspended in pure Triton to a filling height of $H/R_s = 0.5$, and a fluid layer of pure Triton X-100 of the same height. We plot the experimental results in Fig. 5.5a. We observe that the Triton is fully Newtonian, since the slope of the experimental data is indistinguishable from 1 (grey line). This is expected at these temperatures (25°C) -- see appendix 5.7.2.

In Fig. 5.5b, the ratio of the suspension and pure fluid is shown. We see that in the regime where only viscous forces should play a role, the torque, or equivalently the viscosity ratio, is far below the value predicted by the Krieger-Dougherty law for a particle concentration of 55%, a value commonly observed at these flow rates. In order to be consistent with Krieger-Dougherty, the concentration in the particle suspension should be around 37%, far below concentrations that have been observed at these driving rates -- see section 1.5.1. We have no explanation for this.

5.6   Conclusions

We have seen that Eq. 5.2 is a reasonable fit for the rheology of suspension flows in the split-bottom. The timescale that set the rate dependence in the flow profiles of suspensions seems to be similar to the timescale that sets this process in their rheology.

We use the rate independent properties of suspensions to show that Triton X-100 does not lubricate PMMA-PMMA contacts; the effective friction coefficient for PMMA particles submerged in Triton is the same or slightly larger as for dry PMMA contacts.

We find that the effective viscosity of a highly concentrated suspension measured in the split-bottom geometry is anomalously low compared to common phenomenological laws as the Krieger-Dougherty law.

5.7   Appendices

5.7.1   A: Transients in Suspension Rheology

To measure the average driving torques in suspensions, one has to be in steady state flow situation. There are however transients observable in the driving torques, which we show here.

We measure the evolution of the driving torque in a typical 3.2 mm PMMA/triton based suspension, with H/R_s of 0.38, as we suddenly apply a rotation rate of 0.18 rps, starting from rest. The rotation rate is changed after 100 seconds to 0.018 rps (Fig. 5.6a). The time dependence of the driving torques is shown in Fig. 5.6b. Only a short transient of about 10-20 seconds is observed for both starting up and after the sudden reduction of rotation rates. After an increase of speed, an overshoot is observed, after a decrease the torque is temporarily lower than the asymptotic behavior.

The transients shown in Fig. 5.6a,b affect a typical rheological experiment in which the rotation rate is sweeped up and down. In Fig. 5.6c we plot the results of such an experiment for a 4.6 mm particle based suspension with $H/R_s = 0.7$. For the higher Ω, we average over a strain of at least 4 rotations, but that implies that the amount of time we average over is still less than 10 seconds. This amount of time is not enough to get out of the transient dip in torques that follows typically after a reduction of speed, and therefore leads to a systematic underestimation of the driving torques in the downward ramp.

Other, much longer transients have been observed in density matched suspension flows, for example due to shear-induced migration [88]. However,
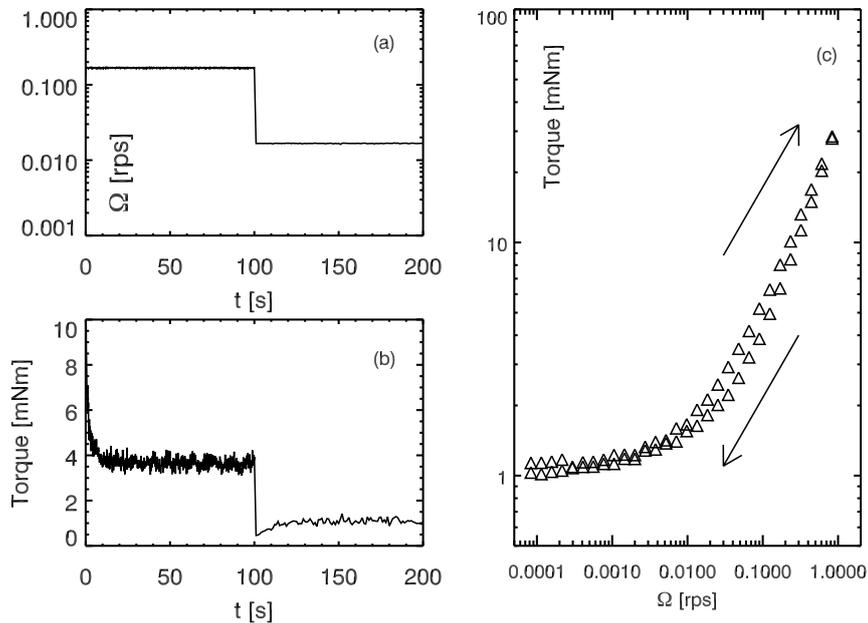
Figure 5.6: The rotation rate (a) and the driving torque (b) are plotted for an experiment on 3.2 mm PMMA particles in a Triton based fluid, with $H/R_s = 0.38$. During the experiment Ω is first increased from 0 to 0.18 rps. After 100 seconds it is changed abruptly to 0.018 rps. (c) Shows $T(\Omega)$ of an experiment in which Ω was ramped up and down. For this experiment, 4.6 mm PMMA particles in a Triton mixture were used; $H/R_s = 0.7$ in this experiment.

in our gravitational suspensions, if we keep the driving rate constant, we do not observe any drift in the torque even after 600 seconds (not shown). We therefore suspect that the settling of the particles in our suspension suppresses all other transient effect observed in density matched suspensions.

5.7.2   B: The Low-Temperature Properties of Triton X-100

[1]Triton X-100 is a polymeric fluid, and has non-Newtonian properties at reduced temperatures. Triton X-100 is specified to 'freeze' below $\sim$ 18 degrees Celsius, and shows a glass transition around 5°C. In this appendix we show that in the range of the temperatures used in our experiments, the behavior of Triton X-100

---

[1]Many thanks to Matthias Möbius for help with the rheological experiments described in this appendix.
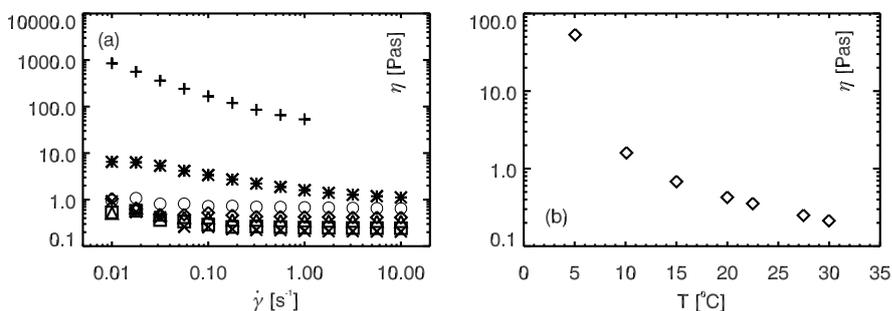
Figure 5.7: (a) The viscosity of pure Triton X-100 as a function of shear rate and temperature. Different symbols indicate different temperature: $+ = 5$, $* = 10$, $\circ = 15$, $\diamond = 20$, $\triangle = 22.5$, $\square = 27.5$, $\times = 30$ °C. (b) shows $\eta(T)$ for $\dot{\gamma} = 1.0$.

is fully Newtonian, for strain rates between 10 and $10^{-2} [s_{-1}]$.

To show this, we measure the viscosity of pure Triton X-100 in a narrow gap Couette geometry over a temperature range of 5 - 30°C. We use a rheometer (Anton Paar MCR 501) with a standard narrow gap Couette geometry (Anton Paar CC20) in a liquid nitrogen cooled temperature chamber (Anton Paar CTD 450). The results of the experiment are plotted in Fig. 5.7. In Fig. 5.7a we see that at low temperature the viscosity of the polymer fluid depends strongly on the strain rate $\dot{\gamma}$ -- note the logarithmic scale on the ordinate. However, for temperatures above 20°C the viscosity of the fluid appears to be rather independent of the strain rate. The typical strain rate in our experiments can be estimated to be $2\pi\Omega R_s/W$, where $W \sim 1$ cm is the typical width of the shearband. In the rate dependent regime, where viscous effects are most pronounced, $\Omega > 0.01$, which gives $\dot{\gamma} > 0.3$ -- in this regime the behavior is Newtonian.

The overall viscosity of the Triton does however still depend on the temperature; the viscosity at $\dot{\gamma} = 1$ is shown in Fig. 5.7b.

Mixing Triton with water can have a surprising effect on the rheology of the mixture; for small amounts, adding water alone for example *increases* the viscosity of the Triton/water mixture [89][2], and at 25° and 50% even a gel point is reached. The rheological behavior of Triton X-100 with water added is not further investigated.

---

[2]Ref. [89] says: *"Increased viscosity and gel formation at concentrations around 50 percent are probably due to interference with the flow that results from hydration of the oxyethylene ether linkages in the aggregates.*

Chapter 6

Agitated Granular Flows

6.1 Introduction

Granular materials exposed to small agitations loose their macroscopic rigidity: the appearance of fluctuating interparticle forces makes rearrangements and flow possible, even at very small stresses [7, 90]. Also in very slowly driven flows and far away from the source of driving one observes sudden particle rearrangements and flow, driven by the force fluctuations due to such agitations [43] -- they have a long range. However, flow itself also induces such agitations [91]. This makes it hard to disentangle the role of the fluctuations on granular flows.

The role of agitations is hard to underestimate. Due to the long range influence of these force fluctuations, they are for example believed to be the main ingredient of non-local extensions for the rheologies of granular flows [?, 2, 38, 51], which should for example explain the broad shearbands in split-bottom flows. Their role is however more broadly appreciated: it is also precisely this macroscopic mechanical sensitivity to microscopic fluctuations that is at the basis of recent models for slowly flowing disordered materials: it comes back in various guises in STZ [92], SGR [93], and the fluidity model from Bocquet [94].

To study the role of agitations on flow of granular media, piezo transducers have been used to inject tiny rearrangements or force fluctuations, either locally [7, 95] or along a complete boundary [96]. Horizontal vibrations have been used to induce flow on inclined planes [90, 97]. The relaxation of the slope of a granular pile has been studied in rotating drums with vertical vibrations [98].

The yield stress of a granular material has been shown to disappear in the presence of flow [99]. However, no experiment to date has been able to combine control over the flow with control over the agitations.

In this chapter we probe for the first time the role of agitations on the continuous flow properties of granular materials. We are able to control the strength of the agitations, and combine this with accurate flow control. We study how the externally applied yet very weak vibrations affect the rheology of granular flows, by performing two kinds of rheological experiments: constant shear rate, in which we measure the torque necessary to sustain a flow rate, and constant shear stress experiments, in which we measure the flow rate under constant stress. In the experiments, the dimensionless vibration amplitude $\Gamma = A\omega^2/g$, in which A is the vibration amplitude and ω the frequency, is always smaller than one.

Independently of the shape of the shearbands, set by the filling height, we see essentially the same behavior: weak vibrations destroy one of the hallmarks of slow granular flows: rate independence. Even a very small amount of vibrations, at $\Gamma \simeq 0.1$, makes granular flows rate dependent at all driving rates.

Moreover, stresses far below the yield stress can induce flow when vibrations are present. We find that after an initial transient, under constant stress also steady state flow can occur, even for stresses below the macroscopic yield stress.

For small Γ and T, we also find a regime of glassy flow, where the transient creep does not cease after 10^7 vibration cycles. This regime connects smoothly to the slow steady flow regime, which suggests that even for very small agitations, flow always remains possible.

6.2   Setup

Split-bottom cell and particles -- We study weakly vibrated granular flows in a split-bottom setup. We use here the *disk* version introduced in section 2.5.1: the rough disk is positioned directly above a hollow smooth cylinder of 6 mm height, such that no particles can get underneath the disk. The disk measures 4 cm in radius, and the acrylic container has a radius of 7 cm. The disk is made rough by gluing particles to it. We use black soda-lime glass beads (Sigmund Lindner 4504-007-L), a polydisperse mixture with a diameter range from 1 to 1.3 mm, and a bulk density ρ of 2.85 $\times 10^3$ kg/m³. The filling heights we use are H/R_s = 0.33 and 0.7, for which we know the shearbands take the form of a trumpet and a dome respectively (section 1.4).

All experiments are carried out under ambient temperature, pressure and relative humidity. We have verified that the experiments we carry out are

insensitive to humidity, in the window of relative humidities between 6 and 55%.
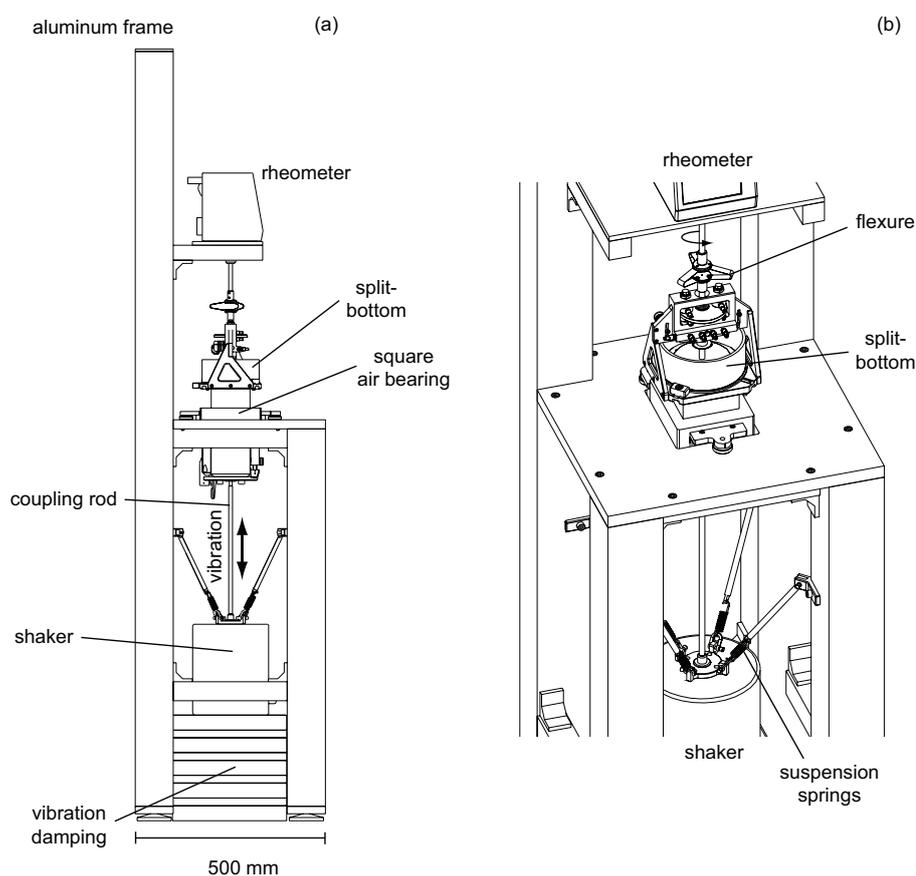
Figure 6.1: The setup used in the vibro-rheology experiments. (a) A schematic picture of the side-view of the setup. (b) A top view of the split-bottom cell on the air bearing, with the shaker beneath it.

Inducing Weak Vibrations -- The split-bottom cell is mounted on the slider of a square air-bearing (4"x4", New Way). The air bearing is used to ensure that the slider and the container move virtually friction free in the vertical direction, and the movement in the horizontal plane has only submicron amplitudes due to the stiffness of the air bearing. The air-bearing can be vertically aligned with set screws. This helps aligning the disk axle with the rheometer axle. The effect

of heaping, the tilting of the surface of granular media subjected to vibrations [100], is not strong enough to affect our measurements, since we use only small amplitude vibrations.

We induce vibrations in the split-bottom cell with an electromagnetic shaker shaker (VTS systems VG100), driven by a function generator (Thurlby Thandar TG1010) via a commercial audio amplifier (Crown CE1000). The total combined weight of the slider and the split-bottom cell is approximately 12 kg and therefore too large to be carried by the shaker alone. Therefore we support their weight with four suspension springs with a stiffness of 2 kN/m, connected to the aluminum frame shown in Fig. 6.1b.

The shaker axis and air-bearing axis cannot be perfectly aligned. A 40 cm long and flexible aluminum rod therefore couples the tube and the shaker. The aluminum rod is flexible enough to compensate for the alignment mismatch of a few millimeter, but stiff enough to ensure a strong mechanical coupling between shaker and air-bearing slider (see Fig. 6.1a).

The vertical acceleration of the split-bottom cell is measured by a combination of two accelerometers (Dytran E3120AK and a modified ADXL322EB[1]). We only use continuous sinusoidal vibrations, so we use a lock-in amplifier (SRS 830) to achieve a measurement accuracy of the vibration amplitude of $< 10^{-3}\ g$. The harmonic distortion of the sinusoidal motion is about 1%.

We employ a LabVIEW driven feedback scheme that keeps the vibration amplitude constant during the experiments to within $< 10^{-3}\ g$. This is necessary since the shaker generates considerable heat, which affects its operation; without feedback the vibration amplitude slowly drifts over 0.1 g per hour.

To limit the mechanical coupling between the table and the shaker, the shaker is placed on a stack of concrete tiles with rubber mats sandwiched between them.

We measure the mechanical response of the whole setup to find the dominant mechanical resonance frequencies -- see section 6.7.1. In the window 50-75 Hz we find no mechanical resonances, and choose 63 Hz as vibration frequency f. The vertical vibration amplitude at a peak acceleration of 1 g at this frequency is 64 micron.

Combining shear and vibration -- As discussed in the introduction, we want to ensure that the disk only induces rotational shear deformations. We therefore make sure that the disk comoves with the reference frame of the container -- there should be no relative vertical motion between the disk and the container. This is done by combining a strong vertical coupling of the

---

[1]Its factory default bandwidth of 50 Hz is increased to 2 kHz.
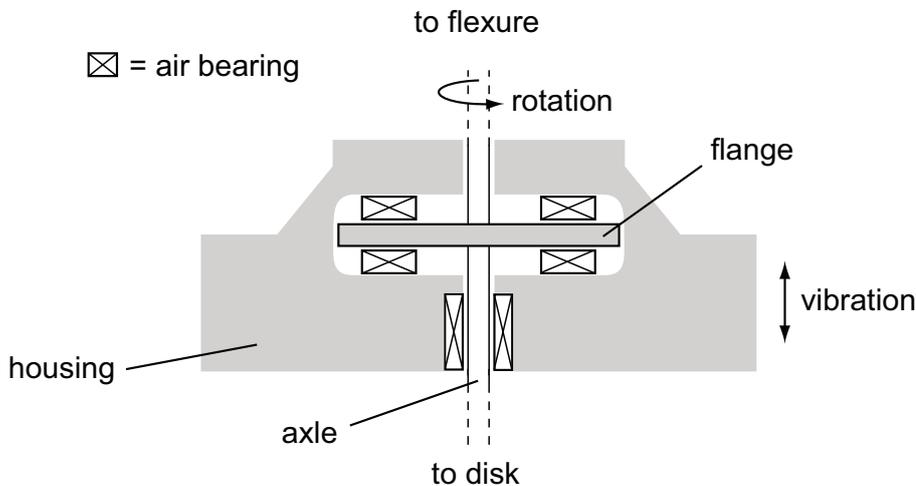
Figure 6.2: Schematic drawing of the custom-built air-bearing assembly that fixes the disk axle in the vibrating reference frame of the container. The flange is held in place by four flat bearings, the axle is fixed by a round bearing.

mechanical motion of the disk with the ability to rotate freely, in the following way: The rotating disk rotates on an axle that is mounted in a cylindrical air bearing ($\varnothing$ 1/4", New Way). Rotational motion is therefore friction-free. We attach a *flange* to the axle. The surface of the flange is polished, and clamped between four flat air bearings ($\varnothing$ 25 mm, New Way). By mounting the flat air-bearing assembly on the container, we ensure that disk and container move together during the vibration cycle: the stiffness of one flat bearing, for a typical gap between the bearing and the flange of 5 micron [101], is 18 N/μm. Since the peak acceleration of the system is never larger than $\sim$ 1.5 g, and the weight of the flange/axle/disk construction is less than a kilogram, the maximum residual motion between the disk and the container is much smaller than a micrometer, which is the typical lengthscale of asperities on glass beads [102].

The flat bearings cannot be positioned perfectly parallel to the flange. This induces an asymmetry in the air flow between the bearings and the flange. This exerts a torque of order of 10 μNm on the flange, which is about 1% of the smallest torques we apply -- see appendix 6.7.1.

Coupling the split-bottom cell to a rheometer -- We drive the disk with a rheometer (Anton Paar DSR 301). The rheometer cannot be vibrated, so it cannot be mounted directly onto the vibrating container. Coupling the disk
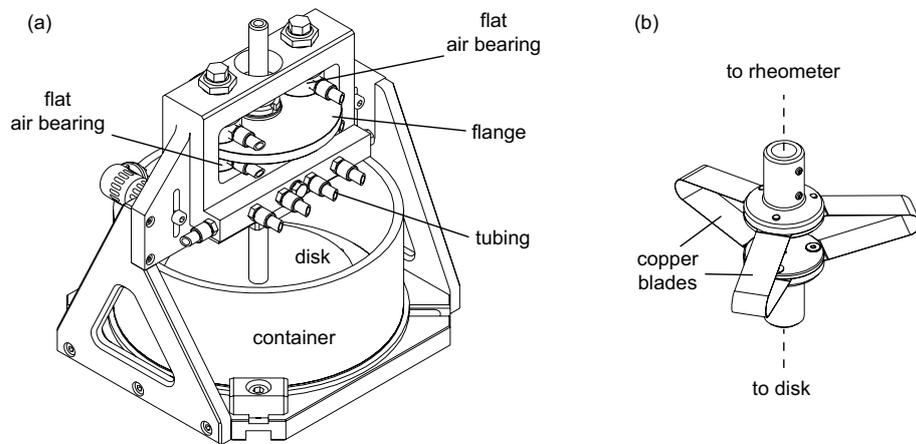
Figure 6.3: (a) The split-bottom cell, with the flat air-bearing assembly (see text). The four flat bearing that clamp the flange and fix it rigidly to the container, are mounted on a bridge over the container itself. In the bridge also the round bearing is mounted that holds the axis for the disk. Tubing for compressed air is not shown. (b) The flexure coupling the rheometer axis to the disk axle. The copper blades measure 0.3 mm in thickness and 7 mm in width.

axle to the rheometer axle is therefore problematic: They are both suspended by very stiff air-bearings that cannot be perfectly aligned, and the disk axle is moving vertically. We solve this by coupling the two axes with a flexure, shown in Fig. 6.3b. It has a torsional spring constant of 4 Nm/rad. The flexure can be compressed easily and therefore accommodate the vertical motion of the disk axle; it's compressional spring constant is 5×10^2 N/m. The copper blades used in the flexure are flexible enough to couple the misaligned axis of the disk and the rheometer, without exerting too large forces on the bearings.

Misalignment between the disk and rheometer axle causes variations with rotational periodicity in the force that the rheometer exerts on the disk and grains. This periodic modulation of the torque can be reduced by improving the alignment of the flexure-coupled axles; the amplitude of the variation can be reduced to less than 20 μNm, which is 2% of the smallest torque we have to measure -- see appendix 6.7.1.

Constant Ω experiments -- The rheometer model we use, the DSR 301, is a stress driven rheometer, so its native mode is to set a torque to control rotation. However, it is also possible to use the rheometer in a so-called constant

shear rate mode. In this mode, the rheometer applies a feedback routine that dynamically adjusts the torque it applies in order to achieve a constant rotation rate. This process has one control parameter: the rate at which the torque is increased or decreased. This timescale is set by the desired driving rate, and by a user-defined time constant, and in principle could affect all constant shear rate experiments.

In all constant shear rate experiments we set the feedback constant such that we observe smooth rotation, this is achieved for a feedback parameter value of 25%[2]. If the torque adaptation rate is too high and becomes of the order of the eigenfrequency of the rheometer axle, the feedback routine will be affected by the rotational eigenmodes of the mass-spring system of the rheometer axle. If the torque is ramped with less than about 1 mNm per second, the flow becomes intermittent; the material then fails in a stick-slip fashion.

6.2.1 Pre-Shear Protocol

Before each experiment, unless noted differently, we apply an amount of pre-shear to the granular material, in order to obtain similar starting conditions for each experiment. The protocol consists of the following amount of shear: *(i)* 10 seconds of 40 rpm rotation clockwise; *(ii)* 20 seconds of 40 rpm rotation counter-clockwise; *(iii)* 10 seconds of 40 rpm rotation clockwise.

After this pre-shear, we wait for 5 seconds before starting the experiment in the clockwise direction. During the pre-shear and also the wait time, the vibrations are turned on, since the feedback loop that controls the vibration needs some time to reach equilibrium, and cannot be started instantaneously. Therefore the waiting time after the pre-shear is not entirely irrelevant -- see appendix 6.5.1.

6.2.2 Yield Torque

In the absence of vibrations, granular materials have a yield stress: a finite amount of force is needed to induce deformation. In the split-bottom setup, this means that we have to apply a finite amount of torque or *yield torque* T_Y to the disk to make the granular materials flow at $\Gamma = 0$. This definition of T_Y is problematic however: the threshold depends on the way the experiment is carried out, and in particular depends on the history of the material: after exposing granular materials to vibrations, or oscillatory shear, the yield torque T_Y can be significantly higher than directly after pre-shear.

---

[2]This is the so-called CSR-value of the rheometer.

To determine a yield torque, we use the following rheometric protocol at $\Gamma = 0$: we ramp up the torque from a low non-zero torque value with 0.5 mNm per second. At a certain moment the material fails under the applied torque; at that point the rotation rate increases dramatically within a very narrow torque interval. In this sharply rising part of $\Omega(T)$, we look at $\Omega(T) = 0.4$ rps; that T sets the yield torque. We then repeat the torque ramp, without applying pre-shear.

This method yields an average yield torque of about 13 mNm for $H/R_s = 0.33$, and 34 mNm for $H/R_s = 0.7$. The yield torque displays a mean drift of about 1 mNm per month, also depending on how many experiments are done. This is probably due to erosion of the bead surface -- we always use the same set of particles. The yield torque also displays run-to-run variation, discussed below.
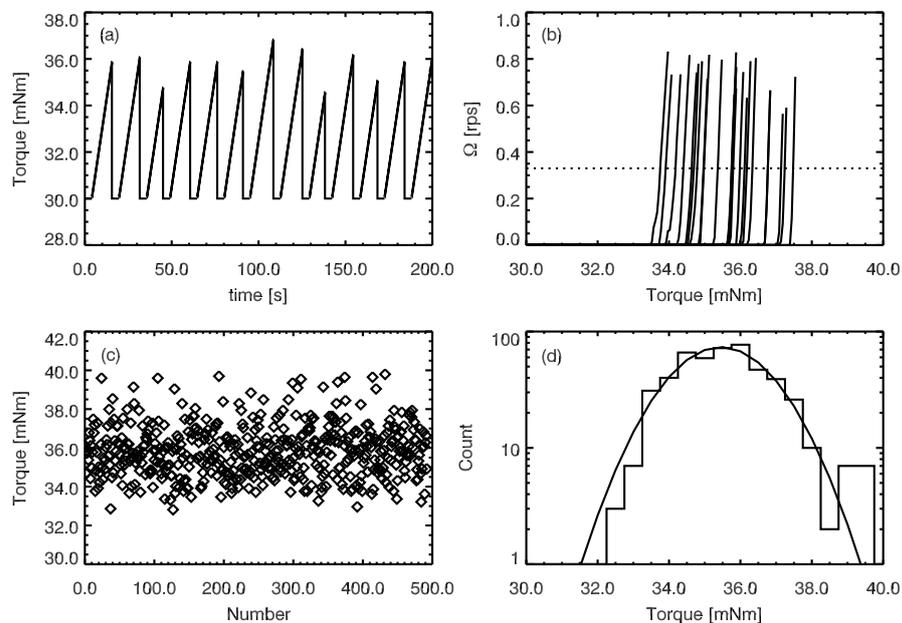
Figure 6.4: (a) The torque values applied during the yield stress measurement. At the peak torque value, $\Omega = 50$ rpm. (b) $\Omega(T)$ for all the torque ramps. The dotted line is where the Ω-cutoff to determine the yield torque. (c) The yield torque as a function of run number. (d) the histogram of the distribution of yield torques, with a Gaussian fit.

Yield torque: statistics -- We measure how much the yield torque varies from run to run, by looping the following protocol after applying pre-shear. We

116

do this for $H/R_s = 0.7$.

(i) Ramp the torque at 0.5 mNm per sec, starting from 30 mNm. At some point the materials fails and the rotation rate increases rapidly. *(ii)* when $\Omega > 50$ rpm, lower the torque immediately back to to 30 mNm, and keep that value for two seconds. This stops the flow and return to a completely quiescent state. Then start again at *(i)*.

We repeat this protocol 489 times. An example of how the the torque as a function of time develops is shown in Fig. 6.4a. In this figure, the peaks of the torque ramps end at different heights, since the ramp is stopped when Ω has reached 50 rpm, which happens at different T for different runs. We plot the individual $\Omega(T)$ curves in Fig. 6.4b. Each individual spike in the plot corresponds to the sharp increase in the rotation rate after materials failure. We determine the yield stress for each run at $\Omega(T) = 0.4$ rps. This gives 489 values of the yield torque. We plot the obtained yield torque as a function of run number in Fig. 6.4c; no trend is observable. The distribution of yield torques around the mean is broad, about 10%. The histogram of torques values is shown in Fig. 6.4d. The distribution is skewed: the Gaussian fit clearly misses the excess of data at the higher T-range, and overestimates the amount of data left of the peak.

6.3   Constant Ω Experiments

In this section we look at how weak vibrations affect the rheology of granular flows, when their deformation rate is imposed. Thus, we use the rheometer in the constant shear rate mode. This allows us to study the role of the vibration-induced fluctuations at any flow rate.

For non-vibrated, slowly flowing hard granular materials, the driving torque at set flow rate is independent of the flow rate [10]: only rate-independent frictional interactions play a role. Softer granular materials show logarithmic rate dependence when compressed [5]. Adding vibrations to these flows changes this picture completely. Furthermore, we will see that two additional flow phases appear, due to the presence of the vibrations.

6.3.1   Steady State Shear

We verify first that a steady state flow rate can be obtained by the rheometer. To do this, we measure the instantaneous driving torque and speed as a function of time for different set speeds and vibration amplitudes. We apply pre-shear before the start of the experiment, and start a logarithmic ramp down in set speeds, from 5×10^{-1} to 5×10^{-5} rps with 2 steps per decade. We measure for all
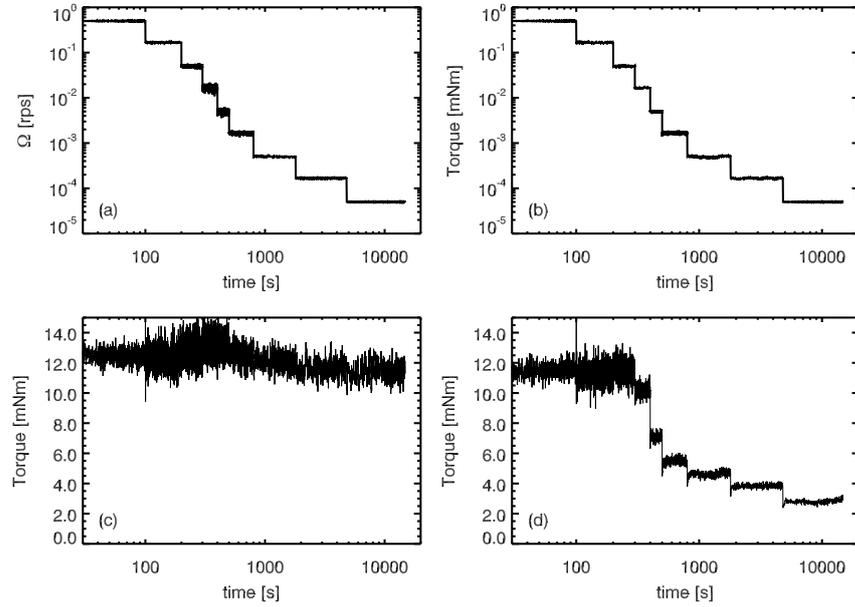
Figure 6.5: Rotation rate (a,b) and driving torque (c,d) shown as a function of time for an experiment in which the set speed is reduced logarithmically. (a,c) are measured for $\Gamma = 0.2$, (b,d) are measured for $\Gamma = 0.8$. Both experiments are carried out at $H/R_s = 0.33$.

set speeds over a strain of 0.5 rotation[3], with a sample rate of 10 Hz. The results for $H/R_s = 0.33$ are shown in Fig. 6.5.

We show for $\Gamma = 0.2$ (a,c) and for $\Gamma = 0.8$ (b,d) both the instantaneous speed of the disk (a,b) and the driving torque (c,d) as a function of time. Note the logarithmic scale on the time axis. We see that for $\Gamma = 0.2$, the set speeds are achieved very accurately and no large fluctuations or transients are observable. The fluctuations in the torque signal are however appreciable. Only a small transient is observable, even for the slowest run, which spans over 3 hours. For $\Gamma = 0.8$, the fluctuations in both speed and torque are strongly reduced and we can clearly see that no long time transients are present in these experiments.

The absence of any long-time transients means that the mean driving torque T and mean rotation rate Ω are well defined quantities. We proceed by looking

---

[3]If the set speed is such that this amount of strain is achieved within 10 seconds, we set the shearing time to 10 seconds for inertial transients to die out.

in detail how these are related at different vibration strengths Γ: we will thus probe $T(\Gamma, \Omega)$.

6.3.2   Breakdown of Rate Independence
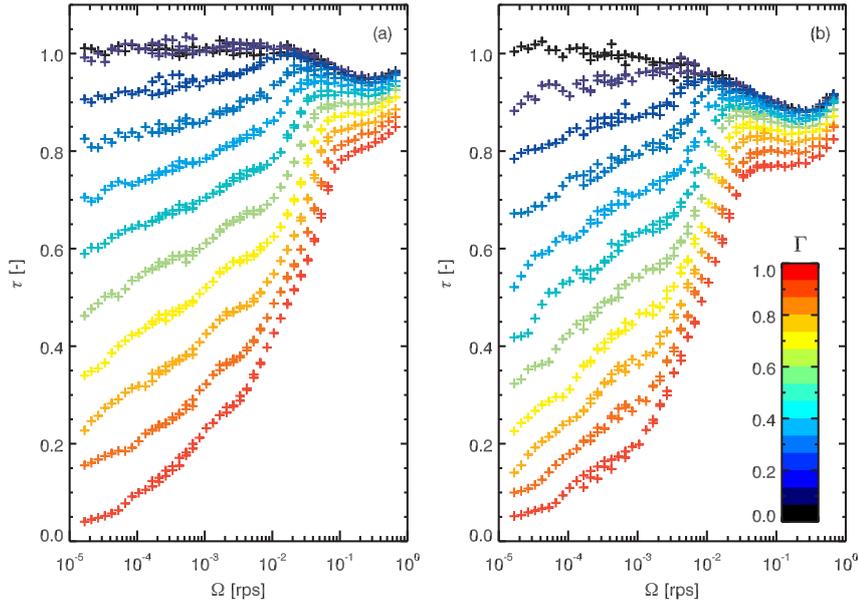
Figure 6.6: (a) $\tau = T/T_Y$ versus Ω for $H/R_s = 0.7$. (b) $\tau(\Omega)$ for $H/R_s = 0.33$. $\Gamma = 0,0.1,0.2,...,1$ (black-red).)

To obtain $T(\Gamma, \Omega)$, we measure the average steady state torque T necessary to sustain a certain rotation rate Ω. We apply vibration strengths Γ between 0 and 1, and the range of rotation rates probed is 1.6×10^{-5} to 1 rps. We measure at two different H/R_s: 0.33 and 0.7; below and above the transition to dome flow (see section1.4.3).

In Fig. 6.6a we plot for $H/R_s = 0.33$ the average normalized torque $T/T_Y = \tau$ versus the rotation rate Ω, for Γ between 0 and 1. Several things can be observed: $T(\Gamma, \Omega)$ is qualitatively very similar for the two different filling heights, and therefore we can conclude it is insensitive to the flow structure. For $\Gamma = 0$, we see rate independence at low Ω, consistent with our observations in chapter 2. For faster flows, with $\Omega \sim 0.01$ rps, we see a small reduction in the driving torques.

119

At $\Gamma > 0$ we see rate dependence at all driving rates. The rate dependence is roughly logarithmic at low driving rates, and displays a sharp increase around $\Omega \sim 5 \times 10^{-3}$ rps. For $\Gamma \to 1$, the driving torque almost entirely disappears at low driving rates. For small Γ and $\Omega \sim 0.5$ rps, the driving torque drops with increased Ω; this mechanical instability, only visible since we control the rotation rate, disappears at larger vibration amplitudes.

Influence of H/R_s **--** The filling height affects the $T(\Gamma, \Omega)$ quantitatively: the rate dependence at $\Gamma = 0.1$ is more pronounced for $H/R_s = 0.33$. We also see that the instability around $\Omega \sim 0.01$ rps disappears at $\Gamma \sim 0.6$ for $H/R_s = 0.7$, but only at $\Gamma = 1$ for the smaller filling height. Furthermore, the slope change of $T(\Gamma, \Omega)$ around $\Omega \sim 5 \times 10^{-3}$ rps is more pronounced for the smaller filling height, and slope $d\tau/d\Omega$ in the logarithmic rate dependent regime for $\Omega \lesssim \sim 5 \times 10^{-3}$ rps is less sensitive to Γ at that same $H/R_s = 0.33$. We will show data for Data for $H/R_s = 0.33$ unless otherwise stated.

6.4   Constant Torque Experiments

Non-vibrated granular materials have a yield stress, which means that no flow occurs for applied stresses below a certain threshold; this is why a heap of sand is stable. This threshold stress roughly corresponds to the average driving torque plateau at small Ω in the constant flow rate experiments. We have seen that vibrations lower this threshold, and even make it rate dependent. Will vibrations also affect the flow behavior if we drive the disk at constant applied torque? Perhaps the weak vibrations will make flow possible, even for very small amounts of imposed torques?

To study this, we drive the flow with the so-called constant *shear stress* mode of the rheometer. In this mode, the rheometer applies a constant torque to the disk.

Constant torque experiments have two advantages over constant Ω experiments. In the latter, the rheometer modulates the torque to keep Ω constant. It is not clear how these modulations affect the flow. Moreover, these torque fluctuations also make it impossible to recover the rotational angle of the disk: we can only record the motion of the rheometer axle, which is connected via a flexure to the disk. For constant torque experiments, fluctuations in the torque are *per definition* absent, and the rotational angle of the disk is easily recovered, since the torque applied to the disk via the flexure, only gives rise to a constant offset in the measured rotational angle.

In this section we discuss such constant torque experiments. A typical

experiment consists of the following protocol: after pre-shearing the sample, a certain amount of torque T is applied, and the ensuing rotation angle φ of the disk is monitored. We will show that applying constant Ω or applying constant torque gives essentially the same flow behavior. We will also see that depending on the control parameters $\tau = T/T_Y$ and Γ we observe three distinctly different types of flow.

6.4.1 Phase Diagram
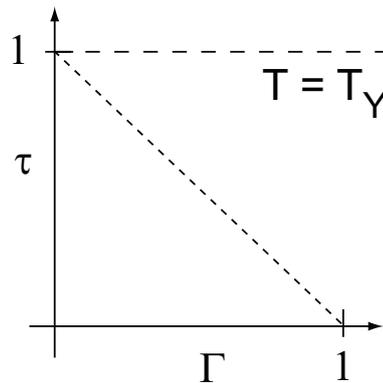
Figure 6.7: A sketch of the phase diagram, with the expected phase boundaries. Long dash: the yield stress boundary extended from $\Gamma = 0$. Short dash: the phase boundary where periodic modulations in which $T \geq T_Y(t)$. τ is defined as the ratio of the applied torque over the yield torque: $\tau = T/T_Y$

With the applied normalized torque $\tau = T/T_Y$ and the vibration amplitude Γ we now have two dimensionless control parameters that govern the type of flow. We can therefore in principle map out a *phase diagram* of weakly vibrated granular materials, and see what types of flow we observe for different flow conditions.

What are the phase boundaries we expect to observe? In chapter 2 we already explored the axis of $\Gamma = 0$: we expect to see no flow for $\tau < 1$, and a constant flow rate $\Omega(T)$ for torques applied above the yield stress $\tau = T/T_Y = 1$. The phase boundary at $\tau = 1$ can be expected to extend to nonzero Γ; this boundary is shown as the long dashed line in Fig. 6.7.

Below this boundary, at finite Γ and $0 < \tau < 1$, we expect another phase boundary, for the following reason. The vibrations periodically modulates the gravitational acceleration on the particles: $g(t) = g_0 + \Gamma \sin(\omega t)$ with g_0 the

gravitational acceleration. The total normal forces acting on the particles, which set the maximum frictional forces and therefore the yield stress, is thus varying periodically. This implies that the yield stress becomes time-dependent: $T_Y(t)$ is sinusoidally varying between $T_Y - \Gamma$ and $T_Y + \Gamma$. Above the lower boundary $T_Y - \Gamma$, there is always a moment during the vibration cycle where the applied torque T is larger than $T_Y(t)$. We therefore expect that there is a flow-no flow boundary at the line $\Gamma + \tau = 1$. This is the short dashed line indicated in Fig. 6.7.

6.4.2 Phenomenology
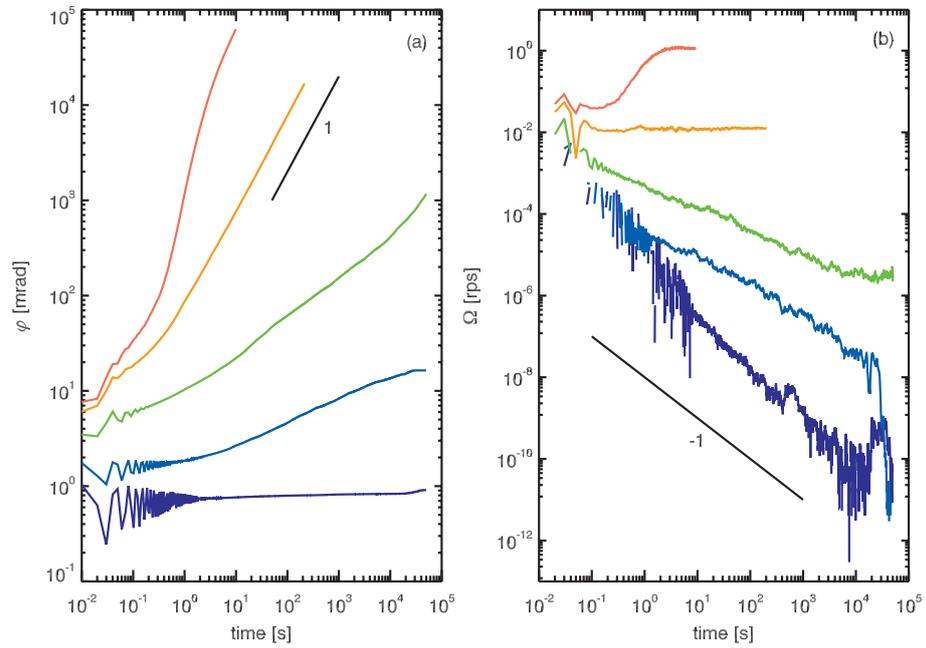
Figure 6.8: The phenomenology for constant torque experiments at $H/R_s = 0.33$. We show the deflection angle φ in (a) and its derivative $d\varphi/dt = \Omega$ in (b) as a function of time, for several τ, Γ combinations along the diagonal $\tau = \Gamma$ in the phase diagram: red: $\tau = 0.9, \Gamma = 0.92$; orange: $\tau = 0.7, \Gamma = 0.75$; green: $\tau = 0.5, \Gamma = 0.5$; light blue: $\tau = 0.2, \Gamma = 0.23$; dark blue: $\tau = 0.1, \Gamma = 0.14$. The black lines have a slope as indicated in the panels.

To obtain insight into the phase behavior, we explore the phase diagram along the diagonal $\Gamma = \tau$. The flow phenomenology is as shown in Fig. 6.8a,b. We plot there the deflection angle $\varphi(t)$ (a) and its derivative $d\varphi/dt$ (b) as a function

of time t for several different combinations of Γ and applied normalized torque τ. We use $H/R_s = 0.33$; the phenomenology is qualitatively similar tot that of $H/R_s = 0.7$. The small initial oscillatory motion, visible for small Γ, is due to transient flexure oscillations.

We distinguish three types of flow: *(i)* a rapidly accelerating flow, equilibrating at a constant large Ω within 10 seconds. This occurs for large Γ and τ, colored in red in Fig. 6.8. We refer to this as *fast steady* flow. *(ii)* Flow that equilibrates at a constant Ω quickly, but which is substantially slower than fast steady flows. This type of flow occurs for intermediate Γ and τ, (colored in shades of orange in Fig. 6.8), and we will refer to it as *slow steady* flow. *(iii)* for small τ and Γ, we observe flow with ever decreasing flow rate, for which equilibration is observed only after a very long transient, and which sometimes even does not equilibrate within experimental timescales, ($t < 10^5$) sec. The flow rate decreases roughly as a power law with an exponent smaller than one; compare to the black line in Fig. 6.8b. Colored in shades of blue in Fig. 6.8, we call the flow in this region *glassy* flow. We will make the distinction between these regimes more precise in sections 6.4.4 and 6.4.5 below.

6.4.3   Comparison to Constant Ω

From the instantaneous derivative of the deflection angle $d\varphi/dt = \Omega$ in Fig. 6.8, we can observe that for the fast and slow steady flow regimes, a well defined $\Omega(\tau, \Gamma)$ can be extracted. In the constant Ω experiments we obtained a relation $\tau(\Omega, \Gamma)$. We can now determine whether these functions are corresponding.

We do this in two ways. First, we plot Ω as a contour plot in the phase diagram for both the constant shear rate experiments (Fig. 6.9a) and the constant torque experiments (Fig. 6.9b). The scale for Ω is logarithmic. The similarity between the two contour plots is striking.

Secondly, a more detailed comparison is made by finding for each τ, Γ-pair from the constant torque measurements the closest matching τ, Γ pair from the data from the constant shear rate experiments, and plotting the corresponding Ω's from these matches against each other in a scatter plot. We show this parametric scatter plot in Fig. 6.9c. Ω_Ω are the speeds from the constant rate experiments, Ω_T are the steady state rotation rates from the constant torque experiments. The distance $(\tau_T - \tau_\Omega)^2 + (\Gamma_T - \Gamma_\Omega)^2$ for each τ, Γ pair is always smaller than 0.028. For a perfect correspondence, the data in the scatter plot should lie on the line $\Omega_\Omega = \Omega_T$, which is indeed the case for rotation rates measured over almost four decades. This shows that the flow rate in the fast and slow steady regimes does not depend on the type of rheometric experiment.
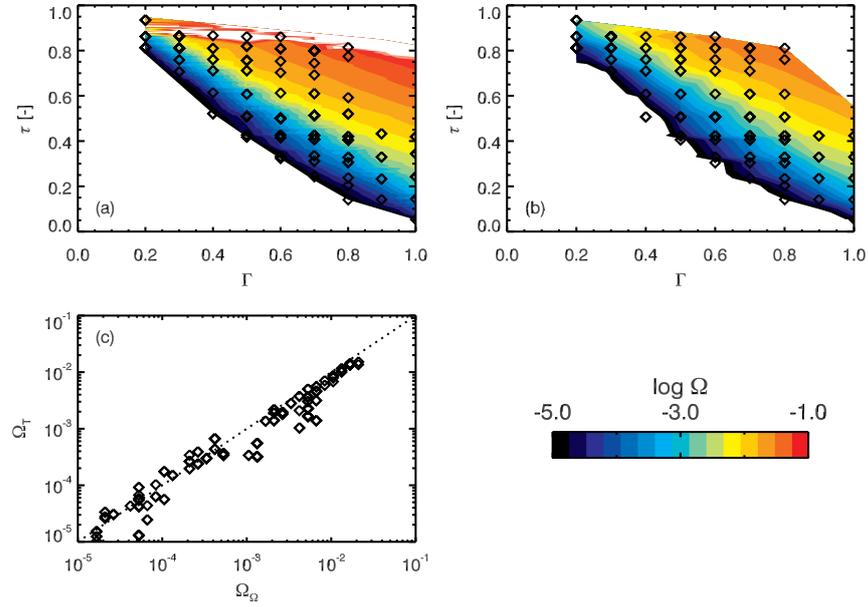
Figure 6.9: (a) $\Omega_\Omega(\tau, \Gamma)$, the data from the constant shear rate experiments shown in a contour plot. (b) $\Omega_T(\tau, \Gamma)$, the data from the constant torque experiments. As in (a), the color scale is $\sim \log \Omega$, and the + indicate the data used in the plotting. (c) The scatter plot comparison of the data shown in (a,b). Data for $H/R_s = 0.33$.

6.4.4 Slow Steady Flow to Fast Steady Flow

In the steady flow regime, we observe a clear transition between fast and slow steady flows. This transition is visible in both constant shear rate, and constant torque experiments. In the constant shear rate experiments, we see for $\Omega = 0.01 - 1$ rps that the driving torque T displays a minimum for certain Ω; this is evident from a close up depicted in Fig. 6.10a of the data shown previously in Fig. 6.6a. This regime of unstable flows can only be entered by driving the flow in constant shear rate mode: under constant applied torque, either fast flow, or slow flow is observed. This can be seen in Fig. 6.10b: the band of flow speeds $\Omega_{\text{forbid}}(\tau, \Gamma)$ that are never observed when driving at constant torque roughly corresponds to the band in which $T(\Omega, \Gamma)$ in Fig. 6.10a displays a minimum. Note that the minimum disappears for stronger vibration amplitude, for $H/R_s = 0.33$ shown in Fig. 6.10a it disappears around $\Gamma \sim 1$. This value is not robust to changes in H/R_S: for the $H/R_S = 0.7$ the minimum disappears at $\Gamma \sim 0.7$, as can

124
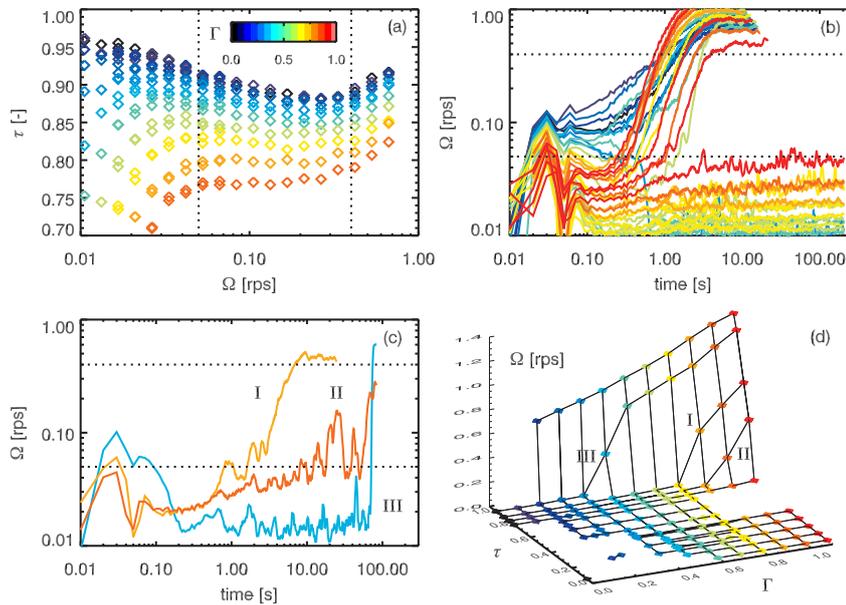
Figure 6.10: (a) The unstable branch reproduced from Fig. 6.6b. Color grading is proportional with Γ as shown and used for all panels. The dashed lines indicate the unstable region of rotation rates. (b) $d\varphi/dt(t) = \Omega$ for constant torque experiments close to the range of unstable Ωs. The dashed lines indicate the regime of flow speeds that are never observed under constant torque; the same dashed lines are shown in (a). In (c) are $d\varphi/dt(t)$ for values of τ, Γ in the unstable regime: I: $\Gamma = 0.9, \tau = 0.85$; II: $\Gamma = 1, \tau = 0.80$; III: $\Gamma = 0.5, \tau = 0.92$. (d) a wire plot plot of the steady state speeds in the upper part of the phase diagram. Ω is on linear scale to show sharp rise; the data points I, II, III in the transition regime correspond to the $\omega(t)$-data from (c).

be seen in Fig. 6.6a.

Close to the transition, the fluctuations in Ω increase, as is visible in Fig. 6.10c, run I and II. In some runs, the rotation rate is within the regime of slow steady flow for considerable time, after which it suddenly changes to fast steady flow. See for example run III in Fig. 6.10c.

A wire plot of the steady rotation rate of the disk in the phase diagram in Fig. 6.10d clearly shows that the fast steady regime is limited to the upper right corner of the phase diagram. The intermittent flow curved I, II and III clearly lay

on the boundary between slow and fast steady flow.

     Location of the phase boundary -- Can we explain the location of the phase boundary? The instability seems to be set by the flow speed, rather than the more indirect control parameters Γ and τ. It is therefore instructive to look at the inertial number $I = \dot{\gamma}d/\sqrt{P/\rho}$, a measure used to determine the onset of fast, rate dependent grain flows (see section 1.5.1). In the split-bottom geometry the strain rate $\dot{\gamma}$ varies throughout the cell, but yet we can estimate the inertial number as follows. We approximate $\dot{\gamma}$ with half the width of the shearband at the surface: $\dot{\gamma} = 2\pi R_s\Omega/(W/2)$; we set $W \sim 5d$. We take the pressure $P = \rho g(H/2)$ to be half of the maximum pressure felt at the bottom. This yields $I = 4\pi R_s\Omega d/W\sqrt{gH/s}$, which gives at $\Omega = 0.5$, $I \sim 0.1$. This is close to $I \sim 1$, the onset of rate dependence given the crude approximations made to estimate I.

     This suggests that the flow transition we observe here is between fast, slightly diluted flows, where both collisions and frictional interactions play a role, and a slow flow regime, where enduring contacts are dominant. This suggests that in the faster flow regime, we should see a small rise in the surface of the grains; however, the particle size and aspect ratio of the system are such that this cannot be measured accurately.

     Although in the inertial number theory, no flow instability occurs, a hysteretic transition from flow to no-flow conditions, under constant stress in Couette geometries was observed already before (see Ref. [2] and references therein). The weak vibrations used in our experiment change the flow to no-flow transition into a transition between slow flow and fast flow; it would be interesting to see whether there is also hysteresis in these weakly agitated systems.

6.4.5   Transition: Into Glassy Flow

For increasingly weaker driving under constant torque, the flow becomes slower, and starts to develop long transients. We show now that both the drop in rotation rate, and the increase in the transient timescale occur abruptly at an unexpected boundary in the phase diagram.

     To show this, we do several different experimental runs on the diagonal of the phase diagram shown in Fig. 6.11a. The transient timescales at small τ and Γ are so long that within experimentally accessible timescales, no well defined steady state rotation is reached. Therefore, we plot the total deflection angle divided by measurement time $\varphi(t)/t$, to study the asymptotic behavior for $t \to \infty$. We call $\varphi(t)/t$ the *average rotation rate*. We use the average rotation rate, and not the instantaneous rotation rate $\Omega = d\varphi/dt$ used above, since Ω becomes increasingly harder to measure at small rotation rates. It shows the same trends
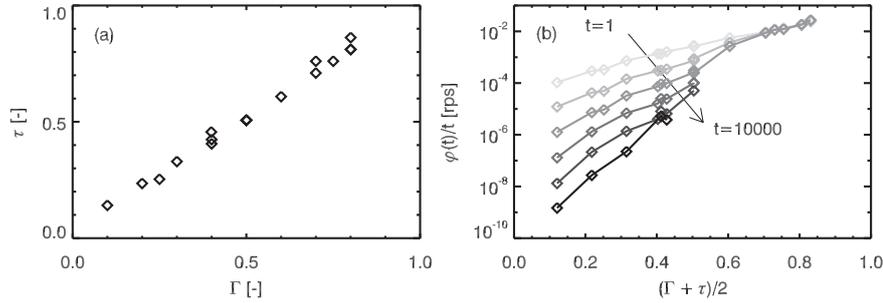
Figure 6.11: (a) The points in the phase diagram, shown in (b). (b) The average rotation rate $\varphi(t)/t$ (see text) for the points shown in (a). Different grayscales correspond to different t, $t = 1, 10, 100, 1000, 10000$; darker lines are larger t as indicated by the arrow.

as $\varphi(t)/t$ however.

The variation of the average rotation rate $\varphi(t)/t$ as a function of t and the two control parameters Γ and τ, is shown in Fig. 6.11b. Both a reduction in τ and in Γ lead to a reduction in average speed, so we plot $\varphi(t)/t$ as a function of the combined parameter $(\Gamma + \tau)/2$.

We note several features in Fig. 6.11b: at large τ and Γ, the average speed does not depend on t varied between 1 and 10000 seconds; the flow has reached a steady state rotation rate before $t = 1$. In this region, the average rotation rate is weakly dependent on the distance to the origin of the phase diagram $(\Gamma + \tau)/2$. This is the regime of slow steady flows.

For $(\Gamma + \tau)/2 \lesssim 0.7$, this behavior changes completely. From that point, $\varphi(t)/t$ starts to depend strongly on the measurement time t. Initially however, this dependence on t seems to disappear after some given $t(\Gamma, \tau)$ that depends on vibration amplitude and applied torque. This is an indication that $\Omega(t)$ becomes constant after some time.

For $t \to \infty$, most Γ, τ combinations seem to approach the line $\varphi(t)/t \sim \exp(-[\Gamma - \tau])$, drawn in Fig. 6.11b. For smaller Γ and τ it takes longer to approach this line, but this asymptotic behavior is not manifest, so this data is not conclusive about whether flow is possible for *all* Γ, τ-combinations.

We identify this regime characterized by long transients with the regime of glassy flows.

Location of the phase boundary -- The location of the well defined boundary between slow steady and glassy flows is however non-trivial. We

expected to see a change of flow behavior around the line $\Gamma + \tau = 1$ on the basis of the periodic modulations of the yield torque (see section 6.4.1). This would be at $(\Gamma + \tau)/2 = 0.5$, and not 0.7, the value at which we see the transition to glassy flow. Another notable observation is that even in glassy flows, we see equilibration to a steady state rotation rate, even below the line $(\Gamma + \tau)/2 = 1$, a region in which the applied torque is always below the periodically modulated yield stress.

As in the transition from slow to fast steady flows, the transition between slow steady flow and glassy flow seems to be at a specific flow rate, with $\Omega \sim 0.005$ rps. The only relevant timescale for these slow flows is the vibration frequency. The lengthscale associated with the transition is therefore $0.005/f$, where f is the vibration frequency, multiplied by a lengthscale of the system; for this we can take both R_s and H, since they are of similar order. This gives a lenghtscale of about 1 micron, the size of the microscopic asperities on the glass beads. It is known that these microscopic asperities are relevant in the macroscopic dynamics of granular systems [102], and that lengthscales much smaller than d play a role in the heterogeneous rearrangement dynamics that dominate these glassy flows [103]. Mechanically, weak vibration with peak acceleration below g cannot induce macroscopic rearrangements, so in line with the conclusion with Ref. [103], we conclude that weak vibrations make the system explore the phase space of different contact configurations rather than different structural arrangements.

6.5   Relaxation in the Absence of Stress

Vibrations induce compaction in granular media [104], even in the limit of $\Gamma \to 0$ [96]. This relaxation process shows up in two parts of the experiments: before switching on the torque, but after applying pre-shear, we wait for typically 5 seconds while $\Gamma > 0$. This *wait time* is to let the packing and disk return to a quiescent state. The wait time can be varied, and this affects the rheology of the granular flows. We discuss the effect of changing the wait time in section 6.5.1.

Secondly, after the experiment in which we monitor position and speed of the disk, the torque-induced rotation of the disk has induced a preferential flow direction in the system [105]. This built-in anisotropy shows up after the experiment is finished, when we switch off the torque, but not the vibrations: the disk then relaxes under influence of the vibration by rotating a small amount in the direction opposite to the torque-induced rotation direction. We discuss this effect in section 6.5.2.

6.5.1 Pre-shear Protocol & Wait Times
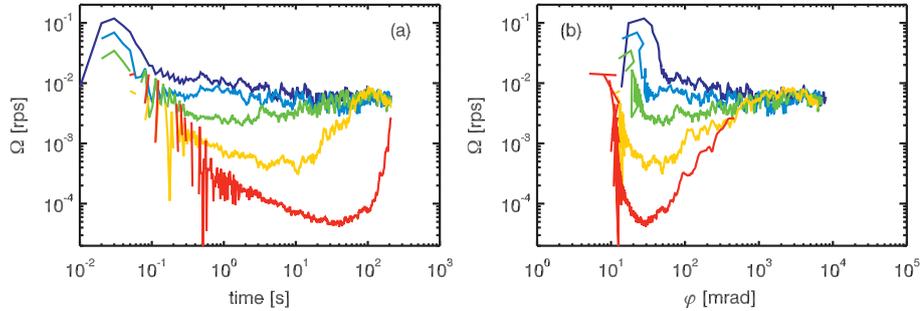
Figure 6.12: (a) The rotation rate as a function of time at $\Gamma = 0.5$ and $\tau = 0.8$. Colors indicate different wait times in the pre-shear protocol: dark blue: 1 second; light blue: 10 s; green: 100 s; orange: 1000 s; red: 10000 s. In (b) the same data is shown as a function of the total deflection angle φ.

We study the effect of the wait time by carrying out a constant torque experiment at $\Gamma = 0.5$ and $\tau = 0.8$. We do five different experiments at these settings, and we vary only the wait time before switching on the torque. The wait times used are 1,10,100,1000 and 10000 seconds. The resulting rotation rate as a function of time is shown in Fig. 6.12a; note that the wait time occurs before $t = 0$ in this plot. Clearly, the initial transient is strongly affected by the wait time. The time it takes to reach a steady state rotation rate increases strongly with the wait time. This is however only due to the reduced speeds during the transient -- the transient lasts the same amount of strain for all wait times, as shown in Fig. 6.12b.

Clearly the wait time only affects the initial transient, and not the steady state rotation rates attained. The fact that the granular material is however changing under the influence of vibrations alone, could shed more light on the nature of the transients observed in the glassy flow regime.

6.5.2 Strain Relaxation

Shear reversal experiments [105] have shown that granular materials develop an anisotropy in the contact network after being sheared over a finite strain amplitude. Such structural anisotropy is also observed in colloidal suspensions [106]. The anisotropy buildup also shows up as a small reversed flow after stopping a rheometric experiment on glassy colloidal suspensions [107]. This relaxation in

129
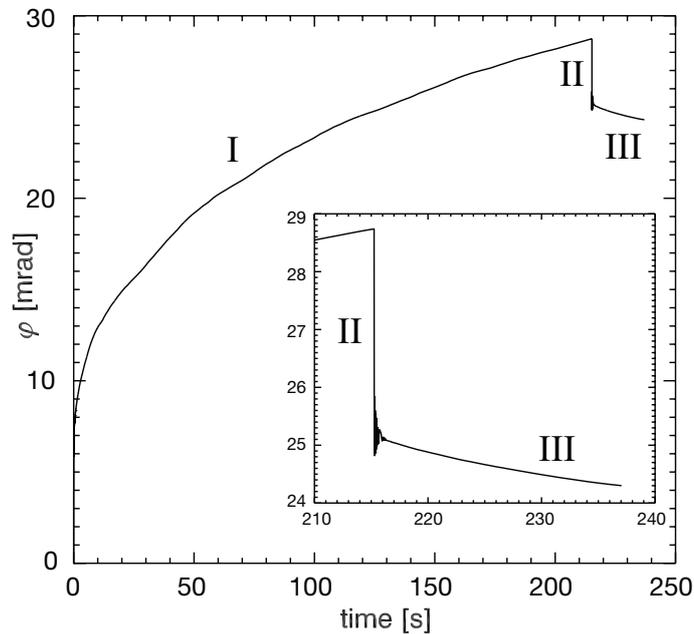
Figure 6.13: The phenomenology in a typical constant torque experiment: $\tau = 0.5$, $\Gamma = 0.25$. I movement of the disk under constant torque. II switching off the torque. III The relaxation process in the absence of any applied stress. The inset zooms in on stage II and III of the experiment.

the absence of any externally applied shear stress can occur due to the thermal fluctuations that allow the colloidal system to age. In ordinary granular systems, thermal fluctuations are negligible, so this relaxation is typically not observed. However, the weak vibration in our experimental system act as a similar source of force fluctuations, and therefore make such a relaxation possible.

This can be seen in a typical constant torque experiment, shown in Fig. 6.13. After applying a constant torque for about 215 seconds (stage I), the torque is switched off. The flexure deformation relaxes quickly[4] in stage II; a short transient oscillation can be seen at the end of this stage. Then, during stage III, no external torque is applied. However, Γ is still nonzero, and this allows the disk to move; this process is what we call *relaxation*. Note that in the case that stage I is in the fast steady regime (not shown), the inertia of the rotating disk first has to decay after switching off the torque, before the relaxation process is

---

[4]This deflection angle step is always a factor two larger than what is expected on the basis of the applied torque and the spring constant of the flexure. We have no explanation for this.

observed.
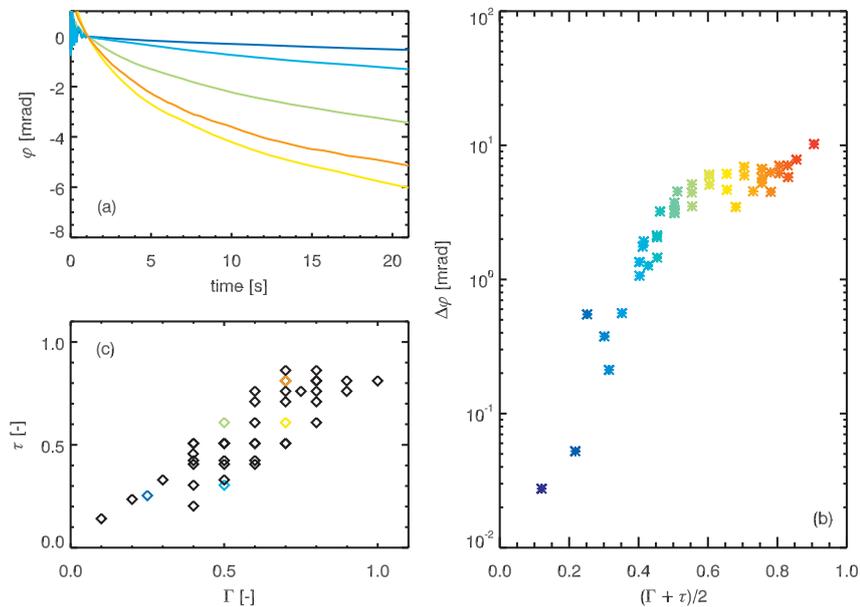
Figure 6.14: (a) Typical stage III relaxation curves. All curves are normalized: $\varphi(t = 1s) = 0$. Dark blue: $\tau = 0.25, \Gamma = 0.25$; light blue: $\tau = 0.3, \Gamma = 0.5$; green: $\tau = 0.61, \Gamma = 0.5$; yellow: $\tau = 0.61, \Gamma = 0.7$; orange: $\tau = 0.8, \Gamma = 0.7$. (b) The deflection between $t = 1s$ and $t = 21s = \Delta\varphi$, as a function of the combined agitation parameter $(\Gamma + \tau)/2$. (c) The data from (b) shown in the phase diagram. The colored points correspond to the curves shown in (a). $H/R_s = 0.33$.

The relaxation process depends on both τ and Γ. We show this in Fig. 6.14a. For several τ, Γ-combinations, we plot stage III of the relaxation process. For the different Γ, τ values, the functional form of $\varphi(t)$ is the same; only the relaxation amplitude amplitude is different for different vibration strengths and applied torques. This amplitude, measured arbitrarily as $|\varphi(t = 21s) - \varphi(t = 1)|$, we plot as a function of the combined parameter $(\Gamma + \tau)/2$ in Fig. 6.14b. Note that we omit the fast steady relaxation data; it is similar to the slow steady relaxation but cannot be readily obtained with the $\Delta\varphi$ measure, since after switching off the torque after a fast steady run, it takes takes a few seconds for the inertial transient to die out.

We distinguish several characteristics: The maximum amount of relaxation

is about 10 mrad, which corresponds to half a particle diameter at the edge of the disk. Moreover, for smaller Γ and τ values, we see a sharp reduction in the relaxation amplitude. At a threshold in $1/2(\Gamma + \tau) = 0.6$, the border between slow steady and glassy flow identified in section 6.4.5, the total relaxation amplitude starts to decrease more strongly with $1/2(\Gamma + \tau)$, although in this regime, a steady state had not been reached during the constant torque experiments, before the torque was turned off and the relaxation measurements were recorded. However, for the relaxation only the buildup of an anisotropy is necessary, and this happens also at higher flow rates, so also during the pre-shear that precedes the glassy flow experiments. This means that for all data shown, enough strain has been applied to build up the anisotropy.

6.6 Conclusions
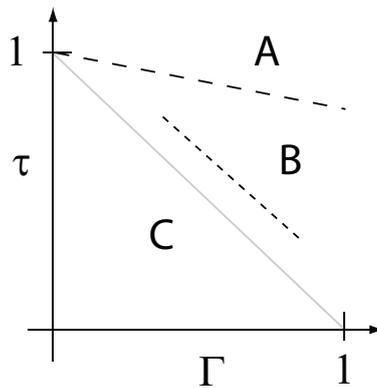
Figure 6.15: A sketch of the new phase diagram, with the experimentally determined phase boundaries. Long dash: the separation between fast steady flow (A) and slow steady flow (B). Short dash: the phase boundary between slow steady flow and glassy flow (C). The grey line is the line originally expected to be a phase boundary.

Weak vibrations strongly change the rheology of granular materials. We find that the rate independence for small rotation rate disappears immediately if vibrations are present. We distinguish three distinctly different types of flow, as shown in Fig. 6.15, separated by clear phase boundaries:

A: Fast steady flow -- For large driving strengths and vibration amplitudes,

we find fast steady flows, that depend weakly on the vibration amplitude. Such fast flows are also found for $\Gamma = 0$.

B: Slow steady flow -- For weaker driving, we find steady flows for which the driving rate is substantially lower than for the fast steady flows. The transient time necessary to reach this steady rotation are about 1 second. The rotation rates depend weakly on both τ and Γ.

C: Glassy flow -- At small τ and Γ, we find a well defined transition to a flow regime where ageing is predominant; we observe long transients. However, we see that steady state flow is reached after this transient as long as the transient is shorter than experimental timescales; the asymptotic behavior of the transient hints that even if the transient becomes very long, steady state rotation is still reached. This rotation rate depends exponentially on both τ and Γ.

We also find that at $\tau = 0$, but $\Gamma > 0$ relaxation appears if the system has experienced strain. This implied that also when $\tau > 0$, this relaxation competes with the onset of flow. This, we think, causes the transients to appear in the glassy flow regime.

6.7 Appendices

6.7.1 A: Mechanical Characteristics of the Setup
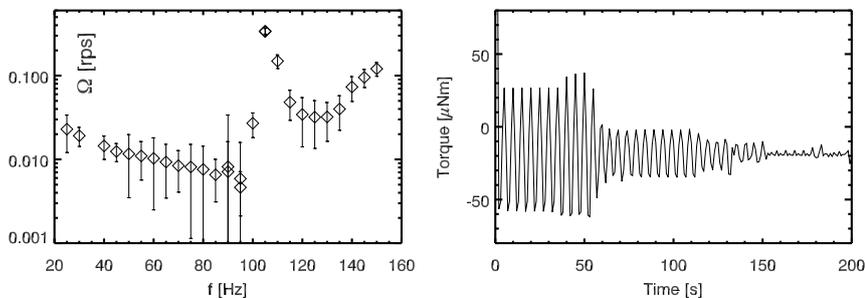
Figure 6.16: (a) Steady state rotation rate dependence on the vibration frequency, measured with $\Gamma = 0.5, \tau = 0.8$. (b) A typical torque signal under constant rotation rate during the alignment of the air bearing. One oscillation period corresponds to a full rotation of the disk

Vibration frequency -- The experiments we do should not be greatly

affected by the choice of the vibration frequency. Therefore we measure what the effect is of the vibration frequency on the flow properties that we probe in our experiments. We measure this effect by determining how the steady state rotation rate Ω under a constant applied torque $\tau = 0.8$ and fixed vibration amplitude $\Gamma = 0.5$ depends on the vibration frequency f. We carry out the measurements with a filling height of $H/R_s = 0.55$. The result is shown in Fig. 6.16a. We see that for vibration frequencies between 50 and 75 Hz, the rotation rate depends only marginally on the vibration frequency. We choose the middle of this regime, $f = 63$ Hz to carry out all experiments discussed in this chapter.

Alignment of the bearing -- We manually align the rheometer with the disk axis by setting a constant rotation rate to the disk, with no particles in the container. While the disk rotates, we monitor the required torque to run the disk at the set speed. Typically, this torque has a periodic modulation. Alignment of the two axis with the set screws on the air bearing then should reduce the amplitude of this periodic modulation on the torque. A typical alignment run is shown in Fig. 6.16b: the modulations can be minimized to an amplitude of about 10 μNm. A small offset also remains, due to the asymmetric air flow between the flat bearings and the flange shown in Fig.6.3a.

A New Control Parameter for Compaction

7.1 Introduction

Static packings of granular materials can be mechanically stable over a whole range of packing fractions. For example, think of the coffee powder in a tin -- it is loose when pored in, it can compacted when tapped, but when not tapped, the powder will keep its density. In packings of frictional granular materials, this remarkable behavior is caused by two effects: First of all the frictional forces between pairs of particles are essentially Coulomb-like friction forces; the frictional interactions can have any value F_F between 0 and μF_N, with μ the friction coefficient, and F_N the normal force between two particles. That makes the tangential forces on the between particles non-unique. Secondly, adding non-unique tangential forces to the total number of forces acting a particle, makes it possible for particles to be mechanically stable without having a fixed number of contacts [108][1], Reducing the necessary number of contacts on a particle also reduces the average distance between particles, and therefore allows for lower densities to occur.

More than a decade ago, a now classic series of experiments probed the compaction of dry glass beads in a narrow tall tube which was tapped

---

[1]For packings of frictionless spheres counting of total number of forces and the total number of degrees of freedom for a single sphere gives that in order to have a stable packing, only 6 contacts per particle are required.

vertically [109--111]. Very rich dynamics were observed: starting from a loose packing, the density was observed to exhibit slow, logarithmic growth as a function of the number of applied taps. Memory effects, in which the density evolution depended on the tapping history, were also found [112]. After having applied a large number of taps however, in all experiments a state was reached where the packing density depends only on the tapping strength and not on the history [104]. From such a state the so-called reversible branch could then be obtained repeatedly and reversibly by slowly ramping up and down the tapping intensity. On this branch, there is a fully reversible, one-to-one relationship between the tapping strength and the packing fraction[2] The long transient phenomena and memory effects all occur along the so called irreversible branch, along which the system has to evolve before reaching the reversible branch.

The mechanism or mechanisms that determine the relation between tapping 'intensity' and volume fraction is however far from clear. In later studies of compaction in much wider containers, convection was found to be an important mechanism in driving the compaction [77, 78, 113]. In these experiments the temporal evolution of the density on the irreversible branch was found to be different [77, 78, 104, 113], but again the same reversible branch was found.

One of the open questions is thus: what is the appropriate control parameter that characterizes the taps? A widely used characterization of taps is the ratio of their peak acceleration and the gravitational acceleration, Γ. Certainly the peak acceleration is important in that it allows to distinguish between tap strengths where no liftoff of the packing occurs, for $\Gamma < \Gamma^* \approx 1$, and taps where that does happen [113]. Recent numerical work on the irreversible branch dynamics of compaction has suggested that the dimensionless acceleration parameter is not appropriate for rescaling the data [114]. Moreover, recent numerics [115] of compaction under sinusoidal driving vibrations indicate that the vibration frequency also influences the reversible branch, and similarly, supporting evidence for the role of tap duration can already be found in the observations of Macrae *et al.* [116].

In this chapter we address the question of the appropriate control parameter by studying the packing density on the reversible branch in experiments in which we expose granular packings to single cycle sinusoidal discrete taps with $\Gamma > 1$, where we control and vary both the the tap amplitude A and its duration T (Fig. 7.1). For sinusoidal taps as used here, Γ can be given in terms of A and

---

[2]Even though changing the tapping strength does induce a small transient in the packing fraction -- a change in tapping amplitude does not produce an instantaneous change in packing fraction.

T: $\Gamma = A\omega^2/g$, with $\omega = 2\pi/T$ the radial frequency, and g the gravitational acceleration. Since we have precise control over the acceleration signal, we can vary both Γ and ω independently (see Fig. 7.1b).

For given T, we obtain similar reversible branches $\Phi_{rev}(\Gamma, T)$ as were observed before for fixed T, both for a bidisperse glass bead mixture and a bronze powder, and the reversible densities $\Phi_{rev}(\Gamma, T)$ depend both on T and Γ. We find that all data can be collapsed in good approximation by plotting the packing fraction as function of ΓT, which is close to the liftoff velocity, or similarly, the time of flight of the granular packing. In addition we probe what happens when we alternate the taps between pairs of different Γ and T for which $\Phi_{rev}(\Gamma, T)$ are equal, and we find no appreciable hysteresis.

We therefore show that Γ is not the appropriate control parameter in the density dynamics of vibrated granular media. This result has an important practical application: it is often creating a steady state density and suggests using variations of T as well as variations of Γ to reach different densities along the reversible branch. For example loose packings can be reached best by combining large Γ and large T.

7.2 The Experiment

7.2.1 Setup

We study granular compaction in a glass tube (diameter 26 mm, height 20 cm) filled with grains. The typical filling height is 10 cm. The glass tube is shaken vertically in the same way as the split-bottom cell was driven in chapter 6: we use a shaker (VG100, VTS systems), driven by a commercial audio amplifier (Crown CE1000). The shaker is placed on a stack of concrete tiles, with rubber mats sandwiched between them (Fig. 7.2a) in order to reduce the mechanical coupling of the shaker to the environment. The vertical motion of the tube is guided by a round air bearing ($\varnothing$ 1", New Way) mounted on a table (Fig. 7.2a) which is levelled. Levelling eliminates heaping, the unwanted tilting of the surface of granular media subjected to vibrations [100]. Also here, a 0.5 meter long and flexible aluminum rod couples the tube and the shaker (see Fig. 7.1a and Fig. 7.2a)). This rod eliminates the necessity of excessively accurate alignment of the axes of the air bearing and the shaker.

The vertical acceleration of the tube is measured with an accuracy of $10^{-3}g$, by a combination of two accelerometers (Dytran E3120AK and a modified
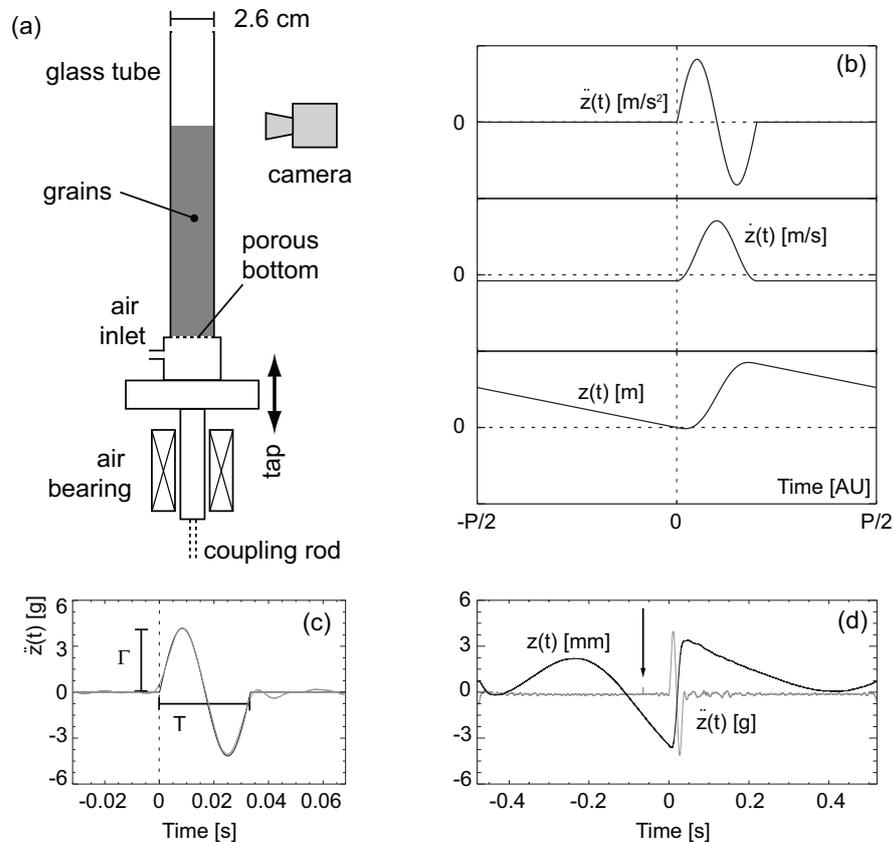
Figure 7.1: (a) Sketch of the experimental setup. (b) Sketch of the waveforms of $\ddot{z}(t)$, $\dot{z}(t)$ and $z(t)$, illustrating the offset and linear slopes present in $z(t)$, stemming from continuity requirements. (c) Comparison between desired waveform (grey) and actual waveform (black) of the vertical acceleration $\ddot{z}(t)$. (d) A typical measured position (black) and acceleration (grey) signal. The arrow indicates the phase at which the packing fraction is measured.

ADXL320EB[3]) -- see Fig. 7.2d. For consistency checks, we occasionally monitor the position $z(t)$ of the glass tube with an inductive position sensor (Messotron WLH50, 10^{-5} m resolution) -- the acceleration measurements are far more sensitive and these will be used in the feedback scheme described below.

---

[3] Its factory default bandwidth of 50 Hz is increased to 2kHz.
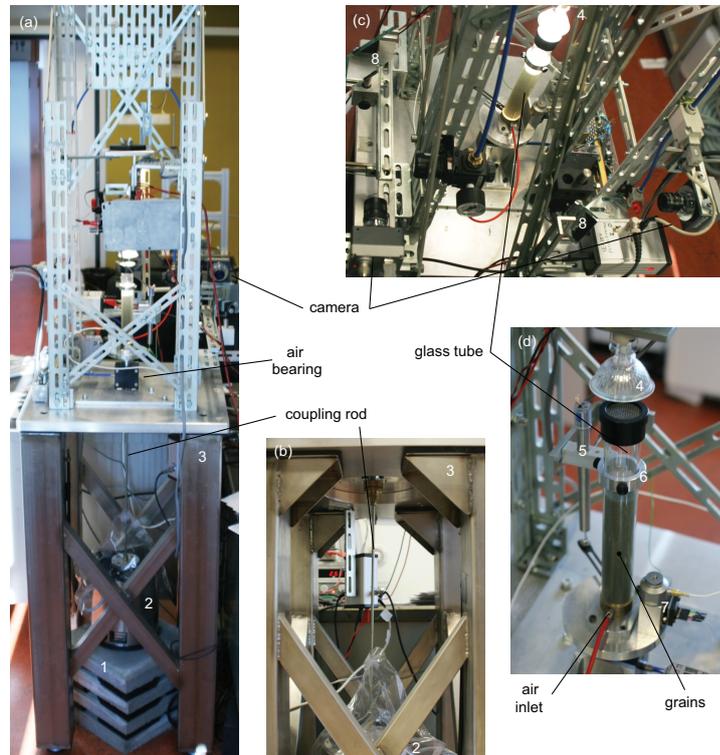
Figure 7.2: Photos of the setup, with parts indicated in Fig. 7.1. (a) The whole setup, with a close-up of the table (b), the camera arrangement and glass tube (c), and the glass tube alone (d) -- see Fig. 7.4 for a technical drawing of figure part (d). Numbers indicate several parts mentioned in the text: 1 - concrete slabs with rubber mats; 2 - the shaker; 3 - the table; 4 - halogen light for bronze powder illumination; 5 - LVDT position sensor; 6 - marker ring for serving as reference height in images; 7 - accelerometers; 8 - mirrors.

7.2.2 Waveform Generation

In order to create a tap where both the duration and strength can be controlled independently, we need to determine the waveform $z(t)$. We denote the duration of the tap by $T = 2\pi/\omega$, the period of the tap by P (we will fix it later at 1 second), and have the tap start at $t = 0$. We demand than that $z(t)$, $\dot{z}(t)$ and $\ddot{z}(t)$ are continuous, that $\int dt\dot{z}(t) = 0$ and $\int dt\ddot{z}(t) = 0$, and that $z(0) = 0$. These requirements severely constrain the tap -- for example, taking for $z(t)$ a single sine cycle followed by a period where $z = 0$ makes $\ddot{z}(t)$ discontinuous. Starting

from a single sine cycle for $\ddot{z}(t)$, obtaining $\dot{z}(t)$ and $z(t)$ by integration, and fixing the integration constants so that the continuity conditions are full filled, we find the waveform summarized in Table 7.1 (see Fig. 7.1b):

	$0 \leq t \leq T$	$T \leq t \leq P$
$\ddot{z}$	$A\omega^2 \sin(\omega t)$	0
$\dot{z}$	$-A\omega \cos(\omega t) + b_1$	$-b_2$
z	$-A \sin(\omega t) + b_1 t$	$-b_2(t - P)$

Table 7.1: Waveform of the tap. Here the integration constants equal $b_1 = A\omega(P - T)/P$ and $b_2 = a\omega\,T/P$.

In order to create such a tap, a feedback algorithm is used to adapt the Fourier components of the signal fed into the audio amplifier such that the measured acceleration signal converges to the desired waveform.

The algorithm works by iteratively adapting the Fourier components of the driving wave, which we will call $\zeta(t)$. The driving wave is feeded into the audio amplifier, and iteratively modified by the algorithm in such a way that the measured acceleration signal of the tube $\ddot{z}(t)$ converges to the desired waveform.

The feedback algorithm starts by feeding an arbitrary trial wave $\zeta_0(t)$ into the amplifier and measuring the response $\ddot{z}_0(t)$ of the container to this trial function. Schematically, this process would look like

$$\zeta_0(t) \rightarrow \text{Electronics} + \text{Mechanics} \rightarrow \ddot{z}_0(t)$$

We write this as $\ddot{z}_0(t) = H(t)\zeta_0(t)$, with $H(t)$ the "transfer" function of the electronic and mechanical components combined. Let $\ddot{z}_\infty(t)$ be the waveform to which the algorithm should converge. We denote the Fourier transform of $\ddot{z}(t)$ with $\widetilde{\ddot{z}}(\omega)$. Comparing the Fourier transforms $\widetilde{\ddot{z}}_\infty(\omega)$ and $\widetilde{\ddot{z}}_0(\omega)$, the routine determines in the following way how it has to adjust the amplitudes and phases of the individual modes in $\widetilde{\zeta}_0(\omega)$ to obtain the second trial function $\zeta_1(t)$:

$$\begin{aligned}
|\widetilde{\zeta}_1(\omega)| &= \widetilde{\zeta}_0(\omega)\frac{\widetilde{\ddot{z}}_\infty(\omega)}{\widetilde{\ddot{z}}_0(\omega)} \\
\arg(\widetilde{\zeta}_1(\omega)) &= \widetilde{\zeta}_0(\omega) + \widetilde{\ddot{z}}_\infty(\omega) - \widetilde{\ddot{z}}_0(\omega).
\end{aligned} \qquad (7.1)$$

The continuation of this iteration is straightforward. Typically the algorithm converges sufficiently to $\widetilde{\ddot{z}}_\infty(\omega)$ within 5-10 iterations, after which it is stopped

manually. The feedback algorithm described above is necessary since the "transfer" function $H(t)$ is not known *a priori*. It can be measured independently, but $H(t)$ changes if one makes slight changes to the setup, adds extra granular materials etc., which would require remeasuring $H(t)$ after each modification.

After this preparatory step, the shape of the output wave is not changed during the actual experiment; it is only multiplied by a scale factor to set its overall amplitude Γ. We have checked that the system is sufficiently linear so that re-calibration of the waveform is not necessary when Γ is varied.

Taps are applied once every second, so $P = 1$; this allows the packing to come completely to rest before the start of a new tap. In Fig. 7.1c, the desired waveform for $\ddot{z}(t)$ is compared to a typical measured acceleration signal -- the waveform produced by the feedback scheme is in good agreement with the desired tap. In Fig. 7.1d, a measured waveform for $z(t)$ and and accompaning $\ddot{z}(t)$ are shown. The slow downward motion of the tube anticipated in Table 7.1 is clearly visible. This downward motion is not at constant speed due to low-frequency limitations in the electronics that drive the shaker. The accelerations associated with this non-constant speed are however always below g, so they do not influence the packing fraction measurably.

7.2.3   Parameter Range and Grain Dynamics

As was established in [113], the dynamics of compaction dramatically slows down when the tapping peak acceleration Γ falls below a critical value Γ^* which is typically slightly above 1. This transition is accompanied by a change from a regime where the grains experience lift off for $\Gamma > \Gamma^*$ to a regime where they do not. In our experiments, the values of Γ range from 1 to 15, and by high speed imaging we have established a clear lift off and expansion of the whole column of grains for $\Gamma \gtrsim 2$ -- the precise value of Γ^* in our experiments is likely somewhat smaller. The vast majority of our data is therefore taken in the regime where the grains loose contact with the bottom plate and their neighbors.

7.2.4   Packing Density and Material Used

The packing density is determined from the height of the granular column, and this height is measured with a camera that observes the packing from the side, as in Refs. [102, 117]. To reduce the overall size of the setup the fixed optical pathway goes via a mirror for both cameras, as shown in Fig. 7.2c. This also is facilitates alignment. We use standard B/W FireWire CCD cameras from Foculus,
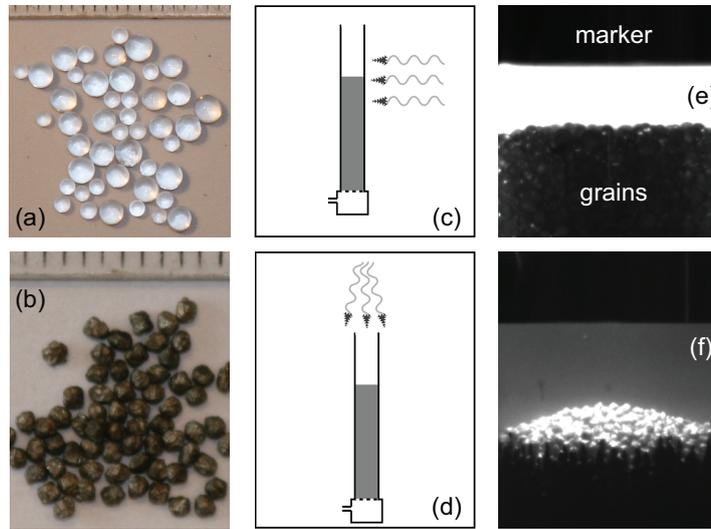
Figure 7.3: The granular materials used in the experiment (scale = 1mm): (a) glass beads, (b) bronze powder. Illumination direction: (c) for glass, from the back, (d) for bronze, from the top. Typical camera image (e) glass, (f) bronze. For bronze powder two cameras are used, image is typical for both.

models FO432B (1392x1040 pixels) and FO114B (659x494 pixels). The camera is triggered for strobed image acquisition, such that the camera takes a picture just before the start of the tap: the trigger moment is indicated by the arrow in Fig. 7.1c. A ring-shaped dark marker, whose height from the bottom of the tube is known (typically 13 cm), is attached to the tube, slightly above the maximum height of the bead pack -- see Fig. 7.2d. Depending on the grains used we use lighting from behind (for glass beads), or from the top (for bronze powder) -- see Fig. 7.3c-d and Fig. 7.2d. The top illumination we use for the bronze powder allows us to use two cameras. With two cameras we are able to image the whole surface, and not just a two dimensional projection. This allows us to check whether heaping is present or absent. Determining the height of the packing in both cases amounts to counting pixels with intensity above a certain threshold value. The threshold value is determined from the histogram of a typical image. We verified that the imaging method applied gives a linear relationship between the amount of grains in the tube and the number of pixels in the gap.

We employ two types of granular matter: a bidisperse mixture of glass beads (Pneumix, 1.6 and 2.3 mm in 1:1 volume mixture, Fig. 7.3a), or monodisperse bronze powder (Acupowder, grade '12HP', $\sim$ 1mm diameter, Fig. 7.3b). The glass

bead packings generally have a flat surface, while the bronze beads grow a small radially symmetric heap at their surface (this heap is likely due to convection) when exposed to taps. One important difference is that the glass beads tend to be more sensitive to triboelectric effects, which result in overall, run-to-run variations of the absolute density (the trends in the variation of Φ_{rev} with Γ are not affected by such variations). We observe that such variations are absent for the bronze powder. Importantly, our essential findings (control parameter $\sim \Gamma T$ and no hysteresis) are seen with both materials.

Our measurement method yields a high resolution; the noise in the determination of the height in the packing due to camera pixel noise alone is $30\mu m$, this translates into a variation of Φ of $\sim 0.03\%$. However, this method gives a relatively poor accuracy in the absolute value of Φ. This is due to the cumulative effect of the errors in the determination of the height of the marker, the inner diameter of the tube, the density of the beads, image calibration and the thresholding. The packing fractions stated in here therefore have an estimated systematic error of 1.3%. Since $\Phi = W/V\rho$, with W the total weight of grains in the glass tube, V the volume occupied by the grains, and ρ their bulk density, we can calculate the error as follows[4]:

$$(\frac{\Delta\Phi}{\Phi})^2 = (\frac{\Delta W}{W})^2 + (\frac{\Delta V}{V})^2 + (\frac{\Delta\rho}{\rho})^2, \tag{7.2}$$

with Δa the absolute error in quantity a. We measured the bulk density ρ by immersing a known weight of bronze powder in a liquid in a graduated cylinder, and measured the resulting height increase of the liquid surface. This gave $\rho = 8.8 \pm 0.1$ kg/m^3. The typical wight W-error on 300 grams of grains used is ± 0.1 gram. The error in the volume is the combination of errors in the determination of the cylinder radius (0.38%), the height of the reference ring (0.15%), the pixel-millimeter calibration (0.04%) and the height of the granular bed (1%). For subtracting and adding quantities, e.g. $a + b = c$ or $a - b = c$, the error propagates as $(\Delta c)^2 = (\Delta a)^2 + (\Delta b)^2$, we arrive at

$$(\frac{\Delta\Phi}{\Phi})^2 = 1.1 \times 10^{-7} + 3.5 \times 10^{-5} + 1.29 \times 10^{-4}, \tag{7.3}$$

This yields $\Delta\Phi/\Phi = 1.3\%$. It is clear from Eq. 7.3 that the dominant source of uncertainty in Φ comes from the uncertainty in the determination of the bulk density of the bronze powder.

---

[4]We will only do this for bronze powder, for glass particles the error is slightly larger due to the increased absolute error in the determination of the bulk density.

7.2.5   Experimental Protocol
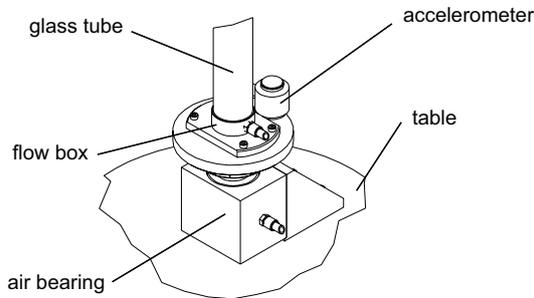
Figure 7.4: A technical drawing of the glass tube, and the way it is mounted, in combination with the flow box and the accelerometer; only the Dytran accelerometer is drawn here. The flow box is used for the fluidization before the start of the experiment. The top of the flow box inside the glass tube is perforated, as indicated in Fig. 7.1.

The bottom of the tube is perforated and connected to a flow box so dry air can be pumped through the bead pack -- see Fig. 7.4. We always start an experiment by fluidizing the packing with several pulses of dried compressed air. This procedure creates an initial packing density of order 0.60 $\pm$ 0.01. The number of flow pulses is generally not the same for each experiment; several pulses are applied initially to ensure a proper erasure of memory effects [109,117]. after which pulses are applied until a packing with a flat surface is obtained. Airflow is turned off during all compaction experiments, which simply consist of observing how Φ evolves while taps are applied.

7.3   Transients & Steady State

Fig. 7.6a shows how the packing typically changes with the number of taps applied to the system, in an experiment where a packing of glass beads is subjected to 250000 taps with $T = 33ms$, and where the amplitude is altered between $\Gamma \sim 2$ and $\Gamma \sim 6$ after each 25000 taps. The packing fraction is only measured every 10 taps. There are several distinct features in this graph: *(i) Initial transient:* Initially the packing fraction evolves slowly towards a steady state value, nonmonotonically in the case depicted in Fig. 7.6b. *(ii) Steady state:* After the initial transient the system is able to reach a steady state packing fraction. The
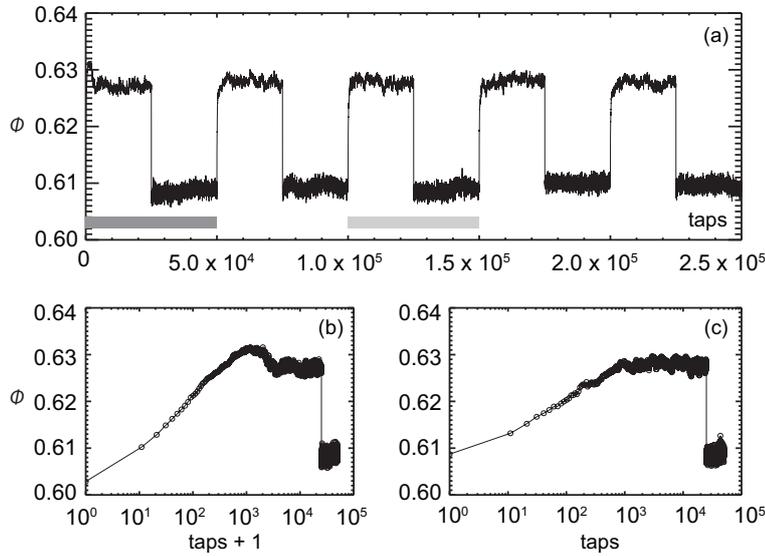
Figure 7.5: (a) Evolution of the packing fraction as function of the number of taps. Here, we fix $T = 33$ ms, and Γ is alternated between $\Gamma = 2$ and $\Gamma = 6$ every 25000 taps. Our data shows that after a short transient, the density can be reversibly changed from one value to another. (b) The initial transient compaction behavior on a logarithmic scale, for the range indicated by the dark grey bar in panel (a). (c) A typical compaction process between two steady states as occurs at $t = 10^5$ s as indicated by the light grey bar in panel (a). Here the horizontal axis labels the number of taps after $t = 10^5$ s.

correspondence between Φ and Γ is also reproducible: changing tap amplitudes repeatedly back and forth shows that for a particular tap amplitude the same steady state packing fraction is always obtained (Fig. 7.6a). *(iii) Amplitude step transient:* When the amplitude of the tap changes, the packing fraction changes too, but not instantaneously. This time dependent process is usually asymmetric in the step direction: an increase of the tap amplitude usually almost immediately dilates the packing to the packing fraction appropriate for the new amplitude. A step down in tap amplitude requires compaction of the packing to reach the steady state packing fraction belonging to the lower tap amplitude. This process is usually slower. As can be seen in Fig. 7.6c, the increase in density from roughly 0.61 to the plateau value ≈ 0.63 takes of the order of 1000 taps, comparable to the initial transient duration.

The initial transient is somewhat different in each experiment. For example,

145

non-monotonicity seen in $\Phi(t)$ in Fig. 7.6 is not always observed. This may either be due to the fact that the preparation of the packing in each experiment is slightly different, or to inherent fluctuations of the density evolution. We identify the transient behavior with the irreversible branch, and the steady state with the reversible branch. The strength of the fluctuations in the early evolution in $\Phi(t)$ hinder a precise comparison of our results to the results from the Chicago and Rennes groups [78, 109, 110]. However, our values for the densities on the reversible branch, $\Phi_{\text{rev}}(\Gamma)$, are far more robust, and in the rest of the paper we focus on $\Phi_{\text{rev}}(\Gamma, T)$ in the steady state.
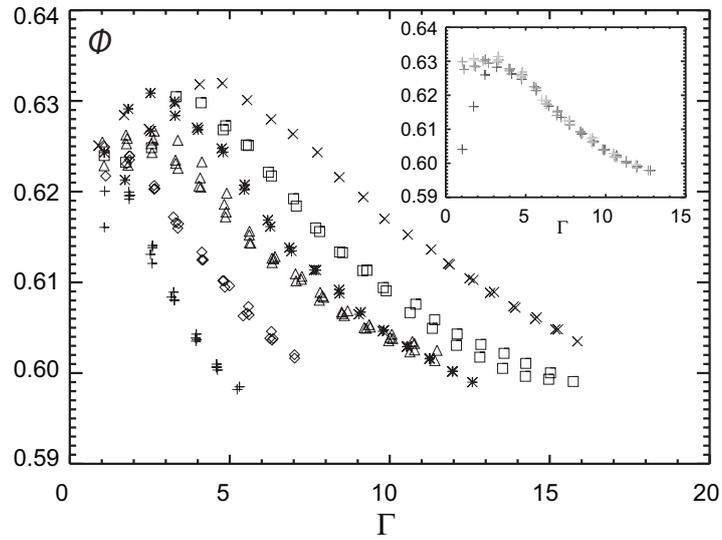
Figure 7.6: Reversible and irreversible branch for the glass bead mixture (See text). The main panel shows the reversible branch $\Phi_{\text{rev}}(\Gamma, T)$ for different tap lengths T ($+$ 50ms, $\diamond$ 33ms, $\triangle$ 16ms, $*$ 14ms, $\square$ 13ms, $\times$ 10ms). Clearly Γ alone is not sufficient to characterize the tapping. The inset shows $\Phi_{\text{rev}}(\Gamma, T)$ for T=14.3ms, and four sweeps in Γ (see text). Greyscale of symbols indicates measurement time; lighter points are later measurements. After an initial transient (black crosses), the densities become history independent.

7.4 Steady State Density as a Function of Γ and T.

As we will show, our experimental protocol allows the determination of $\Phi_{\text{rev}}(\Gamma, T)$. At fixed T, this enables use to reproduce the reversible and irreversible branch
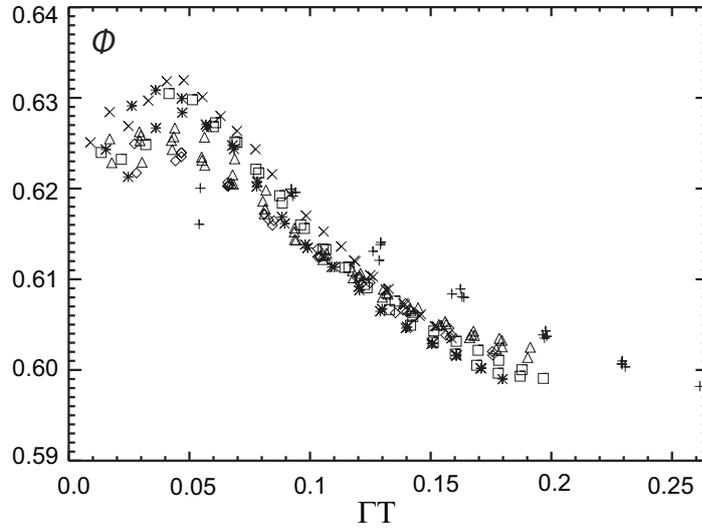
Figure 7.7: Data on Φ for the reversible branches for the glass bead mixture as shown in Fig. 7.6 can be collapsed well when plotted as function of ΓT.

in a $\Phi_{rev}(\Gamma, T)$-plot similar to those found before in the Chicago and Rennes experiments by sweeping Γ up and down several times.

In the inset of Fig. 7.6 we show that the packing density becomes well-defined on the reversible branch. In this experiment, starting from a low density packing, the tap amplitude is sweeped up and down four times, and the number of taps at each different tap amplitude is 4000. Every 20 taps the packing fraction is measured and each data point corresponds to an average over the resulting 200 measurements. The irreversible branch is visible as the initial increase of Φ with Γ. After about 12,000 taps the reversible branch is reached: this branch is clearly shown in the four amplitude sweeps that all follow the same $\Phi_{rev}(\Gamma, T)$ relation, with Φ_{rev} decreasing with Γ.

7.4.1 Effect of the Tap Duration

We will now explore the reversible branch for a range of values of T (Fig. 7.6). The reversible branches obtained in a series of experiments in which Γ is sweeped for a range of values of T are shown in the main panel of Fig. 7.6. The reversible branches for different tap lengths T clearly have the same overall form, but do not coincide -- Γ alone is not the parameter that governs compaction. The

147

spacing of the data and the fact that the functional form of $\Phi_{rev}(\Gamma, T)$ is similar for different T, strongly suggests the data sets can be collapsed onto a master curve. Fig. 7.7 shows that $\Phi)_{rev}(\Gamma, T)$ can be collapsed reasonably well by plotting Φ_{rev} as a function of the product ΓT.
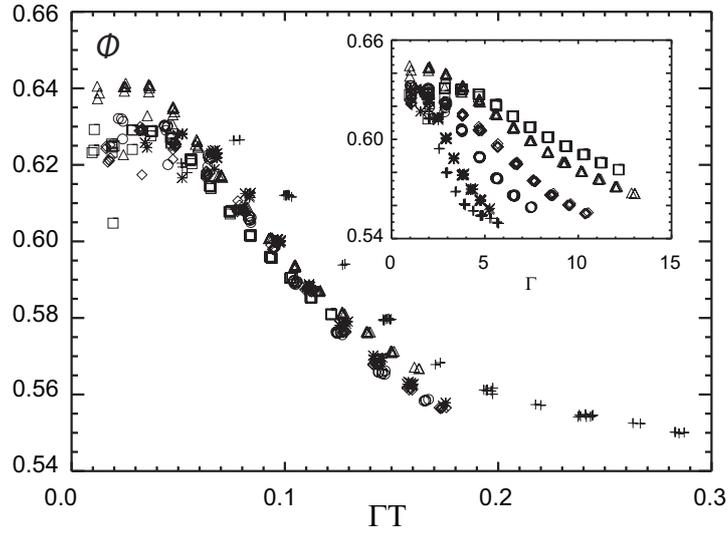
Figure 7.8: $\Phi_{rev}(\Gamma T)$ for the rough bronze powder. Symbols: + 50 ms, * 33 ms, ○ 22 ms, ◇ 17 ms, △ 13 ms , □ 10 ms. Inset: Same data, $\Phi_{rev}(\Gamma, T)$ for the different T.

7.4.2 Bronze Powder

For the bronze powder, we measured the reversible branch $\Phi_{rev}(\Gamma, T)$ for different values of the tap length T; the results are shown in the inset of Fig. 7.8. Note that the range of packing fractions obtained is far larger for the bronze powder, which may be attributed to the roughness of the particles [118]. Similarly to the glass beads, Φ_{rev} collapses onto a master curve when plotted as function of ΓT -- see Fig. 7.8. This shows that the details of the granular material used are entirely insignificant.

7.4.3 Absence of Hysteresis

In Ref. [112] memory effects were observed in the evolution of the packing fraction on the irreversible branch: two different initial conditions where prepared at a certain fixed Φ, by compacting low density systems at different tapping strength.

The time evolution of subsequent compaction differed, despite the fact that the initial packing fraction and tap strength were equal -- hence not only the packing fraction, but also the history is important for the evolution at the irreversible branch.

While such memory effects have not been seen, per definition, on the reversible branch, one may wonder if some more subtle hysteretic effects could arise there. In particular, if the state of the system on the reversible branch is not fully specified by density, it might be that using two control parameters, subtle hysteretic effects not seen when only sweeping the single parameter Γ become apparent.

Since data for Φ_{rev} as a function of Γ and T can be collapsed on a single mastercurve, it follows that Γ and T can be varied at the same time in such a way that Φ_{rev} stays constant. As we will show, we do not observe any appreciable hysteretic effects when switching between different pairs of (Γ, T) adjusted so that $\Phi_{\text{rev}}(\Gamma, T)$ is constant.

We measure the packing fraction of a bronze powder packing while we expose the granular packing to taps with a sequence of different T: 17, 33, 17, 11 ms (Fig. 7.9a) and different Γ. This sequence is repeated three times; each Γ, T-pair was used for 10000 taps, the total number of taps applied in the experiment is 130000. The amplitude Γ (4.84, 2.88, 4.84, 7.32) for each different T, shown in Fig. 7.9b, was finetuned such that the resulting packing fraction stayed the same during the whole experiment; the product ΓT is constant to within 10%. This 10% variation suggests that ΓT is likely an effective approximation of the ultimate order parameter that sets the density on the reversible branch -- see below. The packing fraction evolution during the experiment is shown in Fig. 7.9c. No appreciable transients are observed when switching Γ and T: there is no evidence for any appreciable hysteresis. Our data is further evidence that memory effects, which are a characteristic of the irreversible branch but do not play a role in the reversible branch.

7.5 Interpretation

How can we understand the relevance of ΓT in determining Φ_{rev}? We note that the liftoff velocity $\dot{z}_l$, the time-of-flight τ_f and impact velocity $\dot{z}_i$ are all approximately, although not precisely, proportional to ΓT. Below we briefly discuss these parameters, but note already here that the experimental scatter prevents us from unambiguously determining whether these provide better scaling collapse than the simple ΓT scaling employed above.

(i) Liftoff velocity -- The liftoff velocity $\dot{z}_l$ is determined by calculating the
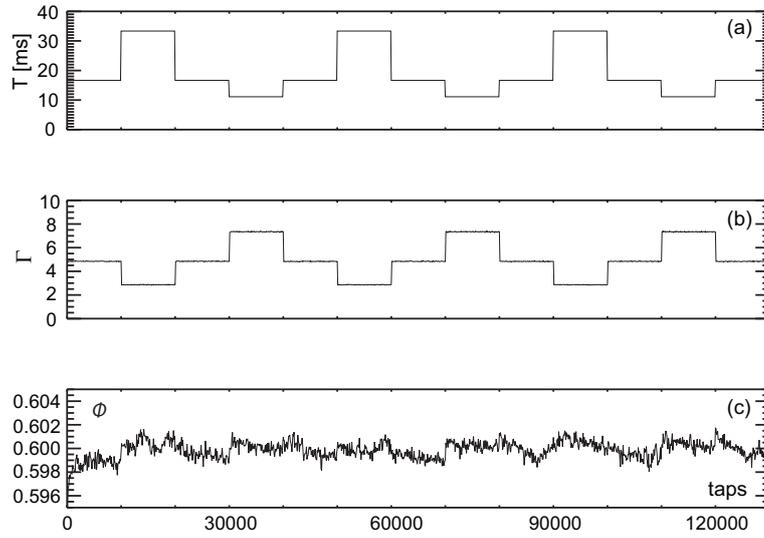
Figure 7.9: T (a) and Γ (b) used in the constant packing fraction sweep. The packing fraction Φ evolution in time is shown in (c). For details, see text.

velocity at the time where the acceleration falls below a threshold $-g\Gamma^*$. In case the packing experiences no friction with the container walls, this threshold equals the gravitational acceleration ($\Gamma^* = 1$), but in general Γ^* is somewhat larger, typically around 1.2. For given Γ^* and waveforms as described above, one finds that in the parameter regime where liftoff occurs ($\Gamma > \Gamma^*$), the liftoff velocity is given by

$$\dot{z}_l = \Gamma\, T \times \left(\frac{g}{2\pi} \left[1 + \sqrt{1 - (\Gamma^*/\Gamma)^2} - \frac{T}{P} \right] \right) . \tag{7.4}$$

For most parameter values, the term within square brackets is close to two -- typically, T/P is of order of a few percent, and for $\Gamma > 5$, the square root term is within a few percent equal to one. The main deviations between the scaling of ΓT and $\dot{z}_l$ occur for small Γ. Our scatter is relatively large in this regime, and in a plot of Φ_{rev} as function of $\dot{z}_l$, the quality of the collapse is very similar to when ΓT is used.

(ii) Time of flight -- In rough approximation, the time of flight τ_f is simply proportional to the liftoff velocity: $\tau_f = 2\dot{z}_l/g$. We have also calculated the time of flight numerically, assuming either the analytic expressions for $z(t)$ and $\ddot{z}(t)$, or using the experimental data available for $z(t)$ and $\ddot{z}(t)$, and taking drag forces into account (These affect the total time of flight of the packing [119]). Despite

the presence of free fit parameters (take off acceleration, drag coefficient), the resulting data collapse when τ_f is used as scaling parameter is only marginal better than for ΓT or $\dot{z}_l$.

(iii) Impact velocity -- The amount of energy dissipated once the packing comes to rest in the container is set by the impact velocity, and this could also be an appropriate choice of rescaling parameter. However, in the range of parameters explored, the impact velocity scales very similar to the time of flight, and the quality of the collapse does not improve.

We hence conclude that while impact velocity or time of flight might give a marginal improvement in the data collapse, the much simpler rescaling parameter ΓT works essentially equally well.

7.6 Conclusions

By precisely controlling the shape of the taps, we find that the compaction of vibrated granular media is not only governed by Γ, the dimensionless peak acceleration; the tap duration plays an equally important role. We observe a collapse of the reversible branch with ΓT, for two different types of granular materials. We do not see any evidence for hysteretic effects when switching between different driving parameters that correspond to the same reversible-branch-density.

The time of flight, the liftoff velocity and the impact velocity all scale similar to ΓT, which makes it impossible to experimentally determine which parameter leads to the best data collapse. In experiments focussing on the transients in granular compaction [114], or on the hydrodynamic phases in vibrofluidize granular materials [120], the order parameter found was always proportional to the injected energy per vibration cycle. We suggest that our scaling supports the view that the energy injected is also the driving mechanism in compaction experiments.

Chapter 8

Appendices

8.1 A: Recovering the Flow Profiles with PIV

We use Particle Image Velocimetry (PIV) [121] techniques to measure flow profiles from sequences of camera images. PIV is a standard technique for flow field visualization, and we will only briefly describe it here. All the PIV techniques and routines are implemented in IDL [122].

Under shear, successively captured images of a certain plane (usually on the surface but also cross sections in the bulk) in a flowing medium can be used to obtain the flow structure of (granular) flows. If the interframe time is sufficiently short such that a finite amount, but not too much strain has occurred in between the two frames (see below for more quantitative statements on this), it is possible to extract the spatial velocity field from these images.

Velocimetry is done by calculating the cross correlation between the intensity profiles $I(x)_i$ on pixel rows[1] x in subsequent frames i and $i + 1$:

$$C_i(\Delta) = \int \frac{I(x)_i I(x + \Delta)_{i+1}}{|I(x)_i|} dx \qquad (8.1)$$

The idea is that if the relative particle position in the pixel row x have not changed from frame i to $i + 1$, then the intensity profiles themselves have not changed from one frame to the next; they are only *shifted*. If only an overall shift has occurred, then Δ for which $C(\Delta)$ is maximal corresponds to this shift between

---

[1]Without loss of generality, we assume here that the image is oriented such that the direction of the flow is parallel to the pixel rows.

Figure 8.1: (a) A typical 8 bit camera image. (b) The image after the histogram equalization contrast enhancement technique discussed below. (c) The coordinates r, θ in the image to be mapped onto the Cartesian coordinates x, y shown in (d). (e) The image from (b), after applying the coordinate transformation. (f) A typical intensity profile of a column of pixels, shown for two consecutive images in black and grey. The overall shift can be computed by finding the maximum in Eq. 8.1. (g) The typical cross correlation function $C(\Delta)$, with a clear maximum at a displacement Δ of about 10 pixels.

the two frames in pixel row x. The velocity of row x is then Δ/t_{frame}, with t_{frame} the interframe time.

By calculating the maximum of $C(\Delta)$, we obtain for each pixel row at coordinate $x = r$ a displacement, and therefore a velocity, measured between two consecutive frames. Averaging this velocity over many consecutive images gives a good measure of the average steady state flow $v(r)$ at that coordinate. Filming series of images at different heights z, we can obtain a three dimensional flow field $v_\theta(r, z)$.

The images we acquire are either small strips in which the particles already move in straight lines, e.g. Fig. 2.9b. Sometimes however, it is more convenient to image the whole cell, such as in Fig. 2.1e, but then the particles trace out a

154

streamline that is approximately a circle. It is easier to use the PIV technique if these streamlines are straight lines that run parallel to the pixel columns or rows in the experimental images. Therefore, we deform those images such that in the images the (r, θ) coordinates of the particle in the box are the x, y coordinates in the image; see Fig. 8.1. After applying this method applied the PIV technique is identical as the one applied to strips.

Optimal PIV settings -- If consecutive images are acquired very slowly, the total displacement in the flow between two frames may be more than the size of the image. The PIV method will cease to work in that limit. If the images are acquired too quickly, the total strain imaged may be far smaller than a pixel, in which case the correlation technique described will also fail. We determined that the optimal maximum amount of strain in images of 800x600 pixels was around 40 pixels. With that amount of strain per image pair, the dynamic range of velocities measurable is about 3 decades.

Improvements in the PIV method -- Apart from getting better statistics from acquiring more images and averaging over longer measurement periods, we use a few other methods that improve the resolution of the PIV method mentioned above substantially. We list them below.

The accuracy in the determination of the location of the peak of $C(\Delta)$ is limited to pixel accuracy. This resolution can be improved by fitting a parabola to the largest three points of $C(\Delta)$, and calculating the maximum of the parabola. Typically 0.1 pixel accuracy per image pair can thus be obtained.

The dynamic range of flow speeds one can typically obtain by using the PIV method mentioned above, is about 2-3 decades. The dynamic range can be increased by another decade by taking different interframe steps. Instead of calculating the correlation coefficient between frame i and $i + 1$, one can also correlate frame i and $i + n$, with $1 < n < N$. This will allow measuring flow speeds in regions of flow that in the acquired images experience less strain than 0.1 pixel per frame, the lower limit resolution with subpixel accuracy. Note that with this technique one has $N - n$ image pairs to average over, with N the total number of images in a single experimental data set. Moreover, only N/n statistically independent frame pairs are available then: the correlation of the error in the strain for image pair $i, i + 1$ and $i + 1, i + 2$ is far smaller than in the image pairs $i, i + n$ and $i + 1, i + n + 1$.

Smoothing of the images was also sometimes used to increase the resolution of the PIV method; it helps to make the gradients in the intensity profiles $I(x)$ less noisy -- see Fig. 8.1e. Smoothing can also be obtained with a slight defocussing of the camera. Note that the effectiveness of smoothing also depends on contrast

and image noise. We used it only when effective, in order to keep CPU time for postprocessing low. We used 5x5 or 3x3 pixel averaging, depending on what was most effective.

Contrast enhancement also greatly improved the PIV method, irrespective of the image quality and pixel noise present. The enhancement technique is available in the standard IDL library, and based on [123]. The effect of contrast enhancement is shown in Fig. 8.1b.

Bibliography

[1] J. Duran. *Sands, Powders and Grains: An Introduction to the Physics of Granular Materials*. 1999.

[2] Y. Forterre and O. Pouliquen. Flows of dense granular media. *Annu. Rev. Fluid Mech.* · 40, 1--24 · 2008.

[3] H. M. Jaeger, S. R. Nagel, and R. P. Behringer. Granular solids, liquids, and gases. *Rev. Mod. Phys.* · 68, 1259--1273 · 1996.

[4] I. Goldhirsch. Rapid granular flows. *Ann. Rev. Fluid Mech.* · 35, 267--293 · 2003.

[5] R.R. Hartley and R.P. Behringer. Logarithmic rate dependence of force networks in sheared granular materials. *Nature* · 421, 928--931 · 2003.

[6] A. Janda, D. Maza, A. Garcimartin, E. Kolb, J. Lanuza, and E. Clément. Unjamming a granular hopper by vibration. *arXiv* · page 0907.0114.

[7] G. A. Caballero-Robledo and E. Clément. Rheology of a sonofluidized granular packing. *arXiv* · page 0907.0317.

[8] R. S. Higginbotham. A cone and plate viscometer. *J. Sci. Instr.* · 27, 139--141 · 1950.

[9] K. Lu, E. E. Brodsky, and H. P. Kavehpour. A thermodynamic unification of jamming. *Nature Phys.* · 4, 404--407 · 2008.

[10] K. Lu, E. E. Brodsky, and H. P. Kavehpour. Shear-weakening of the transitional regime for granular flow. *J. Fluid Mech.* · 587, 347--372 · 2007.

157

[11] P.-E. Peyneau and J.-N. Roux. Frictionless bead packs have macroscopic friction, but no dilatancy. *Phys. Rev. E* · 78, 011307 · 2008.

[12] GDR MiDi. On dense granular flows. *Eur. Phys. J. E* · 14, 341--365 · 2004.

[13] N. W. Mueggenburg. Behavior of granular materials under cyclic shear. *Phys. Rev. E* · 71, 031301 · 2005.

[14] T. Dunstan, J. R. F. Arthur, A. Dalili, O. O. Ogunbekun, and R. K. S. Wong. Limiting mechanisms of slow dilatant plastic shear deformation of granular media. *Nature* · 336, 52--54 · 1988.

[15] A. J. Kabla and T. J. Senden. Dilatancy in slow granular flows. *Phys. Rev. Lett.* · 102, 228301 · 2009.

[16] D. M. Mueth, G. F. Debregeas, G. S. Karczmar, P. J. Eng, S. R. Nagel, and H. M. Jaeger. Signatures of granular microstructure in dense shear flows. *Nature* · 406, 385--389 · 2000.

[17] C. T. Veje, D. W. Howell, and R. P. Behringer. Kinematics of a two-dimensional granular couette experiment at the transition to shearing. *Phys. Rev. E* · 59, 739--745 · 1999.

[18] J.-C. Tsai, G. A. Voth, and J. P. Gollub. Internal granular dynamics, shear-induced crystallization, and compaction steps. *Phys. Rev. Lett.* · 91, 064301 · 2003.

[19] B. Utter and R. P. Behringer. Self-diffusion in dense granular shear flows. *Phys. Rev. E* · 69, 031308 · 2004.

[20] W. Losert, L. Bocquet, T. C. Lubensky, and J. P. Gollub. Particle dynamics in sheared granular matter. *Phys. Rev. Lett.* · 85, 1428--1431 · 2000.

[21] M. van Hecke. Jamming of soft particles: Geometry, mechanics, scaling and isostaticity. *subm.* · 2009.

[22] O. Reynolds. *Phil. Mag.* · 1885.

[23] G. Koval, J.-N. Roux, A. Corfdir, and F. Chevoir. Annular shear of cohesionless granular materials: From the inertial to quasistatic regime. *Phys. Rev. E* · 79, 021306 · 2009.

[24] C.M. Gourlay and A.K. Dahle. Dilatant shear bands in solidifying metals. *Nature* · 445, 70--73 · 2007.

[25] R. M. Nedderman and C. Laohakul. The thickness of the shear zone of flowing granular materials. *Powd. Techn.* · 25, 91 -- 100 · 1980.

[26] C. H. Rycroft, G. S. Grest, J. W. Landry, and M. Z. Bazant. Analysis of granular flow in a pebble-bed nuclear reactor. *Phys. Rev. E* · 74, 021306 · 2006.

[27] J. Choi, A. Kudrolli, R. R. Rosales, and M. Z. Bazant. Diffusion and mixing in gravity-driven dense granular flows. *Phys. Rev. Lett.* · 92, 174301 · 2004.

[28] O. Pouliquen and R. Gutfraind. Stress fluctuations and shear zones in quasistatic granular chute flows. *Phys. Rev. E* · 53, 552--561 · 1996.

[29] K. To, P.-Y. Lai, and H. K. Pak. Jamming of granular flow in a two-dimensional hopper. *Phys. Rev. Lett.* · 86, 71--74 · 2001.

[30] S. Masson and J. Martinez. Effect of particle mechanical properties on silo flow and stresses from distinct element simulations. *Powd. Techn.* · 109, 164 -- 178 · 2000.

[31] D. Fenistein and M. van Hecke. Wide shear zones in granular bulk flow. *Nature* · 425, 356 · 2003.

[32] D. Fenistein, J.-W. van de Meent, and M. van Hecke. Universal and wide shear zones in granular bulk flow. *Phys. Rev. Lett.* · 92, 094301 · 2004.

[33] D. Fenistein, J.-W. van de Meent, and M. van Hecke. Core precession and global modes in granular bulk flow. *Phys. Rev. Lett.* · 96, 118001 · 2006.

[34] X. Cheng, J. B. Lechman, A. Fernandez-Barbero, G. S. Grest, H. M. Jaeger, G. S. Karczmar, M. E. Möbius, and S. R. Nagel. Three-dimensional shear in granular flow. *Phys. Rev. Lett.* · 96, 038001 · 2006.

[35] M. Depken, W. van Saarloos, and M. van Hecke. Continuum approach to wide shear zones in quasistatic granular matter. *Phys. Rev. E* · 73, 031302 · 2006.

[36] M. Depken, J. B. Lechman, M. van Hecke, W. van Saarloos, and G. S. Grest. Stresses in smooth flows of dense granular media. *EPL* · 78, 58001 (5pp) · 2007.

[37] A. Ries, D. E. Wolf, and T. Unger. Shear zones in granular media: Three-dimensional contact dynamics simulation. *Phys. Rev. E* · 76, 051301 · 2007.

[38] E. A. Jagla. Finite width of quasistatic shear bands. *Phys. Rev. E* · 78, 026105 · 2008.

[39] S. Luding. The effect of friction on wide shear bands. *Particulate Sci. and Techn.* · 26, 33--42 · 2008.

[40] K. Sakaie, D. Fenistein, T. J. Carroll, M. van Hecke, and P. Umbanhowar. Mr imaging of reynolds dilatancy in the bulk of smooth granular flows. *EPL* · 84, 49902 · 2008.

[41] T. Unger, J. Török, J. Kertész, and D. E. Wolf. Shear band formation in granular media as a variational problem. *Phys. Rev. Lett.* · 92, 214301 · 2004.

[42] R. Mikkelsen. *Granular Dynamics: Clustering and Shear Flows*. PhD thesis · University of Twente · 2005.

[43] J. Crassous, J.-F. Metayer, P. Richard, and C. Laroche. Experimental study of a creeping granular flow at very low velocity. *J. Stat. Mech.* · page P03009 (15pp) · 2008.

[44] C. S. Campbell. Granular shear flows at the elastic limit. *J. Fluid Mech.* · 465, 261--291 · 2002.

[45] Y. Forterre P. Jop and O. Pouliquen. A constitutive law for dense granular flows. *Nature* · 441, 727--730 · 2006.

[46] J. L. Finney. Random packings and the structure of simple liquids. i. the geometry of random close packing. *Proc. R. Soc. London, Ser. A* · 319, 479--493 · 1970.

[47] M. Pailha, M. Nicolas, and O. Pouliquen. Initiation of underwater granular avalanches: Influence of the initial volume fraction. *Phys. Fluids* · 20, 111701 · 2008.

[48] T. Börzsönyi, R. E. Ecke, and J. N. McElwaine. Patterns in flowing sand: Understanding the physics of granular flow. *Phys. Rev. Lett.* · 103, 178302 · 2009.

[49] P. Schall and M. van Hecke. Shearbands in matter with granularity. *Annu. Rev. Fluid Mech.* · 2010.

[50] T. S. Komatsu, S. Inagaki, N. Nakagawa, and S. Nasuno. Creep motion in a granular pile exhibiting steady surface flow. *Phys. Rev. Lett.* · 86, 1757--1760 · 2001.

[51] J. Török, T. Unger, J. Kertész, and D. E. Wolf. Shear zones in granular materials: Optimization in a self-organized random potential. *Phys. Rev. E* · 75, 011305 · 2007.

[52] W. W. Mullins. Stochastic theory of particle flow under gravity. *J. Appl. Phys.* · 43, 665--678 · 1972.

[53] E. Woldhuis, B. Tighe, and W. van Saarloos. Wide shear zones and the spot model: Implications from the split-bottom geometry. *Eur. Phys. J. E* · 28, 73 -- 78 · 2009.

[54] K. Kamrin and M. Z. Bazant. Stochastic flow rule for granular materials. *Phys. Rev. E* · 75, 041301 · 2007.

[55] P. Jop. Hydrodynamic modeling of granular flows in a modified couette cell. *Phys. Rev. E* · 77, 032301 · 2008.

[56] T.E. Faber. *Fluid Dynamics for Physicist*. 2001.

[57] E. I. Corwin. Granular flow in a rapidly rotated system with fixed walls. *Phys. Rev. E* · 77, 031308 · 2008.

[58] S. Slotterback, M. Toiya, L. Goff, J. F. Douglas, and W. Losert. Correlation between particle motion and voronoi-cell-shape fluctuations during the compaction of granular matter. *Phys. Rev. Lett.* · 101, 258001 · 2008.

[59] W. Losert, K. Ronaszegi, J. Weijs, J. A. Dijksman, and S. Slotterback. Three dimensional particle rearrangements during slow granular shear flow in a split bottom geometry. *P & G 2009: Proc. 6th Intern. Conf. on Micromech. of Gran. Media* · 1145, 347--350 · 2009.

[60] C. Cassar, M. Nicolas, and O. Pouliquen. Submarine granular flows down inclined planes. *Phys. Fluids* · 17, 103301 · 2005.

[61] G. P. Krishnan, S. Beimfohr, and D. T. Leighton. Shear-induced radial segregation in bidisperse suspensions. *J. Fluid Mech.* · 321, 371--393 · 1996.

[62] I. E. Zarraga and Jr. D. T. Leighton. Measurement of an unexpectedly large shear-induced self-diffusivity in a dilute suspension of spheres. *Phys. Fluids* · 14, 2194--2201 · 2002.

[63] Y. Ren. Efficiency shifts of prism coupling into polymer waveguides subject to environmental variations. *Opt. Mater.* · 19, 443--447 · 2002.

[64] D.R. Lide (Ed.). *CRC Handbook of Chemsitry and Physics, 85th Edition*. 2004.

[65] S. Wu, F. Zeng, H. Wang, W. She, and Z. Cai. Thermooptical properties of poly(methyl methacrylate)-based azobenzene composites. *J. Appl. Polymer Sci.* · 89, 2374--2377 · 2003.

[66] H. S. Patel K. Das, B. Jain. Nile blue in triton-x 100/benzenehexane reverse micelles: a fluorescence spectroscopic study. *Spectroch. Acta Part A* · 60, 2059--2064 · 2004.

[67] S. Courrech du Pont, P. Gondret, B. Perrin, and M. Rabaud. Granular avalanches in fluids. *Phys. Rev. Lett.* · 90, 044301 · 2003.

[68] H. Darcy. *Les Fontaines Publique de la Ville de Dijon*. 1856.

[69] J. G. Berryman and S. C. Blair. Kozeny-carman relations and image processing methods for estimating darcy's constant. *J. Appl. Phys.* · 62, 2221--2228 · 1987.

[70] P. Harriott (Eds.) W. McCabe, J. Smith. *Unit Operations of Chemical Engineering*. 2004.

[71] Ph. Renard and G. de Marsily. Calculating equivalent permeability: a review. *Adv. Water Resources* · 20, 253 -- 278 · 1997.

[72] L.D. Landau and E.M. Lifschitz. *Fluid Mechanics*. 1987.

[73] J.-W. van de Meent. private communication.

[74] A. V. Orpe and A. Kudrolli. Velocity correlations in dense granular flows observed with internal imaging. *Phys. Rev. Lett.* · 98, 238001 · 2007.

[75] N. Huang, G. Ovarlez, F. Bertrand, S. Rodts, P. Coussot, and Daniel Bonn. Flow of wet granular materials. *Phys. Rev. Lett.* · 94, 028301 · 2005.

[76] T. Aste, M. Saadatfar, and T. J. Senden. Geometrical structure of disordered sphere packings. *Phys. Rev. E* · 71, 061302 · 2005.

[77] P. Richard, P. Philippe, F. Barbe, S. Bourlès, X. Thibault, and D. Bideau. Analysis by x-ray microtomography of a granular packing undergoing compaction. *Phys. Rev. E* · 68, 020301 · 2003.

[78] P. Philippe and D. Bideau. Compaction dynamics of a granular medium under vertical tapping. *EPL* · 60, 677--683 · 2002.

[79] Vision Research. http://www.visionresearch.com/.

[80] R. Besseling, L. Isa, E. R. Weeks, and W. C.K. Poon. Quantitative imaging of colloidal flows. *Adv. Coll. Interf. Sci.* · 146, 1 -- 17 · 2009.

[81] Particle tracking with IDL. http://www.physics.emory.edu/ weeks/idl/.

[82] S. Slotterback. private communication.

[83] I.M. Krieger and T.J. Dougherty. A mechanism for non-newtonian flow in suspensions of rigid spheres. *J. Rheol.* · 3, 137--152 · 1959.

[84] T. Divoux and J.-C. Géminard. Friction and dilatancy in immersed granular matter. *Physi. Rev. Lett.* · 99, 258301 · 2007.

[85] N. Mitarai and F. Nori. Wet granular materials. *Adv. Phys.* · 55, 1 -- 45 · 2006.

[86] G. K. Batchelors. The effect of brownian motion on the bulk stress in a suspension of spherical particles. *J. Fluid Mech.* · 83, 97--117 · 1977.

[87] G.H Koenderink and A.P. Philipse. Rotational and translational self-diffusion in colloidal sphere suspensions and the applicability of generalized stoke-seinstein relations. *Langmuir* · 16, 5631--5638 · 2000.

[88] J. J. Stickel and R.L. Powell. Fluid mechancis and rheology of dense suspensions. *Annu. Rev. Fluid Mech.* · 37, 129--149 · 2005.

[89] Dow Chemicals. http://www.dow.com/surfactants/.

[90] I. Sánchez, F. Raynaud, J. Lanuza, B. Andreotti, E. Clément, and Igor S. Aranson. Spreading of a granular droplet. *Phys. Rev. E* · 76, 060301 · 2007.

[91] E. Longhi, N. Easwar, and N. Menon. Large force fluctuations in a flowing granular medium. *Phys. Rev. Lett.* · 89, 045501 · 2002.

[92] M. L. Falk and J. S. Langer. Dynamics of viscoplastic deformation in amorphous solids. *Phys. Rev. E* · 57, 7192--7205 · 1998.

[93] P. Sollich, F. Lequeux, P. Hébraud, and M.E. Cates. Rheology of soft glassy materials. *Phys. Rev. Lett.* · 78, 2020--2023 · 1997.

[94] J. Goyon, A. Colin, G. Ovarlez, A. Ajdari, and L. Bocquet. Spatial cooperativity in soft glassy flows. *Nature* · 454, 84--87 · 2008.

[95] A. Janda, D. Maza, A. Garcimartin, E. Kolb, J. Lanuza, and E. Clement. Unjamming a granular hopper by vibration. *EPL* · 87, 24002 · 2009.

[96] G. Caballero, E. Kolb, A. Lindner, J. Lanuza, and E. Clement. Experimental investigation of granular dynamics close to the jamming transition. *J. Phys. Cond. Matt.* · 17, 2503--2516 · 2005.

[97] D. Rubin, N. Goldenson, and G. A. Voth. Failure and strengthening of granular slopes under horizontal vibration. *Phys. Rev. E* · 74, 051307 · 2006.

[98] H. M. Jaeger, Chu-heng Liu, and Sidney R. Nagel. Relaxation at the angle of repose. *Phys. Rev. Lett.* · 62, 40--43 · 1989.

[99] K. Nichol, E. Wandersman, R. Bastien, A. Zanin, and M. van Hecke. Shear-induced agitations create a granular fluid. *subm.* · 2009.

[100] H. K. Pak, E. Van Doorn, and R. P. Behringer. Effects of ambient gases on granular materials under vertical vibration. *Phys. Rev. Lett.* · 74, 4643--4646 · 1995.

[101] New Way. Air bearing application and design guide.

[102] M. Schröter, D. I. Goldman, and H. L. Swinney. Stationary state volume fluctuations in a granular medium. *Phys. Rev. E* · 71, 030301 · 2005.

[103] F. Lechenault, O. Dauchot, G. Biroli, and J. P. Bouchaud. Critical scaling and heterogeneous superdiffusion across the jamming/rigidity transition of a granular glass. *EPL* · 83, 46003 · 2008.

[104] P. Richard, M. Nicodemi, R. Delanney, P. Ribiére, and D. Bideau. Slow relaxation and compaction of granular systems. *Nature Mat.* · 4, 121--128 · 2005.

[105] M. Toiya, J. Stambaugh, and W. Losert. Transient and oscillatory granular shear flow. *Phys. Rev. Lett.* · 93, 088001 · 2004.

[106] H. Hoekstra, J. Vermant, J. Mewis, and G. G. Fuller. Flow-induced anisotropy and reversible aggregation in two-dimensional suspensions. *Langmuir* · 19, 9134--9141 · 2003.

[107] G. Petekidis, D. Vlassopoulos, and P. N. Pusey. Yielding and flow of sheared colloidal glasses. *J. Phys. Cond. Matt.* · 16, 3955--3963 · 2004.

[108] K. Shundyak, M. van Hecke, and W. van Saarloos. Force mobilization and generalized isostaticity in jammed packings of frictional grains. *Phys. Rev. E* · 75, 010301 · 2007.

[109] J. B. Knight, C. G. Fandrich, C. N. Lau, H. M. Jaeger, and S. R. Nagel. Density relaxation in a vibrated granular material. *Phys. Rev. E* · 51, 3957–3963 · 1995.

[110] E. R. Nowak, J. B. Knight, M. L. Povinelli, H. M. Jaeger, and S. R. Nagel. Reversibility and irreversibility in the packing of vibrated granular material. *Powd. Techn.* · 94, 79–83 · 1997.

[111] E. Ben-Naim, J. B. Knight, E. R. Nowak, H. M. Jaeger, and S. R. Nagel. Slow relaxation in granular compaction. *Physica D* · 123, 380–385 · 1998.

[112] C. Josserand, A. V. Tkachenko, D. M. Mueth, and H. M. Jaeger. Memory effects in granular materials. *Phys. Rev. Lett.* · 85, 3632–3635 · 2000.

[113] P. Philippe and D. Bideau. Granular medium under vertical tapping: Change of compaction and convection dynamics around the liftoff threshold. *Phys. Rev. Lett.* · 91, 104302 · 2003.

[114] F. Ludewig, S. Dorbolo, T. Gilet, and T. Vandewalle. Energetic approach for the characterization of taps in granular compaction. *EPL* · 84, 44001 · 2008.

[115] X.Z. An, R.Y. Yang, R.P. Zou, and A.B. Yu. Effect of vibration condition and inter-particle frictions on the packing of uniform spheres. *Powd. Techn.* · 188, 102 – 109 · 2008.

[116] J.C. Macrae, P.C. Finlay, and W.A. Gray. Vibration packing of dry granular solids. *Nature* · 179, 1356–1366 · 1957.

[117] T. Divoux, H. Gayvallet, and J.-C. Geminard. Creep motion of a granular pile induced by thermal cycling. *Phys. Rev. Lett.* · 101, 148303 · 2008.

[118] X. Z. An, R. Y. Yang, K. J. Dong, R. P. Zou, and A. B. Yu. Micromechanical simulation and analysis of one-dimensional vibratory sphere packing. *Phys. Rev. Lett.* · 95, 205502 · 2005.

[119] G. Lumay and N. Vandewalle. Experimental study of the compaction dynamics for two-dimensional anisotropic granular materials. *Phys. Rev. E* · 74, 021301 · 2006.

[120] P. Eshuis, K. van der Weele, D. van der Meer, and D. Lohse. Granular leidenfrost effect: Experiment and theory of floating particle clusters. *Phys. Rev. Lett.* · 95, 258001 · 2005.

[121] G. Katgert. *Flow of Foams*. PhD thesis · Leiden University · 2008.

BIBLIOGRAPHY

[122] Wikipedia. http://en.wikipedia.org/wiki/idl_(programming_language).

[123] S. M. Pizer, E. P. Amburn, J. D. Austin, R. Cromartie, A. Geselowitz, T. Greer, B. Ter Haar Romeny, and J. B. Zimmerman. Adaptive histogram equalization and its variations. *Comput. Vision Graph. Image Process.* · 39, 355-368 · 1987.

Samenvatting

Granulaire materialen zoals zand, rijst en koffie bonen zijn zo alledaags dat we ons nauwelijks realiseren hoe uniek hun eigenschappen eigenlijk zijn. Wie staat nog stil bij het kunnen lopen op een droog, mul, zanderig strand? Wie zal het nog opvallen dat de dikte en stroomsnelheid van de koffieboontjes of -poeder ingesteld kan worden door de zak net iets anders schuin te houden? Wie vindt het verbazend dat een pot met rijst altijd nog net wat extra korrels kan bevatten als je hem een beetje schudt?

Granulaire materialen komt men buiten de keuken ook vaak genoeg tegen: de aluminium legering waaruit onderdelen van uw mobiele telefoon waarschijnlijk bestaan, is gemaakt door een goed gemixte verzameling van - inderdaad -- korrels van verschillende metalen te smelten. Het plotselinge schuifgedrag van aardbevingen en de ontwikkeling van lawines zijn nauw verwant aan de processen die een rol spelen bij het instorten van een zandkasteel. Bovendien zijn granulaire materialen een deel van een veel grotere groep materialen die we *wanordelijke materialen* noemen: wanordelijke verzamelingen van macroscopische deeltjes, zoals mayonaise, tandpasta en scheerschuim.

Wanordelijke materialen, en met hen granulaire materialen, zo kunnen we concluderen, omringen ons in ons dagelijks leven. Maar ondanks hun uitbundige aanwezigheid, begrijpen we hun gedrag nog helemaal niet zo goed. Dit is verwonderlijk, gezien het feit dat er vele andere fysische systemen, bestaand uit veel, met elkaar wisselwerkende deeltjes, bestaan die we wel goed begrijpen. Neem bijvoorbeeld de lucht die we inademen: die bestaat uit een onbevattelijke hoeveelheid kleine rondvliegende moleculen, terwijl haar eigenschappen al reeds ruim een eeuw goed worden begrepen. Substanties als water en kristallijne, vaste stoffen, andere voorbeelden van grote verzamelingen ronddansende moleculen, zijn ook al goed begrepen. Waarom zijn dan wanordelijke materialen zo lastig te begrijpen?

De moeilijkheid voor het vinden van die beschrijving ligt hem in het gegeven dat korrels anders met elkaar wisselwerken dan atomen en moleculen in gassen, vloeistoffen en vaste stoffen. Zand korrels bijvoorbeeld, *wrijven* en botsen *inelastisch* als ze met elkaar in contact komen, wat betekent dat die interacties energie laten wegvloeien. Daarom is het zo dat als ze niet extern wordt aangedreven, een verzameling van korrels tot rust komt in een toestand waarin alle relevante interne dynamica tot stilstand komt. In tegenstelling tot gassen, vloeistoffen en vaste stoffen, waarin moleculen en atomen altijd blijven rondvliegen, botsen, tollen en vibreren, zitten de korrels in een hoop granulair materiaal vast -- ze zijn als het ware bevroren. Daarom is de gebruikelijke gereedschapskist met methodes waarmee een natuurkundige veel-deeltjes systemen beschrijft niet van toepassing. Het vinden van methodes en technieken die bijvoorbeeld het stromingsgedrag of de elasticiteit van deze 'bevroren' materialen beschrijft is een buitengewoon diepzinnig probleem gebleken in de moderne natuurkunde.

We bestuderen wanordelijke materialen experimenteel, door de stroming van ronde glaskogeltjes te onderzoeken. Hiertoe gebruiken we een speciaal stuk gereedschap: de *split-bottom* geometrie. In essentie is het een bak met op de bodem ervan een kleine draaiende schijf; vandaar de naam 'split-bottom'. Korrels kan men in de bak deponeren, en door de schijf te draaien zullen de korrels meegetrokken worden, en zal er dus stroming ontstaan. De split-bottom geometrie is een zeer nuttig instrument gebleken om granulaire stromingen te bestuderen, omdat het deze materialen op een speciale manier 'breekt' - er ontstaan brede stromingsgebieden in het materiaal, waarin zeer vele deeltjes meedoen. Het is voor een dergelijke stroming dat men graag een model zou willen hebben dat bijvoorbeeld het stromingsveld voorspelt. Op dit moment is er nog geen model dat dit afdoende doet.

We bestuderen deze speciale stroming in de split-bottom geometrie op verschillende manieren: in hoofdstuk 2 kijken we naar de reologie van dergelijke stromingen. Simpel gezegd is reologie de relatie tussen de toegepaste krachten op de stroming, en het resulterende stromingsgedrag. In langzame stromingen domineert de wrijving tussen de deeltjes de reologie. Als de korrelstroming sneller wordt aangedreven, zullen de korrels meer en sneller met elkaar gaan botsen. Bij een zekere aandrijfsnelheid zullen krachten die een rol spelen bij deze botsingen groter worden dan de wrijvingskrachten, welke snelheidson-afhankelijk zijn. We bestuderen deze overgang, die zichtbaar is in de reologie als een toename van de kracht die nodig is om de stroming aan te drijven. We testen ook nog een voorspelling voor de reologie van granulaire stromingen in de split-bottom geometrie, die voortkomt uit een theorie die was opgezet om een aspect van het stromingsgedrag te beschrijven.

In hoofdstuk 3 en 5 bestuderen we granulaire stromingen, die geheel plaatsvinden in een vloeistof in de split-bottom geometrie. Deze stromingen staan beter bekend als suspensiestromingen. De vloeistof die nu tussen de deeltjes aanwezig is, verandert de reologie van deze stroming op een niet-triviale wijze, maar we laten zien dat deze reologie beschreven kan worden door een bestaande, fenomenologische theorie voor snelle granulaire stromingen op gepaste wijze aan te modificeren.

Granulaire materialen onderdompelen is niet slechts een manier om de interacties tussen de deeltjes te veranderen. We kunnen de brekingsindex van de vloeistof gelijk maken aan die van de korrels, met als gevolg dat de suspensie transparant wordt. Terwijl gewone korrelige materialen niet doorzichtig zijn, waardoor dus alleen aan het oppervlak de eigenschappen kunnen worden waargenomen, kunnen we in een transparante suspensie in drie dimensies bijvoorbeeld stromingseigenschappen bestuderen. We ontdekken dat het bovengenoemde model voor de reologie ook voor de *stromingsstructuur* de juiste voorspellingen geeft, voornamelijk in de limiet van snelle stromingen.

Drie dimensionale stromingen van een vloeistof meten is niet gemakkelijk, laat staan van een geconcentreerde suspensie. We besteedden hieraan een significante hoeveelheid werk, en dit is het onderwerp van hoofdstuk 4. We laten zien dat het instrument dat we hebben ontwikkeld suspensiestroming in groot detail kan meten, en met ongeëvenaarde snelheid.

In hoofdstuk 6 zullen we een granulair materiaal laten smelten door het zachtjes te vibreren. We bestuderen wederom de reologie van dit 'gesmolten' materiaal in de split-bottom geometrie, en we vinden dat deze reologie compleet verandert door maar de kleinste hoeveelheid vibraties; zelfs langzame, wrijvingsgedomineerde stromingen worden snelheidsafhankelijk. Bovendien maken de vibratiegeïnduceerde agitaties een nieuw type stroming mogelijk, die nog niet eerder was waargenomen.

In hoofdstuk 7 doen we een experiment, vergelijkbaar met het schudden van een pot met rijst om er meer aan toe te kunnen voegen: we bestuderen hoe een goed gecontroleerde schudbeweging de dichtheid van een stapeling korrels in een glazen buis beïnvloedt. We vinden dat er een limiet is waarin het aantal schudbewegingen niet meer uitmaakt voor de uiteindelijke dichtheid. De uiteindelijk behaalde dichtheid hangt ook af van de totaal toegevoegde energie per schudbeweging, en niet alleen van zijn amplitude, zoals voorheen altijd werd aangenomen.

Summary

Granular materials such as sand, rice and coffee beans are so common that we hardly ever realize how unique their properties are. Who marvels at the fact one can walk on a dry sandy beach? Who will notice the surprising fact that we can tune the rapidity and thickness of the stream of coffee beans into the grinder, simply by holding the bag differently? Who will find it surprising that a jar of rice can always contain a little amount of extra rice, if you shake the jar a little?

Granular materials are also encountered outside of the kitchen: the aluminum alloy of which the cover of your mobile phone is probably made, is made by melting a well mixed collection of -- indeed -- small grains of different metals. The stick-slip motion of earthquakes, and the development of snow avalanches are closely related to the processes that occur in a collapsing sand castle.

Moreover, granular materials are part of an even larger class of materials called *disordered materials*: disordered collections of macroscopic particles, such as mayonnaise, toothpaste and shaving foam.

Disordered materials, and with them granular materials, it can be concluded, fill our everyday life. But despite the omnipresence of these materials, we still do not understand their behavior very well. This is surprising, considering that there are many other types of physical systems with many interacting particles that we do understand. Consider the air we breathe: it is made out of sheer unimaginable number of tiny molecules flying around, yet its properties are well understood, for more than a century already. Substances like water and crystalline solids, other examples of large collections of molecules jiggling around, are also well understood. Then why is the behavior of a small collection of simple sand grains or foam bubbles so hard to model?

The difficulty in describing disordered materials is due to the fact that granular materials interact differently than molecules and atoms that make up gases, liquids and solids. Sand grains for example *rub* or collide *inelastically*

when they come in contact, which means these interactions dissipate energy. Therefore, when not externally driven, a collection of grains comes to rest in a state in which all relevant internal dynamics have ceased. Unlike molecules in ordinary gases, liquids and solids, which always fly, bounce, tumble and vibrate around, the grains in a heap of granular material are stuck -- they are, as one might say, frozen. Therefore, all the ordinary tools physicists have available to describe systems with a large number of particles break down. Finding tools that describe for example the flow behavior, or simply the elasticity of these 'frozen' or *jammed* materials, has proven to be a profound challenge in modern physics.

We study disordered materials experimentally, by studying the flow of spherical glass beads. For this we use a special tool: the *split-bottom* geometry. Essentially, it is a container with a small rotating disk at the bottom; hence the name 'split-bottom'. Grains are poured into the container, and the disk is rotated. The disk drags along the particles, and flow is thus induced. The split-bottom setup is a useful tool to study granular flows, since the rotating disk 'breaks' the granular material in a very special way -- very broad flowing zones are created, in which many glass beads participate. It is for such flows that one would like to have a model that for example predicts the flow structure. At the moment such models do not exist.

We study these special granular flows in the split-bottom geometry in several ways: In chapter 2, we look at the *rheology* of such flows: simply put, the rheology is the relation between the forces applied to the flow and the resulting speed of the flow. In slow flows, grains are mostly rubbing against each other, so friction forces dominate the rheology of the flow. When driven faster, the grains in the split-bottom start to collide at higher speeds and more frequently. At some driving rate, the forces related to these collisions will become more important than the frictional forces between the particles, which are independent of the driving rate. We study this transition, which is observed as an increase in the force needed to drive the flow. We verify rheological predictions of a model, initially devised to predict only flow structure properties of split-bottom flows.

In chapter 3 and 5, we study submersed granular flows, also know as suspension flows, in the split-bottom geometry. The fluid now present between the particles changes the rheology of these granular flows flows in an nontrivial way, but we show we can readily capture this by extending an existing, phenomenological theory for fast granular flows.

Submersing grains is not just a way to change the interactions between the particles. We can tune the index of refraction of the interstitial liquid such that is matches the index of the beads -- our suspension is then transparent. Whereas ordinary, dry, granular materials are opaque, and only their surface can

be observed, in transparent suspensions we can study the flow properties in three dimensions. We discover that the extended rheology model mentioned above also gives the right predictions for the flow *structure*, mainly in the fast driving limit.

Measuring three dimensional flow structure of a fluid, let alone a dense suspension, is not easy. We devoted a substantial amount of work to develop an experimental setup capable of doing so. This is the subject of chapter 4; we show there that with the instrument we developed, we can now scan suspension flows in great detail, at unparalleled imaging rates.

In chapter 6, we 'unfreeze' granular materials by means of very weak vibrations. Again, we study the flow of glass beads in the split-bottom geometry, and find that its rheology is completely modified by the weak vibrations: weak vibrations make even slow, friction-dominated flows rate dependent. Moreover, we discover that weak agitations make new types of granular flow possible that had not been observed before.

In chapter 7 we do an experiment, analogous to tapping a jar of rice to add more grains to it: we study how well controlled taps influence the packing density of two different types of granular materials in a glass tube. We find that there is a limit in which the number of taps does not influence the density anymore -- one cannot keep adding rice grains indefinitely. The control parameter that sets this *steady state* densities, we find to be related to the energy input that the tap delivers, and not simply its amplitude, as was previously assumed.

Publication List

[1a]   J.A. Dijksman and M. van Hecke,
        Granular Flows in Split Bottom Geometries
[1b]   J.A. Dijksman, G. Wortel and M. van Hecke,
        Rheology of weakly vibrated granular materials
[1c]   W. Losert, K. Ronaszegi, J. Weijs, J.A. Dijksman and S. Slotterback,
        Three Dimensional Particle Rearrangements During Slow Granular Shear Flow
        In A Split Bottom Geometry
        Powders and Grains 2009: Proceedings of the 6th International Conference
        on Micromechanics of Granular Media, (2009)
[2]   J.A. Dijksman and M. van Hecke,
        The role of the tap duration for the steady state density of vibrated
        granular media.,
        Accepted for EPL, (2009); arXiv:0903.5499.

Other publications, unrelated to this thesis:

[1]   S. Yu. Krylov, J.A. Dijksman, W. van Loo and J.W.M. Frenken,
      Stuck in slipperiness: do we get what we see in atomic scale friction?
      Phys. Rev. Lett 94, 102123 (2006).

[2]   F. J. Verbaan, S. M. Bal, D. J. van den Berg, J. A. Dijksman, M. van Hecke,
      H. Verpoorten, A. van den Berg, R. Luttge, J. A. Bouwstra.
      Improved piercing of microneedle arrays in dermatomed human skin
      by an impact insertion method.,
      J. Contr. Release 128, 80-88 (2008).

[3]   P. H. Hovenkamp, R. W. J. M. van der Ham, G. A. van Uffelen, M. van Hecke,
      J. A. Dijksman and W. Star.
      Spore movement driven by the spore wall in an eusporangiate fern
      Grana 45, 122 (2009).

Curriculum Vitae

The Hague was the place of my birth on the fourth of November, 1981. I went to high school in Rijswijk (Zuid-Holland) and Goes (Zeeland), receiving my VWO diploma from 'Het Goese Lyceum' in June 2000. I studied experimental physics at Leiden University, where I received my degree in Experimental Physics in November 2005, for the thesis 'Intruder dynamics in weakly vibrated granular media', work carried out under supervision of Prof. Dr. Martin van Hecke.

I continued my education at Leiden University by doing a Ph.D. in experimental granular physics in Martin's group. During this time, I attended courses in Utrecht, Enschede, Leiden and Les Houches, France. I attended conferences in Veldhoven, Eindhoven; Tampa, Pittsburgh, New Orleans, Colby College (United States); Naples (Italy), Rennes (France); Lund (Sweden) and London (England), and presented my work in the form of a poster or a talk in the Netherlands, England, Germany, the United States and Italy. I also participated in an exchange program with the University of Maryland, where I worked for three months in the group of dr. Wolfgang Losert. I was also a teaching assistant for the undergraduate LabVIEW practicum for three years, and enjoyed participating in physics outreach programs such as the *Junior Science Lab*, and during the annual *Wetenschapsdag*.

Acknowledgements

The content of this thesis has benefited greatly from discussions I had with several people, whom I would like to thank here. Of course the daily discussions with colleagues here in Leiden have been very fruitful; in this context I would like to mention, in random order, Gijs Katgert, Matthias Möbius, Elie Wandersman, Wim van Saarloos, Wouter Ellenbroek, Brian Tighe, Zorana Zeravcic, Alexander Morozov, Eric Sultan, Paul Becherer, Erik Woldhuis and Jan-Willem van de Meent.

All the experimental work would certainly not have been possible without the excellent technical support received from Fred Kranenburg, Jeroen Mesman, Ton Tampung and Raymond Koehler.

I would like to thank Wolfgang Losert for his hospitality during my visit to the University of Maryland, and Steven Slotterback, Chris Berardi and Don Martin for all the help and technical support received there.

I would also like to thank Kinga Lorincz, Peter Schall, Rut Besseling, Tamas Unger, Matthias Schröter, Bob Behringer, Olivier Pouliquen, Deniz Ertas, Olivier Dauchot, Heinrich Jaeger and Jerry Gollub for sharing their valuable comments, remarks and insights with me.

Naturally, writing a thesis is not a solitary enterprise. I will thank all the people who contributed in a non-scientific manner to this thesis elsewhere.